

**MINISTÉRIO DA DEFESA
EXÉRCITO BRASILEIRO
DEPARTAMENTO DE CIÊNCIA E TECNOLOGIA
INSTITUTO MILITAR DE ENGENHARIA
PROGRAMA DE PÓS-GRADUAÇÃO EM ENGENHARIA ELÉTRICA**

VITOR TEIXEIRA KLINGELFUS

**SIDELobe SUPPRESSION AND MUTUAL COUPLING RESISTANT
TECHNIQUE FOR NARROWBAND BEAMFORMERS**

**RIO DE JANEIRO
2025**

VITOR TEIXEIRA KLINGELFUS

SIDELobe SUPPRESSION AND MUTUAL COUPLING RESISTANT
TECHNIQUE FOR NARROWBAND BEAMFORMERS

Dissertação apresentada ao Programa de Pós-graduação
em Engenharia Elétrica do Instituto Militar de Engenharia,

Orientador(es): José Antonio Apolinário Júnior, D.Sc.
Cláudio Augusto Barreto Saunders Filho,
Ph.D.

Rio de Janeiro

2025

©2025

INSTITUTO MILITAR DE ENGENHARIA

Praça General Tibúrcio, 80 – Praia Vermelha

Rio de Janeiro – RJ CEP: 22290-270

Este exemplar é de propriedade do Instituto Militar de Engenharia, que poderá incluí-lo em base de dados, armazenar em computador, microfilmар ou adotar qualquer forma de arquivamento.

É permitida a menção, reprodução parcial ou integral e a transmissão entre bibliotecas deste trabalho, sem modificação de seu texto, em qualquer meio que esteja ou venha a ser fixado, para pesquisa acadêmica, comentários e citações, desde que sem finalidade comercial e que seja feita a referência bibliográfica completa.

Os conceitos expressos neste trabalho são de responsabilidade do(s) autor(es) e do(s) orientador(es).

Klingelfus, Vitor Teixeira.

SIDELobe SUPPRESSION AND MUTUAL COUPLING RESISTANT
TECHNIQUE FOR NARROWBAND BEAMFORMERS / Vitor Teixeira Klingel-
fus . – Rio de Janeiro, 2025.

82 f.

Orientador(es): José Antonio Apolinário Júnior e Cláudio Augusto Barreto
Saunders Filho.

Dissertação (mestrado) – Instituto Militar de Engenharia, Engenharia Elétrica,
2025.

i. Antonio Apolinário Júnior, José (orient.) ii. Augusto Barreto Saunders
Filho, Cláudio (orient.) iii. Título

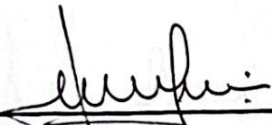
VITOR TEIXEIRA KLINGELFUS

**SIDELobe SUPPRESSION AND MUTUAL COUPLING
RESISTANT TECHNIQUE FOR NARROWBAND
BEAMFORMERS**

Dissertação apresentada ao Programa de Pós-graduação em Engenharia Elétrica do Instituto Militar de Engenharia,

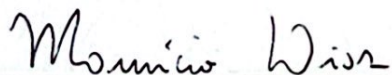
Orientador(es): José Antonio Apolinário Júnior e Cláudio Augusto Barreto Saunders Filho.

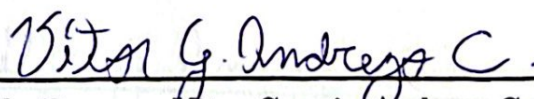
Aprovada em 14 de Fevereiro de 2025, pela seguinte banca examinadora:


Orientador - José Antonio Apolinário Júnior, D.Sc., do IME.


Co-orientador - Cláudio Augusto Barreto Saunders Filho, Ph.D. do IME.


Membro da Banca - Aline de Oliveira Pinto Silva, D.Sc., do IPqM.


Membro da Banca - Maurício Henrique Costa Dias, D.Sc., do CEFET-RJ.


Membro da Banca - Vitor Gouvêa Andrezo Carneiro, D.Sc., do IME.

Rio de Janeiro

2025

*This work is dedicated to my family,
and, to all those who dream and pursue their dreams.*

ACKNOWLEDGEMENTS

I thank, first of all, God, in His mighty love for overlooking and providing me with this amazing life opportunity.

The most special thanks goes to my family, my wife Helga and my son Henri, for their infinite love and patience with the extremely long hours of dedication and focus.

To my advisors Colonel José Antonio Apolinário Júnior and Lieutenant Colonel Cláudio Augusto Barreto Saunders Filho for their orientation, patience, technical teachings, and friendship.

To my colleague in the Brazilian Navy Lieutenant Paulo César Ribeiro Marciano, for the friendship and initial help with the master course.

To the Brazilian Navy, a noble institution that inspires me to do my best every day.

To IME for the solid academic graduation.

*“Aprendi desde menino que,
tudo na vida a gente consegue,
com luta e dignidade:
correr com as pernas,
aguentar com o coração,
vencer com a cabeça...
(Vanderlei Cordeiro de Lima)*

RESUMO

Em um teatro de operações de guerra eletrônica, o ambiente eletromagnético pode ser denso e a interferência eletromagnética geralmente está presente nas medidas ativas de guerra eletrônica radar e comunicações. Nesse cenário, as técnicas de formação de feixe adaptativas (ABF) em arranjos de antenas são essenciais para melhorar a relação sinal-interferência mais ruído (SINR) e para melhorar a recepção de sinais fracos e com baixa relação sinal-ruído. No entanto, as técnicas de formação de feixe adaptativas geralmente não são orientadas para controlar os níveis de lóbulo lateral (SLL). O controle de SLL pode melhorar o SINR e reduzir a suscetibilidade à interferência de radiofrequência indesejada de um número considerável de novos interferidores adicionados ao cenário eletromagnético. Nosso primeiro tema de pesquisa é o desenvolvimento de uma técnica de supressão de lóbulos laterais para formadores de feixe adaptativos com base em uma abordagem de posicionamento de nulos, propondo novos algoritmos que empregam algoritmos adaptativos com restrições lineares. Os resultados das simulações demonstram a eficácia da abordagem proposta no controle de SLL e seu efeito na supressão de interferência para diferentes números de antenas. Nosso segundo tema de pesquisa diz respeito aos efeitos de acoplamento mútuo em arranjos de antenas. O acoplamento mútuo entre elementos do arranjo causa distorção no diagrama de radiação e degradação do desempenho, levando à supressão indesejada do sinal e a uma redução significativa no SINR. ABF normalmente atenua essas distorções por meio da calibração prévia do arranjo e do conhecimento prévio do *array manifold vector* (AMV) in-situ ou realista, o que é conhecido como uma tarefa demorada e que requer ser realizada com antecedência. No entanto, em cenários práticos onde o AMV realista é desconhecido, algoritmos de formação de feixe adaptativos tendem a convergir para soluções distorcidas, que se desviam substancialmente do desempenho de um sistema calibrado, resultando em perda significativa de SINR. Nosso trabalho aborda esse desafio propondo um algoritmo que atenua os efeitos de distorção do sinal sem exigir conhecimento prévio do AMV realista. O algoritmo não requer assumir uma estrutura específica para a matriz de acoplamento mútuo, como Toeplitz por exemplo. Ele combina um projeto de formador de feixe robusto com nossa técnica de supressão de lóbulos laterais. Como estudos de caso, as matrizes de acoplamento mútuo de três arranjos de antenas linear uniformes são estimadas usando simulações eletromagnéticas 3D de onda completa. Os resultados demonstram a eficácia da abordagem proposta em melhorar significativamente o desempenho da formação de feixes e o SINR em cenários onde o AMV realista é desconhecido.

Palavras-chave: supressão de lóbulos laterais; acoplamento mútuo; formação de feixe adaptativa; restrições lineares; interferência de radiofrequência; supressão de interferidores; formação de feixe robusta; arranjo linear uniforme; direção de chegada.

ABSTRACT

In an electronic warfare theater of operations, the electromagnetic environment can be dense, with electromagnetic interference commonly affecting radar and communications electronic support measures. In this scenario, antenna array adaptive beamforming (ABF) techniques are essential to improve the signal-to-interference plus noise ratio (SINR) and to enhance the reception of weak signals and low signal-to-noise ratio. However, adaptive beamforming is usually not oriented to control the sidelobe levels (SLL). SLL control could improve the SINR and may reduce the susceptibility to undesired radio frequency interference of a considerable number of new jammers added to the electromagnetic scenario. Our first research theme is the development of a sidelobe suppression technique for adaptive beamformers based on a null placement approach, proposing new algorithms that employ constrained adaptive algorithms. Simulation results demonstrate the effectiveness of the proposed approach in controlling SLL and its effect on interference suppression for different numbers of antennas. Our second research theme concerns mutual coupling effects in antenna arrays. Mutual coupling between antenna array elements causes radiation pattern distortion and performance degradation, leading to undesired signal suppression and a significant reduction in the SINR. ABF typically mitigates these distortions through prior array calibration and previous knowledge of the in-situ or realistic array manifold vector (AMV), which is known as a time-consuming task that requires being performed in advance. However, in practical scenarios where the realistic AMV is unknown, adaptive beamforming algorithms tend to converge to distorted solutions, which deviate substantially from the performance of a calibrated system, resulting in significant SINR loss. Our work addresses this challenge by proposing an algorithm that mitigates signal distortion effects without requiring prior knowledge of the realistic AMV. The algorithm does not assume a specific structure for the mutual coupling matrix (MCM), such as Toeplitz. It combines a robust design with our sidelobe suppression technique. As case studies, the MCMs of three uniform linear antenna arrays are estimated using full-wave 3D electromagnetic simulations. The results demonstrate the effectiveness of the proposed approach in significantly enhancing beamforming performance and SINR in scenarios where the realistic array manifold is unknown.

Keywords: sidelobe suppression; mutual coupling; adaptive beamforming; linear constraints; radio-frequency interference; jammer suppression; robust beamforming; uniform linear array (ULA); direction of arrival (DOA).

LIST OF FIGURES

Figure 1 – Block diagram of the beamformer adopted in this thesis with an M antenna array followed by M receivers and an array signal processor. The output of an array processor is $y(k) = \mathbf{w}^H \mathbf{x}(k)$	21
Figure 2 – Coordinate system and an example of an $M = 8$ dipole antenna array. The figure illustrates, at the M -th antenna, the typical dipole radiation pattern (without mutual coupling).	22
Figure 3 – Example of beampatterns for an $M = 20$ ULA beamformer steered at 90° for different distances between sensors: (left) $d = 0.3\lambda$, (center) $d = 0.5\lambda$, the most usual choice, and (right) $d = 1.3\lambda$ where we observe undesirable grating lobes. Similar to the example in [6].	25
Figure 4 – A transmission line terminated in a load impedance Z_L [37].	27
Figure 5 – Flowchart of the proposed sidelobe suppression approach from [8].	31
Figure 6 – Methodology used concerning Sidelobe Suppression.	32
Figure 7 – In the NP-SLS Algorithm loops, when used with an adaptive beamformer, our approach entails iteratively updating coefficients from the previous vector (\mathbf{B} as in before) $\mathbf{w}_B \in \mathcal{H}_0$ to the closest vector (\mathbf{A} as in after) such that $\mathbf{w}_A \in \mathcal{H}_0 \cap \mathcal{H}_1$, the intersection of hyperspaces \mathcal{H}_0 and \mathcal{H}_1	34
Figure 8 – Strategy of the CLMS Algorithm with NP-SLS.	37
Figure 9 – Confidence interval analysis of the NP-SLS MPDR algorithm. The SOI is fixed at 45° and the jammer ranges from 0 to 30° and from 60 to 180° , representing the cases of jammer DOAs not too close to the SOI DOA. It displays the minimum final SLL level versus the number of array elements M	40
Figure 10 – Confidence interval analysis of the NP-SLS MPDR algorithm. The SOI is fixed at 45° and the jammer ranges from 0 to 30° and from 60 to 180° , representing the cases of jammer DOAs not too close to SOI DOA. It displays the number of required loops.	40
Figure 11 – Comparing the performance of the NP-SLS CLMS Algorithms, Versions 1 and 2, for a block with $K = 23,000$ snapshots. Note that the beampatterns at the end of the first block, after sidelobe suppression, are identical in both versions.	41
Figure 12 – Comparing SINR and the squared norm deviation of the coefficient vectors of the NP-SLS CLMS Algorithms, Versions 1 and 2, for a block with $K = 23,000$ snapshots.	42

Figure 13 – SINR performance of the NP-SLS CLMS Algorithms, Versions 1 and 2, for 2,000,000 snapshots.	43
Figure 14 – Comparing SINR and the squared norm deviation of the coefficient vectors of the NP-SLS CLMS Algorithms, Versions 1 and 2, for a block with $K = 250$ snapshots.	44
Figure 15 – Methodology used concerning Mutual Coupling evaluation and mitigation.	48
Figure 16 – Example of model configuration for calculation of $\mathbf{a}_{\text{iso},1}(\phi)$ in a dipole array with $M = 4$ antenna elements.	53
Figure 17 – Example of model configuration for calculation of $\mathbf{a}_{\text{oc},4}(\phi)$ in a dipole array with $M = 4$ antenna elements.	54
Figure 18 – Dipole array design model as used in the HFSS [®] software.	56
Figure 19 – Bowtie array design model as used in the HFSS [®] software.	56
Figure 20 – Microstrip array design model as used in the HFSS [®] software.	56
Figure 21 – Dipole array gain radiation pattern result (in dB) in HFSS [®] software.	57
Figure 22 – Bowtie array gain radiation pattern result (in dB) in HFSS [®] software.	58
Figure 23 – Microstrip array gain radiation pattern result (in dB) in HFSS [®] software.	58
Figure 24 – MPDR beampattern for a generic isotropic array in a non-mutual coupling environment (top left). Beampatterns for the studied dipole, bowtie, and microstrip arrays with mutual coupling.	60
Figure 25 – MPDR beampattern for a generic isotropic array in a non-mutual coupling environment (top left). Beampatterns for the studied dipole, bowtie, and microstrip arrays with mutual coupling. A simplified MC model was used instead of the complete one.	62
Figure 26 – Graphical interpretation of the BF Algorithm and its robust version. The blue vector is the regular robust BF case and the red vector stands for the restrained robust BF result.	64
Figure 27 – Strategy of the RNP-SLS ABF Algorithm.	65
Figure 28 – BP of the dipole array using the RNP-SLS CLMS algorithms, versions 1 and 2, for two blocks of $K = 50,000$ snapshots each.	68
Figure 29 – BP of the bowtie array using the RNP-SLS CLMS algorithms, versions 1 and 2, for two blocks of $K = 50,000$ snapshots each.	69
Figure 30 – BP of the microstrip array using the RNP-SLS CLMS algorithms, versions 1 and 2, for two blocks of $K = 50,000$ snapshots each.	70
Figure 31 – Comparing the SINR (linear) performance of the RNP-SLS CLMS algorithms, V1 and V2, for two blocks of $K = 50,000$ snapshots each.	71

LIST OF TABLES

Table 1 – Data format of the computed simulated complex voltages under isolated condition	52
Table 2 – Data format of the computed simulated complex voltages under open-circuit condition	53
Table 3 – Dipole Array Scattering Matrix (in dB)	56
Table 4 – Bowtie Array Scattering Matrix (in dB)	56
Table 5 – Microstrip Array Scattering Matrix (in dB)	57
Table 6 – Final SINR (linear) achieved by the NP-SLS and robust techniques and their combination	72
Table 7 – Final front-to-sidelobe ratio (dB), or SLL, achieved by the NP-SLS and robust techniques and their combination	72

LIST OF ABBREVIATIONS AND ACRONYMS

ABF	Adaptive Beamforming
ADC	Analog to Digital Converter
AI	Artificial Intelligence
AMV	Array Manifold Vector
BF	Beamforming or Beamformer
BP	Beampattern
CBB	Complex Baseband
CCG	Constrained Conjugate Gradient
CESM	Communications Electronic Support Measures
CLMS	Constrained LMS
CNLMS	Constrained Normalized LMS
CRLS	Constrained RLS
CST	Computer Simulation Technology
DF	Direction Finding
DOA	Direction of Arrival
D&S	Delay and Sum
DMI	Direct Matrix Inversion
EEP	Embedded Element Pattern
EM	Electromagnetic
EMI	Electromagnetic Interference
EMS	Electromagnetic Spectrum
EW	Electronic Warfare
GSC	Generalized Sidelobe Canceler
HFSS	High-Frequency Structure Simulation Software

IF	Intermediate Frequency
IME	Instituto Militar de Engenharia
ISWCS	International Symposium on Wireless Communication Systems
LCAF	Linear Constrained Adaptive Filter
LMS	Least Mean Squares
MC	Mutual Coupling
MCE	Mutual Coupling Environment
MOE	Minimum Output Energy
MPDR	Minimum Variance Distortionless Response
NEC	Numerical Electromagnetic Codes
NB	Narrowband
NP-SLS	Null Placement Sidelobe Suppression
RESM	Radar Electronic Support Measures
RLS	Recursive Least Squares
RF	Radiofrequency
SDR	Software Defined Radio
SINR	Signal-to-Interference plus Noise Ratio
SL	Sidelobe
SLL	Sidelobe Level
SNR	Signal to Noise Ratio
SOI	Signal of Interest
SV	Steering Vector
ULA	Uniform Linear Array

CONTENTS

1	INTRODUCTION	16
1.1	CONTEXT AND MOTIVATION	16
1.2	OBJECTIVES	18
1.3	MASTER THESIS STRUCTURE	18
2	THEORETICAL FOUNDATION	20
2.1	A CBB SNAPSHOT VECTOR MODEL	20
2.1.1	BEAMFORMER ARCHITECTURE	20
2.1.2	SINGLE RECEIVER SIGNAL MODEL	20
2.1.3	ANTENNA ARRAY SIGNAL MODEL	21
2.2	FUNDAMENTALS ON CONSTRAINED ADAPTIVE FILTERING	23
2.2.1	NARROWBAND OPTIMUM AND DETERMINISTIC BEAMFORMING	23
2.2.2	BEAMPATTERN AND GRATING LOBES	25
2.2.3	SINR	26
2.2.4	ADAPTIVE BEAMFORMING	26
2.3	REFLECTION AND TRANSMISSION COEFFICIENTS AND THE SCATTERING MATRIX	27
3	SIDELOBE SUPPRESSION	30
3.1	LITERATURE REVIEW CONCERNING SIDELOBE SUPPRESSION	30
3.2	METHODOLOGY CONCERNING SIDELOBE SUPPRESSION	31
3.3	THE NP-SLS MPDR ALGORITHM	33
3.4	USING THE NP-SLS WITH AN ADAPTIVE FILTER	33
3.4.1	THE NP-SLS ALGORITHM FOR AN ABF	36
3.5	SIDELOBE SUPPRESSION RESULTS	39
4	A MUTUAL COUPLING RESISTANT APPROACH	46
4.1	LITERATURE REVIEW CONCERNING MUTUAL COUPLING COMPENSATION	46
4.2	METHODOLOGY FOR MUTUAL COUPLING EVALUATION AND MITIGATION	46
4.3	MODELING THE MUTUAL COUPLING	48
4.3.1	A REALISTIC MUTUAL COUPLING MODEL FOR A ULA	48
4.3.2	THE MUTUAL COUPLING MATRIX	50
4.3.3	CALCULATION OF ARRAY RESPONSE USING 3D ELECTROMAGNETIC SIMULATION	51

4.3.4	SIGNAL MODEL WITH MUTUAL COUPLING	54
4.4	ANTENNA ARRAY SCENARIOS	55
4.5	OPTIMUM BEAMFORMING WITH MUTUAL COUPLING	59
4.5.1	MPDR BEAMFORMING WITH MUTUAL COUPLING	59
4.5.2	MPDR BEAMFORMING WITH MUTUAL COUPLING AND WITHOUT KNOWL- EDGE OF THE REALISTIC ARRAY MANIFOLD	59
4.5.3	MUTUAL COUPLING EFFECTS AND THE CONVERGENCE OF AN ABF IN CASE OF MUTUAL COUPLING	59
4.6	SIMPLIFIED VERSION OF MUTUAL COUPLING MODEL	61
4.7	THE PROPOSED SCHEME	62
4.7.1	ROBUST ADAPTIVE BEAMFORMER	62
4.7.2	THE ROBUST NP-SLS MPDR ALGORITHM	64
4.7.3	THE ROBUST NP-SLS ALGORITHM FOR ABF	65
4.8	ANALYSIS OF COMPUTATIONAL COMPLEXITY	67
4.9	SIMULATION RESULTS	68
5	CONCLUSION	73
5.1	FINAL CONSIDERATIONS	73
5.2	FUTURE WORK	74
5.3	PUBLISHED AND SUBMITTED PAPERS	75
	BIBLIOGRAPHY	76

1 INTRODUCTION

The naval warfare theater of operations is a complex tactical environment, where having information as a tactical advantage is crucial. In this context, knowing the electromagnetic emission environment and being able to identify and respond to a possible threat might be the difference between the success and failure of a mission.

Electronic Warfare (EW) concerns performing actions in the electromagnetic spectrum such as interception, analysis, classification, gathering of information, manipulation, and protection of friendly usage, to provide an element of strategy and combat power for a given nation [1]. EW is crucial in modern defense and security operations, as it ensures control over the electromagnetic spectrum (EMS), a critical domain in today's technology-driven world. EW enhances a nation's intelligence-gathering and operational capabilities by enabling the detection, interception, and disruption of enemy communications and radar systems. Therefore, it supports offensive and defensive strategies, making it a key component of modern warfare.

Aboard a naval warship, specialized equipment is responsible for receiving and processing electromagnetic spectrum data for electronic warfare purposes. For example, Radar Electronic Support Measures (RESM) handle radar signals, while Communications Electronic Support Measures (CESM) manage communication signals [2]. These systems usually employ antenna arrays to determine the Direction of Arrival (DOA) of incoming signals and to record the emission to classify them based on a known database [3]. Therefore, the field of Array Signal Processing [4] plays a key role in Electronic Warfare.

1.1 Context and Motivation

In an electronic warfare theater of operations, the electromagnetic environment can be dense and Electromagnetic Interference (EMI) is usually present. EMI can be severe when a jamming signal is mixed with the Signal of Interest (SOI) or when the receivers are very sensitive. In this scenario, improving the signal-to-interference plus noise ratio (SINR) is of main importance to enhance the reception of weak signals and low signal-to-noise ratio (SNR) [5].

Array signal processing techniques can be employed in an array of sensors to enhance the SOI from a specific direction, as well as to reduce interference of undesired directions. This spatial filtering process is known in the literature as beamforming (BF) [4, 6], and can be divided into deterministic, optimum, and adaptive. Deterministic BF does not depend on the incoming data statistics, but on the known directions to be enhanced or reduced [6]. Optimum beamforming relies on knowing the statistical information of

the incoming signals, as in the minimum power distortionless response (MPDR) BF [4]. Adaptive beamforming (ABF) relies on estimating the statistics, or at least its adequate substitute, and adapting to the incoming data [4].

However, adaptive beamforming is usually not oriented to control the sidelobe levels (SLL). SLL control could improve the SINR. Also, minimizing the sidelobes may reduce susceptibility to undesired radio frequency interference [7], which may be significant when receiving a considerable number of new jammers added to the electromagnetic scenario [8]. Optimization techniques have been used to control the sidelobe level and optimize the radiation pattern as in [8–12]. The work in [8] presents a scheme, in the form of a flowchart, to, in parallel to an ABF technique, achieve a specified sidelobe level, improving SINR and directivity. However, it leaves room for developing a specific algorithm or technique to perform such a task. Therefore, the first topic for this master degree research is the development of a technique to enhance sidelobe suppression to adaptive beamformers. Our approach is based on employing linear constraints to an adaptive beamforming algorithm in order to perform null placement sidelobe suppression.

Additionally, having beamforming improvement as our main goal, another research topic of interest is to incorporate mutual coupling into ABF techniques. ABF algorithms employ array manifold vectors (AMV) to process the signal and to calculate the output weight vector, consequently constructing the beampattern [6]. Frequently, the AMV is built on the assumption that the array elements radiate like isotropic sources, isotropic AMV, disregarding possible mutual coupling (MC) between antenna array elements [13]. Therefore, the isotropic AMV would consider only the time delay between the array elements, while the realistic AMV, also commonly known in the literature as in-situ, analytic, or electromagnetic AMV, would also incorporate the effects of a possible non-isotropic radiation pattern of the elements along with the mutual coupling effects between them [14, 15]. For that reason, the realistic array manifold vector, based on Maxwell equations and electromagnetic theory, is the most accurate mathematical model for the array's response to the incoming signals [4, 15].

Mutual coupling in antenna arrays is commonly defined as the effect of electromagnetic (EM) interactions between antennas that can alter the radiation pattern, the array manifold vector, and, consequently, impact the overall performance of the array [16–18]. It may impair communication and the ability to reject radio frequency interference [7]. Due to signal suppression, imprecise beamforming is achieved, resulting ultimately in a decreased signal-to-interference plus noise ratio. Over the past decades, vast work has been performed on the research of mutual coupling in antenna arrays, leading to several techniques for modeling, estimating, and mitigating its effects [19–27]. However, most of the current mutual coupling compensation techniques present in the literature involve array calibration, as in [16, 18, 28, 29], which requires, ultimately, an estimation of the realistic array manifold vector through Maxwell equations, instead of using the standard

isotropic AMV. It usually requires either previous array measurements or 3D full-wave simulations, known both to be extensive and time-consuming works or, at least, a task to be performed in advance [13, 30, 31]. Nevertheless, considering a practical scenario of an uncalibrated array, the realistic array manifold vector is unknown, and the ABF would converge to a distorted beamforming solution, with a significant loss in performance, signal quality, and signal-to-interference plus noise ratio.

The second topic of this master degree research is a study of the signal-impairing effects caused by the mutual coupling between antenna array elements to their beampatterns inside optimum and ABF techniques; and a proposal of a solution to those effects when the realistic array manifold vector is unknown, i.e., the array is not previously compensated or calibrated.

1.2 Objectives

Based on the two previously mentioned research topics of sidelobe suppression improvement and mutual coupling evaluation and mitigation for uncalibrated arrays, with optimum and adaptive beamforming techniques, these are the main objectives to be achieved with this master thesis:

- (i) To explore and extend null placement sidelobe suppression (NP-SLS) to adaptive beamformers, proposing new approaches that employ constrained adaptive algorithms.
- (ii) To estimate the mutual coupling on different antenna-type uniform linear arrays (ULA), and to calculate the respective realistic array manifold vectors.
- (iii) To incorporate the realistic array manifold vectors into optimum and adaptive beamformers and to observe and evaluate the effects on the beampatterns and SINRs for the different arrays.
- (iv) To propose a solution to mitigate the signal-impairing effects for the scenario when the array is not previously calibrated, i.e., without previous knowledge of the realistic array manifold vector.

1.3 Master Thesis Structure

This thesis is structured in chapters, each of them carrying out a specific function in describing the work performed.

In Chapter 2, the fundamental concepts employed for both sidelobe suppression and mutual coupling fields are explained. It covers the complex baseband (CBB) snapshot vector model, beamformer architecture and generic signal model used, constrained adaptive

filtering basics, and some transmission line theory fundamentals.

In Chapter 3, we cover the contributions in the field of sidelobe suppression. It covers the literature revision, the methodology employed, and the development of the proposed algorithms along with a discussion of the results.

Chapter 4 is dedicated to the contributions in the mutual coupling evaluation and compensation field. It is composed of the literature revision and methodology employed, along with the modeling, 3D electromagnetic simulation, BF calculation, and evaluation of the mutual coupling effects to the beamformers. Finally, it covers the proposed scheme and analysis of the results of a mutual coupling resistance technique for uncalibrated beamformers.

Chapter 5 closes this thesis with the final considerations and future work proposed.

2 THEORETICAL FOUNDATION

In this Chapter, some basic concepts have been introduced with the purpose of paving the way for the specific sidelobe suppression study in Chapter 3 and mutual coupling resistance study in Chapter 4.

2.1 A CBB snapshot vector model

Array signal processing is usually carried out with either analytic or CBB signals [6]. Analytic signals have their real and imaginary components related to each other by the Hilbert transform and contain energy only on the positive side of their spectrum. In this work, the signals are also assumed narrowband such that $\Delta f/f_o \ll 1$, where Δf is the signal bandwidth and f_o is the operating frequency. CBB signals are obtained through a phase-quadrature modulation scheme on a digital receiver. Therefore, assuming far-field propagation conditions, signals from different array elements can be easily delayed and time-aligned when the distance between the elements is known, and the angles of arrival are based on a fixed reference.

2.1.1 Beamformer Architecture

Figure 1 displays the beamformer architecture considered in this work: an M antenna array followed by M synchronized receivers that feed the resulting snapshot vector $\mathbf{x}(k)$ to an array signal processor.

In the RF front-end, after low-noise amplification, the narrowband signal is downconverted to an intermediate frequency (IF), as in a basic heterodyne receiver architecture [32]. The IF analog signal is sampled at f_s in the analog-to-digital converter (ADC), demodulated in-phase and quadrature, and decimated by a factor R so that the final sampling frequency of $x(k)$ is $2\Delta f$, twice the modulator signal bandwidth.

2.1.2 Single Receiver Signal Model

The narrowband SOI, which is received by an antenna array, is time-delayed between consecutive elements of the array and embedded in additive noise; represented by

$$x(t) = s(t - \Delta t) \cos(\Omega_o(t - \Delta t)) + n(t), \quad (2.1)$$

where Δt is the time-delay due to the direction of arrival (DOA), $\Omega_o = 2\pi f_o$, and $n(t)$ is white Gaussian noise. After passing through the receiver architecture depicted in Figure 1,

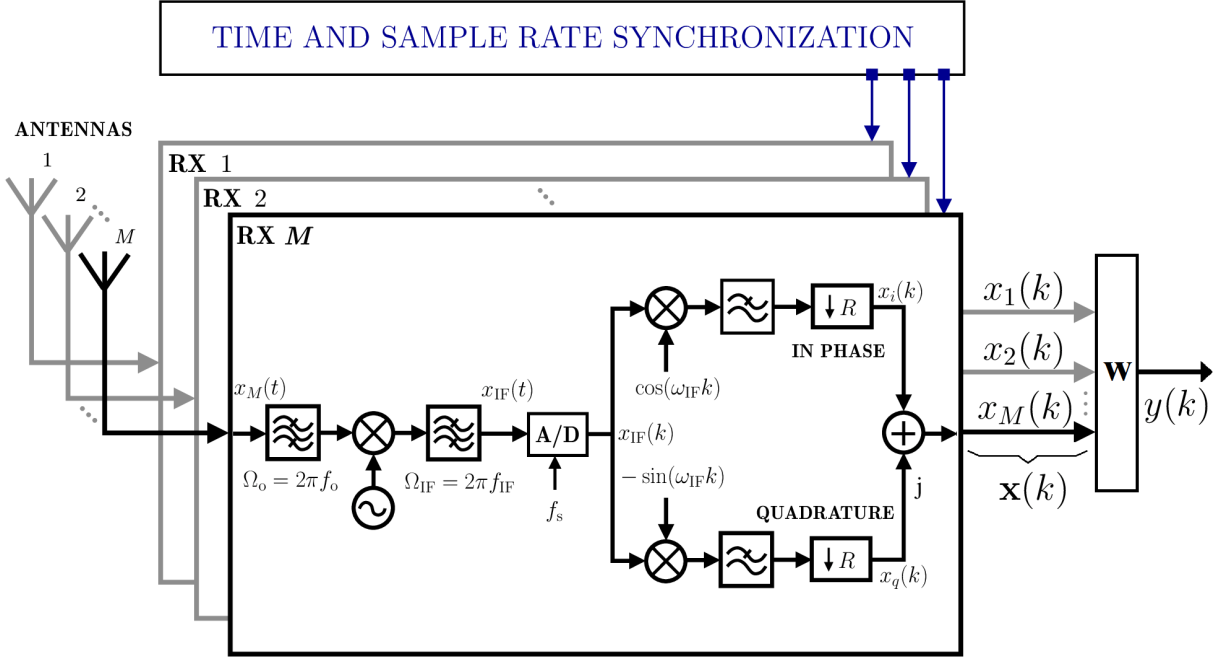


Figure 1 – Block diagram of the beamformer adopted in this thesis with an M antenna array followed by M receivers and an array signal processor. The output of an array processor is $y(k) = \mathbf{w}^H \mathbf{x}(k)$.

the discrete-time CBB signal follows the model:

$$x(k) = x_I(k) + jx_Q(k) = s(k)e^{-j\Omega_o\Delta t} + n(k), \quad (2.2)$$

where $x_I(k)$ and $x_Q(k)$ are the in-phase and quadrature components that compose the CBB signal. It is worthwhile mentioning that the time-delay information, Δt , is present in the phase of the CBB signal.

2.1.3 Antenna Array Signal Model

Each signal received by a different array element has a different time delay. Assuming no mutual coupling between antenna elements, isotropic antennas, and a single emitter, the signal model for an array of M elements is represented as:

$$\mathbf{x}(k) = \begin{bmatrix} x_1(k) \\ \vdots \\ x_m(k) \\ \vdots \\ x_M(k) \end{bmatrix} = s(k) \underbrace{\begin{bmatrix} e^{-j\Omega_o\Delta t_1} \\ \vdots \\ e^{-j\Omega_o\Delta t_m} \\ \vdots \\ e^{-j\Omega_o\Delta t_M} \end{bmatrix}}_{\mathbf{a}(\phi)} + \underbrace{\begin{bmatrix} n_1(k) \\ \vdots \\ n_m(k) \\ \vdots \\ n_M(k) \end{bmatrix}}_{\mathbf{n}(k)}, \quad (2.3)$$

which is known in the literature as the snapshot vector [4], its m_{th} element being $x_m(k) = s(k)e^{-j\Omega_o\Delta t_m} + n_m(k)$, and, assuming a ULA, $\mathbf{a}(\phi)$ corresponds to the isotropic array manifold vector containing the phase delays for each antenna.

Figure 2 depicts the coordinate system, with azimuth angle ϕ and elevation angle θ , and an example of a ULA with $M = 8$ antennas linearly disposed along the x axis, centered at the origin, and separated by distance d , which is usually close to $\frac{\lambda}{2}$.

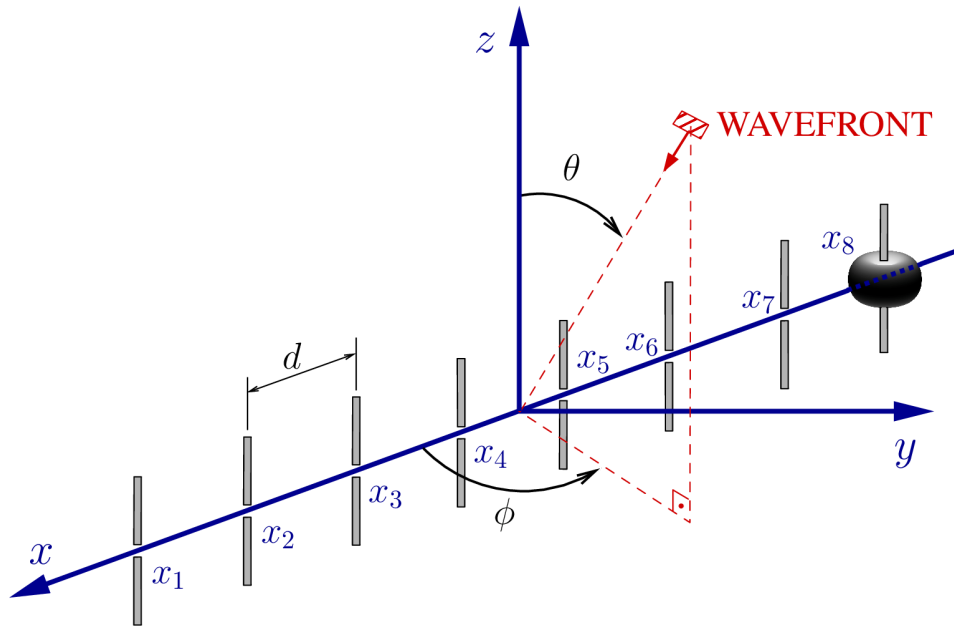


Figure 2 – Coordinate system and an example of an $M = 8$ dipole antenna array. The figure illustrates, at the M -th antenna, the typical dipole radiation pattern (without mutual coupling).

The isotropic AMV for a ULA is defined as:

$$\mathbf{a}(\phi) = \left[1 \quad e^{-j\frac{2\pi d \cos \phi}{\lambda}} \quad \dots \quad e^{-j\frac{2\pi(M-1)d \cos \phi}{\lambda}} \right]^T, \quad (2.4)$$

and it depends only on the direction of arrival ϕ and on the array's geometry. The m_{th} time delay is $\Delta t_m = (m - 1)d \cos(\phi)/c$, where c is the speed of light, d is the physical separation between antenna elements, $\lambda = c/f_o$ is the wavelength, and f_o is the operating frequency.

Consider now the case of D different sources, $D \leq M$, 1 SOI (ϕ_1) and $D - 1$

jammers (ϕ_2 to ϕ_D), so that the signal model adopted herein is:

$$\begin{aligned}
\mathbf{x}(k) &= s_1(k)\mathbf{a}(\phi_1) + \cdots + s_D(k)\mathbf{a}(\phi_D) + \mathbf{n}(k) \\
&= \underbrace{\begin{bmatrix} \mathbf{a}(\phi_1) & \cdots & \mathbf{a}(\phi_D) \end{bmatrix}}_{\mathbf{A} \text{ (steering matrix)}} \underbrace{\begin{bmatrix} s_1(k) \\ \vdots \\ s_D(k) \end{bmatrix}}_{\mathbf{s}(k)} + \mathbf{n}(k) \\
&= \mathbf{A}\mathbf{s}(k) + \mathbf{n}(k),
\end{aligned} \tag{2.5}$$

where \mathbf{A} is the steering or array manifold matrix containing the D array manifold vectors for each DOA.

2.2 Fundamentals on constrained adaptive filtering

Array signal processing techniques in an array of sensors can be employed in applications such as to determine the signals' direction of arrival, and to enhance the SOI from a specific direction and reduce interference of undesired directions. The latter is a spatial filtering known as beamforming [4, 6], and can be divided into deterministic, optimum, and adaptive. Deterministic BF depends only on the known directions to be enhanced or reduced [6]. Optimum beamforming relies on knowing the statistical information of the incoming signals, as in the MPDR BF [4]. On the other hand, adaptive beamformers change according to the incoming data estimating its statistics [4]. After the signals are received and demodulated, they pass through a signal processor as in Figure 1, being \mathbf{w} the coefficient vector and $y(k) = \mathbf{w}^H \mathbf{x}(k)$ its output at a given instant k . This signal processor performs the spatial filtering, or beamforming, that enhances the signal on the known signal of interest's direction, ϕ_1 , and places nulls on the directions of other impinging signals [6]. This is carried out in practice by adjusting the weight vector \mathbf{w} which is subject to the distortionless criteria, $\mathbf{w}^H \mathbf{a}(\phi_1) = 1$ [33].

2.2.1 Narrowband Optimum and Deterministic Beamforming

A first possible approach to a beamforming technique is to minimize the variance or the energy of the output signal, $\mathbb{E}[|y(k)|^2]$ subject to $\mathbf{w}^H \mathbf{a}(\phi) = 1$. Since $|y(k)|^2 = y(k)y^*(k) = \mathbf{w}^H \mathbf{x}(k) \mathbf{x}^H(k) \mathbf{w}$, $\mathbb{E}[|y(k)|^2] = \mathbb{E}[\mathbf{w}^H \mathbf{x}(k) \mathbf{x}^H(k) \mathbf{w}] = \mathbf{w}^H \mathbf{R}_x \mathbf{w}$ is the objective function which, when minimized, corresponds to the minimum output energy (MOE). Applying Lagrange multipliers and performing algebraic manipulations, the outcome yields the following derivatives $\nabla \mathcal{L}(\mathbf{w}, \lambda)_{\mathbf{w}^*} = \mathbf{R}_x \mathbf{w} + \lambda^* \mathbf{a}(\phi)$ and $\nabla \mathcal{L}(\mathbf{w}, \lambda)_{\lambda^*} = \mathbf{w}^H \mathbf{a}(\phi) - 1$, which, when solved and equated to zero, result in the optimal solution

$$\mathbf{w}_{\text{MPDR}} = \frac{\mathbf{R}_x^{-1} \mathbf{a}(\phi)}{\mathbf{a}^H(\phi) \mathbf{R}_x^{-1} \mathbf{a}(\phi)}. \tag{2.6}$$

This is the minimum power distortionless response (MPDR) beamformer solution [6]. From the signal model in Equation (2.5), we know that $\mathbf{R}_x = \mathbf{A}\mathbf{R}_s\mathbf{A}^H + \mathbf{R}_n$, where $\mathbf{R}_s = \mathbb{E}[\mathbf{s}(k)\mathbf{s}^H(k)]$ and $\mathbf{R}_n = \mathbb{E}[\mathbf{n}(k)\mathbf{n}^H(k)]$ are the signal and noise covariance matrices [6]. Another approach for beamforming is when minimizing $\mathbf{w}^H\mathbf{w}$ subject to the distortionless criteria $\mathbf{w}^H\mathbf{a}(\phi) = 1$, i.e. when assuming $\mathbf{R}_x = \mathbf{I}$. After employing Lagrangian multipliers, it yields the solution known as Delay and Sum (D&S) beamformer [6]:

$$\mathbf{w}_{\text{D\&S}} = \frac{1}{M}\mathbf{a}(\phi). \quad (2.7)$$

The D&S solution is considered deterministic since it does not rely on the knowledge of the statistics of the impinging signals. In practical terms, the MPDR solution enhances the SOI and creates nulls in the directions of other unwanted signals whose information is contained in \mathbf{R}_x . The D&S solution attains the distortionless response without taking into account the statistical information from the input signals; therefore there is no information to place nulls in unwanted directions.

By minimizing the output power objective function $\mathbf{w}^H\mathbf{R}_x\mathbf{w}$ subject to $\mathbf{C}^H\mathbf{w} = \mathbf{f}$, the problem is presented in a more generalized form, where $\mathbf{C} = [\mathbf{a}(\phi_1) \cdots \mathbf{a}(\phi_D)]$ is a matrix of up to D linear constraints columns having steering vectors (SV). Vector \mathbf{f} , with the length as the number of columns of \mathbf{C} , or the number of linear constraints, can be customized depending on the application. For example, $\mathbf{f} = [1 \ 0 \ \cdots \ 0]^T$ means enhancing the signals from ϕ_1 (SOI) and placing nulls on the remaining directions (jammers). By employing Lagrangian multipliers it yields the following constraining problem:

$$\mathcal{L}(\mathbf{w}, \boldsymbol{\lambda}) = \mathbf{w}^H\mathbf{R}_x\mathbf{w} + \text{Real}[\boldsymbol{\lambda}^H(\mathbf{C}^H\mathbf{w} - \mathbf{f})]. \quad (2.8)$$

It results in the following derivatives $\nabla\mathcal{L}(\mathbf{w}, \boldsymbol{\lambda})_{\mathbf{w}^*} = \mathbf{R}_x\mathbf{w} + \frac{1}{2}\mathbf{C}\boldsymbol{\lambda}$ and $\nabla\mathcal{L}(\mathbf{w}, \boldsymbol{\lambda})_{\boldsymbol{\lambda}^*} = \frac{1}{2}\mathbf{C}^H\boldsymbol{\lambda} - \frac{1}{2}\mathbf{f}$ that, when solving, simplifying and equating to zero, results in:

$$\mathbf{w} = \mathbf{R}_x^{-1}\mathbf{C}(\mathbf{C}^H\mathbf{R}_x^{-1}\mathbf{C})^{-1}\mathbf{f}, \quad (2.9)$$

which is equivalent to the linearly constrained adaptive filter (LCAF) for the beamforming application [6].

Equations (2.6), and (2.7) are particular cases of (2.9) when $\mathbf{C} = \mathbf{a}(\phi_1)$, and $\mathbf{f} = 1$, with $\mathbf{R}_x = \mathbf{I}$ for the D&S. Therefore, the linear constrained filter theory makes it possible to enforce fixed linear restrictions, whether for enhancing the SOI, $\mathbf{w}^H\mathbf{a}(\phi_1) = 1$, or for placing nulls, $\mathbf{w}^H\mathbf{a}(\phi_i) = 0$, $i \neq 1$ and $i \leq M$. i stands for the index for the signal directions with nulls placed on them.

2.2.2 Beampattern and Grating Lobes

The beampattern associated with an array coefficient vector \mathbf{w} may be then defined as the energy of this gain as a function of a DOA (angle ϕ for a ULA), [6], which in the linear normalized form is given as:

$$BP(\phi) = \frac{\mathbf{w}^H \mathbf{a}(\phi)}{\max_{\phi} (\mathbf{w}^H \mathbf{a}(\phi))}, \quad (2.10)$$

or expressed in dB:

$$BP_{\text{dB}}(\phi) = \frac{10 \log \left(|\mathbf{w}^H \mathbf{a}(\phi)|^2 \right)}{\max_{\phi} (10 \log \left(|\mathbf{w}^H \mathbf{a}(\phi)|^2 \right))}. \quad (2.11)$$

An example is presented in Figure 3, where we observe the beampattern of a 20 sensor D&S beamformer steered to 90° (uniformly weighted linear array, i.e., $\mathbf{w} = \frac{1}{M} \mathbf{1}_{M \times 1}$) with different sensor spacing: 0.3λ , 0.5λ , and 1.3λ . As detailed in Figure 3, one can notice that 0.5λ is the most effective since it presents the main lobe having a smaller beamwidth without the risk of grating lobes [4] entering the visible region ($0^\circ \leq \phi \leq 180^\circ$) as occurs for $d = 1.3\lambda$.

A grating lobe is a lobe with the same height as the main lobe, usually outside the visible region, but which could move into this region when we increase the distance between sensors [6]. If the array spacing is greater than $d = \lambda$ the peak of the grating lobe will occur inside the visible region, meaning an ambiguity of the peak response. However, in order to steer the array in the entire visible region $0^\circ \leq \phi \leq 180^\circ$ it is required that $d \leq \frac{\lambda}{2}$ [4]. The uniform linear array with $d = \lambda/2$ is referred to as a standard linear array [4]. The grating lobe problem, or spatial undersampling, is similar to that of aliasing in time series analysis which occurs when we undersample the time domain waveform.

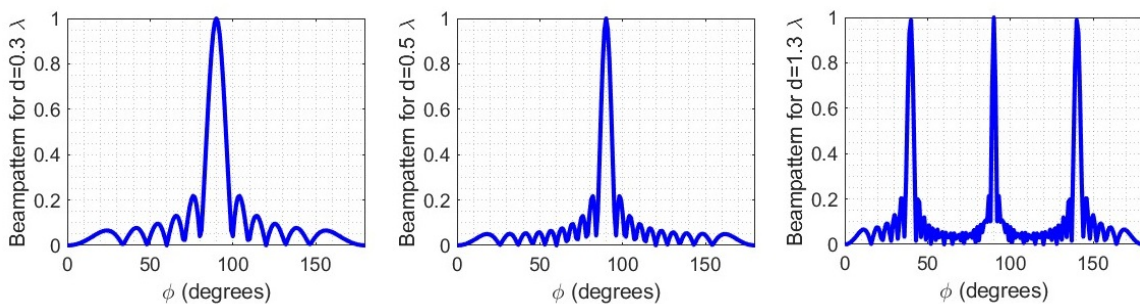


Figure 3 – Example of beampatterns for an $M = 20$ ULA beamformer steered at 90° for different distances between sensors: (left) $d = 0.3\lambda$, (center) $d = 0.5\lambda$, the most usual choice, and (right) $d = 1.3\lambda$ where we observe undesirable grating lobes. Similar to the example in [6].

2.2.3 SINR

As in [34] the signal-to-interference plus noise ratio, SINR, is a commonly accepted measure of the steady-state performance of an adaptive array. The SINR takes into account the mutual coupling between array elements and therefore can be used to study its effects in the array performance.

The SINR can be given as [34–36]:

$$\text{SINR} = \frac{\mathbf{w}^H \mathbf{R}_s \mathbf{w}}{\mathbf{w}^H \mathbf{R}_{jn} \mathbf{w}}, \quad (2.12)$$

where $\mathbf{R}_s = \mathbb{E} [\mathbf{s}(k) \mathbf{s}^H(k)]$ is SOI covariance matrix, and $\mathbf{R}_{jn} = \mathbb{E} [\mathbf{j}(k) \mathbf{j}^H(k)] + \mathbb{E} [\mathbf{n}(k) \mathbf{n}^H(k)]$ is the jammer plus noise covariance matrix. The beamformer weight coefficient vector \mathbf{w} depends on the application. In the case of known SOI and jammers,

$$\mathbf{R}_s = \sigma_{\text{SOI}}^2 \mathbf{a}(\phi_{\text{SOI}}) \mathbf{a}(\phi_{\text{SOI}})^H, \quad (2.13)$$

and:

$$\begin{aligned} \mathbf{R}_{jn} = & \sigma_{\text{JAMMER } 1}^2 \mathbf{a}(\phi_{\text{JAMMER } 1}) \mathbf{a}(\phi_{\text{JAMMER } 1})^H + \dots \\ & + \sigma_{\text{JAMMER } D-1}^2 \mathbf{a}(\phi_{\text{JAMMER } D-1}) \mathbf{a}(\phi_{\text{JAMMER } D-1})^H + \sigma_{\text{NOISE}}^2 \mathbf{I}, \end{aligned} \quad (2.14)$$

for 1 SOI and $D - 1$ jammers. σ_{SOI} is the variance of the SOI and σ_{JAMMER} is the variance of the jammer signal.

2.2.4 Adaptive Beamforming

When \mathbf{R}_x is not available, a possible solution is to estimate it from the available snapshots and perform a sample matrix inversion technique. This block data processing approach is also known as direct matrix inversion (DMI) or estimate and plug technique [4]. Therefore, a possible adaptation of the MPDR solution (2.6) is replacing \mathbf{R}_x with an estimate $\hat{\mathbf{R}}_x$ resulting in the sample matrix inversion (SMI) solution [4]:

$$\mathbf{w}_{\text{SMI}} = \frac{\hat{\mathbf{R}}_x^{-1} \mathbf{a}(\phi)}{\mathbf{a}^H(\phi) \hat{\mathbf{R}}_x^{-1} \mathbf{a}(\phi)}. \quad (2.15)$$

Equation (2.15) is a particular case of (2.9) when $\mathbf{C} = \mathbf{a}(\phi)$, $\mathbf{f} = 1$, with $\mathbf{R}_x = \hat{\mathbf{R}}_x$. SMI requires estimating the statistics and feeding the data back to the processor, thus not adapting in real time.

An ABF solution that adapts in real-time to the incoming data is, for example, a steepest descent-based algorithm such as the Constrained Least Mean Squares (CLMS) [4]. The CLMS algorithm updates the coefficient vector \mathbf{w} at every iteration, subject to $\mathbf{C}^H \mathbf{w} = \mathbf{f}$, in order to receive and enhance the SOI while attenuating possible jammers from any other direction. The CLMS update equation is given by [6]:

$$\mathbf{w}_{\text{CLMS}}(k+1) = \mathbf{P} [\mathbf{w}(k) + \mu e^*(k) \mathbf{x}(k)] + \mathbf{f}_c, \quad (2.16)$$

where $e(k) = -\mathbf{w}^H(k) \mathbf{x}(k)$ is the error, $\mathbf{P} = \mathbf{I}_{M \times M} - \mathbf{C} (\mathbf{C}^H \mathbf{C})^{-1} \mathbf{C}^H$ is a projection matrix, and $\mathbf{f}_c = \mathbf{C} (\mathbf{C}^H \mathbf{C})^{-1} \mathbf{f}$ is an $M \times 1$ quiescent vector.

2.3 Reflection and Transmission Coefficients and the Scattering Matrix

The transmission line theory is an important part of this work when it comes to mutual coupling analysis in terms of scattering parameters, as well as a base to analyze the electromagnetic simulation results. Figure 4 displays a lossless transmission line terminated in an arbitrary load impedance Z_L [37].

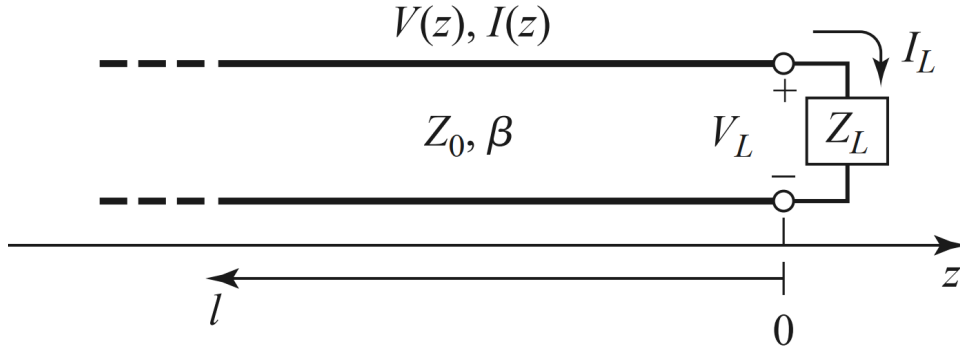


Figure 4 – A transmission line terminated in a load impedance Z_L [37].

Assuming an incident wave of the form $V_o^+ e^{-j\beta z}$ is generated from a source at $z < 0$, where β is the propagation constant for the lossless line [37]:

$$\beta = \frac{2\pi}{\lambda}, \quad (2.17)$$

$\lambda = v/f_o$ is the wavelength, v is the propagating speed in the medium, and f_o is the operating frequency. The ratio of voltage to current for such a traveling wave is Z_0 , the characteristic impedance of the line. Nevertheless, when the line is terminated in an arbitrary load $Z_L \neq Z_0$, the ratio of voltage to current at the load must be Z_L . Thus, the total voltage on a line may be written as the sum of the incident and reflected waves as in [37]:

$$V(z) = V_o^+ e^{-j\beta z} + V_o^- e^{j\beta z}, \quad (2.18)$$

and the total current on the line is described by:

$$I(z) = \frac{V_o^+}{Z_0} e^{-j\beta z} - \frac{V_o^-}{Z_0} e^{j\beta z}. \quad (2.19)$$

The total voltage and current at the load are related by the load impedance, so at $z = 0$:

$$Z_L = \frac{V(0)}{I(0)} = \frac{V_o^+ + V_o^-}{V_o^+ - V_o^-} Z_0 \quad (2.20)$$

Solving for V_o^- it yields:

$$V_o^- = \frac{Z_L - Z_0}{Z_L + Z_0} V_o^+. \quad (2.21)$$

The total voltage and current waves on the line can then be written as [37]:

$$V(z) = V_o^+ (e^{-j\beta z} + \Gamma e^{j\beta z}), \quad (2.22)$$

and

$$I(z) = \frac{V_o^+}{Z_0} (e^{-j\beta z} - \Gamma e^{j\beta z}). \quad (2.23)$$

The amplitude of the reflected voltage wave normalized to the amplitude of the incident voltage wave is defined as the voltage reflection coefficient, Γ [37]:

$$\Gamma = \frac{V_o^-}{V_o^+} = \frac{Z_L - Z_0}{Z_L + Z_0}, \quad (2.24)$$

and the return loss is a measure of reflected power defined as:

$$RL_{\text{dB}} = -20 \log |\Gamma|. \quad (2.25)$$

If $Z_L = Z_0$ it results in $\Gamma = 0$ and $RL = -\infty$ dB and no power is reflected, meaning the load is *matched* to the line. On the other hand, if $|Z_L| \gg |Z_0|$ or $|Z_L| \ll |Z_0|$ it results in $|\Gamma| = 1$ and $RL = 0$ dB, meaning that all the incident power is reflected at the load [37]. When the load is not matched to the line there is superposition of incident and reflected waves often called standing waves [37], and usually a part of the wave is transmitted onto the load with a voltage amplitude given by a transmission coefficient. The transmission coefficient is given by:

$$T = 1 + \Gamma = 1 + \frac{Z_L - Z_0}{Z_L + Z_0} = \frac{2Z_L}{Z_L + Z_0}, \quad (2.26)$$

and is expressed in dB by the insertion loss:

$$IL_{\text{dB}} = -20 \log |T|. \quad (2.27)$$

The scattering matrix is a comprehensive representation of a N -port network, describing its behavior as observed at its N ports. Unlike the impedance and admittance matrices, which relate the voltages and currents at the ports, the scattering matrix establishes the relationship between the voltage waves arriving at the ports and those reflected back from them [37]. Consider an arbitrary N -port network illustrated as an example, where V_n^+ represents the amplitude of the voltage wave approaching port n , and V_n^- represents the amplitude of the voltage wave reflected from port n . The scattering

matrix, denoted as \mathbf{S} , is defined based on the relationship between those incident and reflected voltage waves as [37]:

$$\begin{bmatrix} V_1^- \\ V_2^- \\ \vdots \\ V_N^- \end{bmatrix} = \begin{bmatrix} S_{11} & S_{12} & \cdots & S_{1N} \\ S_{21} & & & \vdots \\ \vdots & & \ddots & \\ S_{N1} & \cdots & & S_{NN} \end{bmatrix} \begin{bmatrix} V_1^+ \\ V_2^+ \\ \vdots \\ V_N^+ \end{bmatrix}, \quad (2.28)$$

or:

$$\mathbf{V}^- = \mathbf{S}\mathbf{V}^+. \quad (2.29)$$

Hence, a specific element of the scattering matrix is defined as:

$$S_{ij} = \left. \frac{V_i^-}{V_j^+} \right|_{V_q^+ = 0 \text{ for } q \neq j} \quad (2.30)$$

Equation (2.30) means that S_{ij} is achieved by driving port j with an incident wave of voltage V_j^+ and measuring the reflected wave amplitude V_i^- coming out of port i . The incident waves on all ports, except the j th port, are set to have zero wave amplitude, meaning that all other ports must be terminated with matched loads to avoid reflections. Therefore, assuming that all other ports are terminated in matched loads, S_{ii} represents the reflection coefficient observed at port i , and S_{ij} represents the transmission coefficient from port j to port i [37].

If we consider an M -elements antenna array as an M -ports network [21,27], the S_{ii} in the antenna terminal i , when all other terminals are matched, represents a measurement of reflected voltage from the antenna to the referred terminal, which is a very small number when they are matched. If measured in dB as in Equation (2.25), the S_{ii} represents minus the return loss or the amount of power reflected back to the antenna terminal. Analogously, the S_{ij} represents a measurement of transmitted voltage from terminal j to terminal i . If measured in dB as in Equation (2.27), the S_{ij} represents minus the insertion loss or the amount of power transmitted between the antennas and therefore provides insight about the coupling degree between the antenna elements.

3 SIDELOBE SUPPRESSION

3.1 Literature Review concerning Sidelobe Suppression

Sidelobe suppression has been a goal of current research efforts by the scientific community in both radar and communications fields [38–44]. SLL control may improve the signal-to-interference plus noise ratio. Also, minimizing the sidelobes may reduce the susceptibility to undesired radio frequency interference [7], which may be significant when receiving a considerable number of new jammers added to the electromagnetic scenario [8]. Recent work has used ABF to control and suppress interference, as seen in [45–49]. ABF algorithms using remaining degrees of freedom on the linear constraints to reduce interference are proposed in [50]. However, an adaptive beamforming is usually not oriented to control the sidelobe levels. Optimization techniques have been used to control the sidelobe level and optimize the radiation pattern as in [9–12].

The work in [8] presents a strategy, to, in parallel to an ABF technique, achieve a specified sidelobe level, improving SINR and directivity. Its flowchart is presented in Figure 5. According to [8], it reduces sidelobe level by placing radiation pattern nulls in the direction of the greatest sidelobes. The purpose is to become less susceptible to unpredicted interference signals, improving the SINR [8]. The BF calculates the weight coefficient vector, plots the beam pattern (BP), finds the greatest sidelobe, and, if its level surpasses a specified minimum, it creates an additional interfering signal and a null towards the sidelobe direction. After that, it employs the BF technique to calculate new weights and the new beam pattern. The algorithm is applied on MPDR, SMI, and Recursive Least Squares (RLS) beamforming techniques, and is tested for several DOA. Our approach shall take advantage of the idea proposed in [8], however proposing an executable algorithm employing, instead of interfering signals, linear constraints to optimum and adaptive filters.

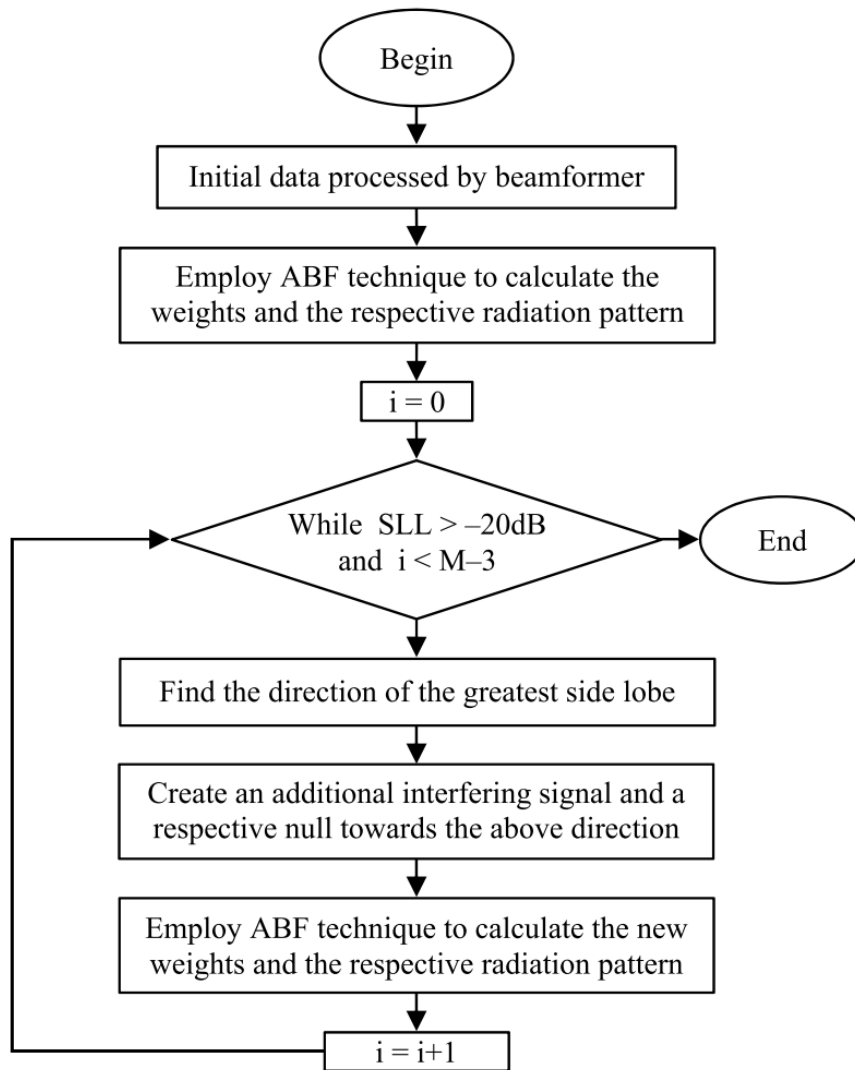


Figure 5 – Flowchart of the proposed sidelobe suppression approach from [8].

3.2 Methodology concerning Sidelobe Suppression

As previously detailed the main objective concerning SLS in this work is to explore and extend null placement sidelobe suppression to adaptive beamformers, proposing new approaches that employ constrained adaptive algorithms. The methodology used for achieving this objective is displayed in Figure 6. The main steps are explained below:

1. The work started with a literature review concerning the state of the art in sidelobe suppression and constrained adaptive filters.
2. A realistic beamformer architecture, which is composed of a receiver and an array processor, was defined. It is displayed in Figure 1. It allows the simulation of the array signals' reception through an analog and digital receiver, followed by the beamforming in the array signal processor.

3. The adaptive filter theory was explored with a focus on using linear constraints into an ABF.
4. A peak-finder routine was employed to determine the angular direction of the second-greatest lobe, i.e., the greatest sidelobe.
5. The main SL direction is converted into a steering vector (SV) to be used as an additional linear restriction to perform a null in that direction.
6. An expression was derived to add additional restrictions to adaptive filters.
7. The algorithm's strategy was defined, i.e., the moment when the NP-SLS would act in the ABF.
8. The algorithms to perform NP-SLS to optimum and adaptive beamformers were developed.
9. Experiments were performed to evaluate the effectiveness of the NP-SLS technique in terms of suppressed sidelobe level, confidence interval analysis, number of required loops to achieve an SLL, SINR, among others.

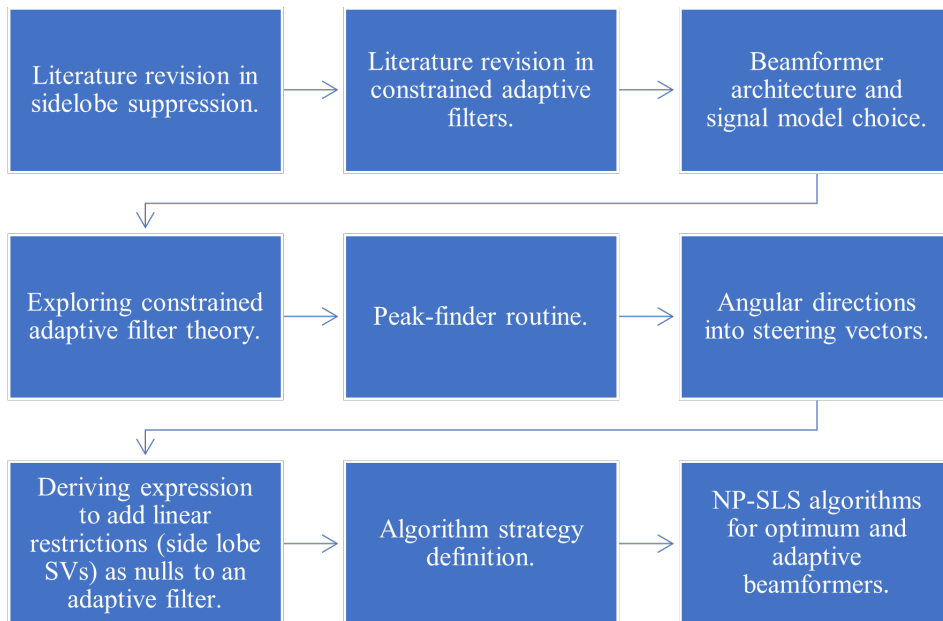


Figure 6 – Methodology used concerning Sidelobe Suppression.

3.3 The NP-SLS MPDR Algorithm

Our sidelobe suppression proposal for optimum beamformers is the null placement sidelobe suppression MPDR algorithm (NP-SLS MPDR), shown in Algorithm 1. Using the covariance matrix and the SOI steering vector as inputs, and initializing with the MPDR coefficient vector, it calculates the MPDR beampattern. After that, it detects the greatest sidelobe level and incorporates an additional restriction to the linear adaptive filter in the form of an SV with the SL direction. This additional restriction reduces the detected SLL by placing a null on its direction. It stops when the sidelobe level is smaller than a specified amount $SLL < SLL_{min}$ [51].

Algorithm 1 The NP-SLS MPDR Beamformer

Input data: \mathbf{R}_x ▷ Theoretical Covariance matrix
 $\mathbf{a}(\phi_1)$ ▷ SOI Steering Vector

Initialization:

$$\mathbf{w}_{\text{MPDR}} = \frac{\mathbf{R}_x^{-1} \mathbf{a}(\phi_1)}{\mathbf{a}^H(\phi_1) \mathbf{R}_x^{-1} \mathbf{a}(\phi_1)}$$

$$\text{BP}_{\text{MPDR}}(\phi) = |\mathbf{w}_{\text{MPDR}}^H \mathbf{a}(\phi)|$$
▷ $\forall \phi \in$ visible region

From the peaks of $\text{BP}_{\text{MPDR}}(\phi)$, find SL and ϕ_{SL}

$$\mathbf{C} \leftarrow [\mathbf{a}(\phi_1) \quad \mathbf{a}(\phi_{\text{SL}})]$$

$$\mathbf{f} \leftarrow [1 \quad 0]^T$$

$$\mathbf{w}_{\text{NP-SLS}} \leftarrow \mathbf{w}_{\text{MPDR}}$$

$$NrLoops \leftarrow 0$$

Choose: SLL_{min}

while $SLL > SLL_{min}$ **do**

$$NrLoops \leftarrow NrLoops + 1$$

$$\mathbf{w}_{\text{NP-SLS}} \leftarrow \mathbf{R}_x^{-1} \mathbf{C} (\mathbf{C}^H \mathbf{R}_x^{-1} \mathbf{C})^{-1} \mathbf{f}$$

$$\text{BP}_{\text{MPDR}}(\phi) = |\mathbf{w}_{\text{NP-SLS}}^H \mathbf{a}(\phi)|$$

From the peaks of $\text{BP}_{\text{MPDR}}(\phi)$, find SL and ϕ_{SL}

$$\mathbf{C} \leftarrow [\mathbf{C} \quad \mathbf{a}(\phi_{\text{SL}})]$$

$$\mathbf{f} \leftarrow [\mathbf{f}^T \quad 0]^T$$

end

3.4 Using the NP-SLS with an Adaptive Filter

For the adaptive beamformer case, this master thesis proposes the NP-SLS ABF solution [51]. The NP-SLS algorithm receives the updated weight vector \mathbf{w}_B from the ABF, along with the restriction vectors \mathbf{C} and \mathbf{f} . After that, it detects the sidelobe with the greatest sidelobe level and incorporates an SV for the direction of the SL as an additional linear restriction to the linear adaptive filter. This originates an updated weight vector \mathbf{w}_A . Figure 7 depicts the problem from a geometric perspective.

\mathcal{H}_0 hyperspace contains the vectors that are subject to $\mathbf{C}^H \mathbf{w} = \mathbf{f}$, i.e. the vectors \mathbf{w}_B that incorporate the restrictions from the ABF loop. \mathcal{H}_1 hyperspace contains the

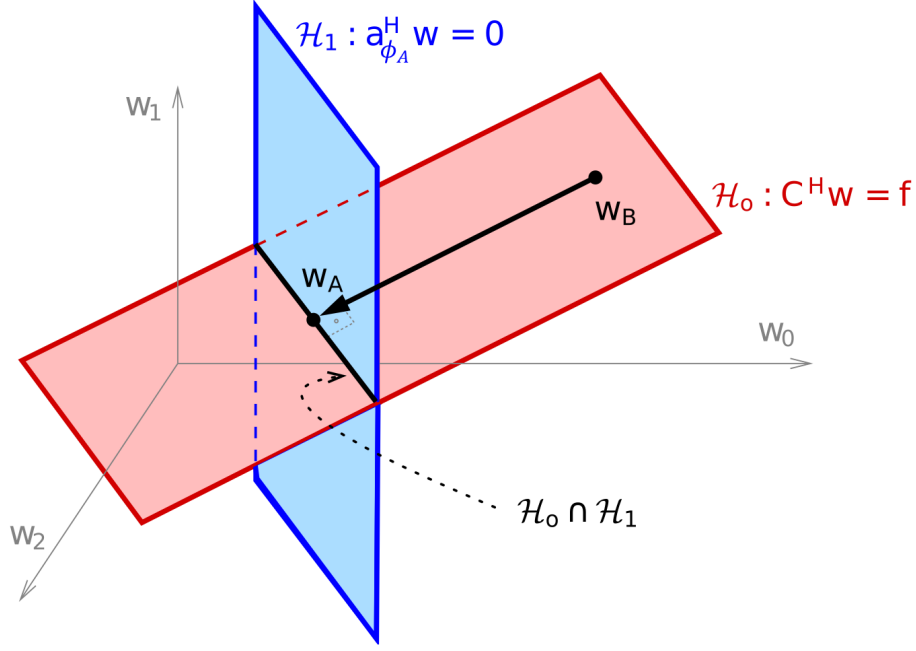


Figure 7 – In the NP-SLS Algorithm loops, when used with an adaptive beamformer, our approach entails iteratively updating coefficients from the previous vector (\mathbf{B} as in before) $\mathbf{w}_B \in \mathcal{H}_0$ to the closest vector (\mathbf{A} as in after) such that $\mathbf{w}_A \in \mathcal{H}_0 \cap \mathcal{H}_1$, the intersection of hyperspaces \mathcal{H}_0 and \mathcal{H}_1 .

vectors that are subject to $\mathbf{a}_{\phi_A}^H \mathbf{w} = 0$, i.e., the vector \mathbf{w}_A that results in a BP with a null on the ϕ_A direction. The objective, from a geometric point of view, is to find the vector that is the result of minimizing the distance between \mathbf{w}_B and \mathbf{w}_A (B standing for "Before" and A standing for "After"), also known as the minimum disturbance approach. To derive an update expression for this step, we define an additional constraint matrix denoted as $\mathbf{C}_A = [\mathbf{C} \ \mathbf{a}_{\phi_A}]$. The expression for \mathbf{w}_A is then obtained from minimizing the following objective function subject to a set of linear equations:

$$\min_{\mathbf{w}} \|\mathbf{w} - \mathbf{w}_B\|^2 \text{ subject to } \mathbf{C}_A^H \mathbf{w} = \begin{bmatrix} \mathbf{f} \\ 0 \end{bmatrix}. \quad (3.1)$$

Applying Lagrange multipliers, this constraint may be written as:

$$\mathcal{L}(\mathbf{w}, \boldsymbol{\lambda}) = \|\mathbf{w} - \mathbf{w}_B\|^2 + \text{Re}[\boldsymbol{\lambda}^H (\mathbf{C}_A^H \mathbf{w} - \mathbf{f}_A)], \quad (3.2)$$

where:

$$\mathbf{C}_A = \begin{bmatrix} \mathbf{C} & \mathbf{a}_{\phi_A} \end{bmatrix}. \quad (3.3)$$

This is equivalent to:

$$\mathcal{L}(\mathbf{w}, \boldsymbol{\lambda}) = \|\mathbf{w} - \mathbf{w}_B\|^2 + \text{Re}[(\mathbf{C}_A \boldsymbol{\lambda})^H \mathbf{w}] - \text{Re}[\boldsymbol{\lambda}^H \mathbf{f}_A], \quad (3.4)$$

or to:

$$\mathcal{L}(\mathbf{w}, \boldsymbol{\lambda}) = \|\mathbf{w} - \mathbf{w}_B\|^2 + \text{Re}[\mathbf{w}^H \mathbf{C}_A \boldsymbol{\lambda}] - \text{Re}[\boldsymbol{\lambda}^H \mathbf{f}_A], \quad (3.5)$$

Deriving first with relation to \mathbf{w}^* :

$$\frac{\partial(\|\mathbf{w} - \mathbf{w}_B\|^2)}{\partial \mathbf{w}^*} = \frac{\partial(\mathbf{w}^H \mathbf{w} - 2\mathbf{w}^H \mathbf{w}_B + \mathbf{w}_B^H \mathbf{w}_B)}{\partial \mathbf{w}^*} = 2(\mathbf{w} - \mathbf{w}_B), \quad (3.6)$$

and

$$\frac{\partial(\text{Re}[(\mathbf{w})^H \mathbf{C}_A \boldsymbol{\lambda}] - \text{Re}[\boldsymbol{\lambda}^H \mathbf{f}_A])}{\partial \mathbf{w}^*} = \frac{1}{2} \mathbf{C}_A \boldsymbol{\lambda}, \quad (3.7)$$

Setting the gradient to zero:

$$2(\mathbf{w}_A - \mathbf{w}_B) + \frac{1}{2} \mathbf{C}_A \boldsymbol{\lambda} = 0 + j0. \quad (3.8)$$

Solving for \mathbf{w}_A :

$$\mathbf{w}_A = \mathbf{w}_B - \frac{1}{4} \mathbf{C}_A \boldsymbol{\lambda}. \quad (3.9)$$

Second, deriving with relation to vector $\boldsymbol{\lambda}$:

$$\mathcal{L}(\mathbf{w}, \boldsymbol{\lambda}) = \|\mathbf{w} - \mathbf{w}_B\|^2 + \text{Re}[\boldsymbol{\lambda}^H \mathbf{C}_A^H \mathbf{w}] - \text{Re}[\boldsymbol{\lambda}^H \mathbf{f}_A], \quad (3.10)$$

$$\frac{\partial(\mathcal{L}(\mathbf{w}, \boldsymbol{\lambda}))}{\partial \boldsymbol{\lambda}^*} = 0 + \frac{1}{2} \mathbf{C}_A^H \mathbf{w}_A - \frac{1}{2} \mathbf{f}_A \quad (3.11)$$

Setting the gradient to zero:

$$\mathbf{C}_A^H \mathbf{w}_A - \mathbf{f}_A = 0 + j0, \quad (3.12)$$

which is our constraint itself. Substituting Eq. 3.9 into 3.12 we achieve:

$$\mathbf{C}_A^H \left(\mathbf{w}_B - \frac{1}{4} \mathbf{C}_A \boldsymbol{\lambda} \right) = \mathbf{f}_A, \quad (3.13)$$

which yields:

$$\mathbf{C}_A^H \mathbf{w}_B - \frac{1}{4} \mathbf{C}_A^H \mathbf{C}_A \boldsymbol{\lambda} = \mathbf{f}_A, \quad (3.14)$$

and results in:

$$\mathbf{C}_A^H \mathbf{C}_A \boldsymbol{\lambda} = 4 \left(\mathbf{C}_A^H \mathbf{w}_B - \mathbf{f}_A \right). \quad (3.15)$$

Solving for $\boldsymbol{\lambda}$ it results in:

$$\boldsymbol{\lambda} = 4 \left(\mathbf{C}_A^H \mathbf{C}_A \right)^{-1} \left(\mathbf{C}_A^H \mathbf{w}_B - \mathbf{f}_A \right). \quad (3.16)$$

Substituting Eq. 3.16 into Eq. 3.9:

$$\mathbf{w}_A = \mathbf{w}_B - \frac{1}{4} \mathbf{C}_A \left[4 \left(\mathbf{C}_A^H \mathbf{C}_A \right)^{-1} \left(\mathbf{C}_A^H \mathbf{w}_B - \mathbf{f}_A \right) \right], \quad (3.17)$$

and finally:

$$\mathbf{w}_A = \mathbf{w}_B - \mathbf{C}_A \left(\mathbf{C}_A^H \mathbf{C}_A \right)^{-1} \left(\mathbf{C}_A^H \mathbf{w}_B - \mathbf{f}_A \right), \quad (3.18)$$

Or:

$$\mathbf{w}_A = \mathbf{w}_B - \mathbf{C}_A (\mathbf{C}_A^H \mathbf{C}_A)^{-1} \left([\mathbf{C} \ \mathbf{a}_{\phi_A}]^H \mathbf{w}_B - \begin{bmatrix} \mathbf{f} \\ 0 \end{bmatrix} \right). \quad (3.19)$$

Since $\mathbf{C}^H \mathbf{w}_B = \mathbf{f}$ we can simplify $[\mathbf{C} \ \mathbf{a}_{\phi_A}]^H \mathbf{w}_B$ to:

$$[\mathbf{C} \ \mathbf{a}_{\phi_A}]^H \mathbf{w}_B = \begin{bmatrix} \mathbf{C}^H \mathbf{w}_B \\ \mathbf{a}_{\phi_A}^H \mathbf{w}_B \end{bmatrix} = \begin{bmatrix} \mathbf{f} \\ \mathbf{a}_{\phi_A}^H \mathbf{w}_B \end{bmatrix}. \quad (3.20)$$

Therefore:

$$\begin{bmatrix} \mathbf{f} \\ \mathbf{a}_{\phi_A}^H \mathbf{w}_B \end{bmatrix} - \begin{bmatrix} \mathbf{f} \\ 0 \end{bmatrix} = \begin{bmatrix} 0 \\ \mathbf{a}_{\phi_A}^H \mathbf{w}_B \end{bmatrix} \quad (3.21)$$

and finally substituting back into Eq. 3.19 we achieve:

$$\mathbf{w}_A = \mathbf{w}_B - \mathbf{C}_A (\mathbf{C}_A^H \mathbf{C}_A)^{-1} \begin{bmatrix} 0 \\ \mathbf{a}_{\phi_A}^H \mathbf{w}_B \end{bmatrix} \quad (3.22)$$

or:

$$\mathbf{w}_A = \mathbf{w}_B + \mathbf{C}_A (\mathbf{C}_A^H \mathbf{C}_A)^{-1} \begin{bmatrix} 0 & -\mathbf{a}_{\phi_A} \end{bmatrix}^H \mathbf{w}_B. \quad (3.23)$$

This is a possible solution to this problem as the one published in [7]. With the previous result, we iterate the NP-SLS technique as in Algorithm 3.

3.4.1 The NP-SLS Algorithm for an ABF

The NP-SLS CLMS, Algorithm 2, is a proposed solution for the CLMS ABF. It is noteworthy to mention that the CLMS was used as an example, and any other ABF techniques may be used, including the Constrained Normalized LMS (CNLMS) and the Constrained Conjugate Gradient (CCG) [52] algorithms, among others. Figure 8 presents a schematic of the strategy of Algorithm 2.

It uses the SLS Algorithm 3 as a function. Based on the constraints, it calculates the CLMS projection matrix and the quiescent weight vector, \mathbf{f}_c , as initialization. After that, it updates the CLMS weight vector based on the snapshot on each iteration, up to the end of the sample block with K snapshots. After K snapshots, the algorithm is divided into two versions. Version 1 calls for Algorithm 3, which performs the SLL control returning the updated weight vector and keeps the single restriction given as the SOI SV. Version 2 also calls for Algorithm 3 to perform the SLL reduction; however, it returns all additional restrictions generated by Algorithm 3 and not only the SOI SV restriction. One can notice that the NP-SLS technique is only employed in between sample blocks, reducing the Algorithm's computational complexity, as shall be detailed further in this text.

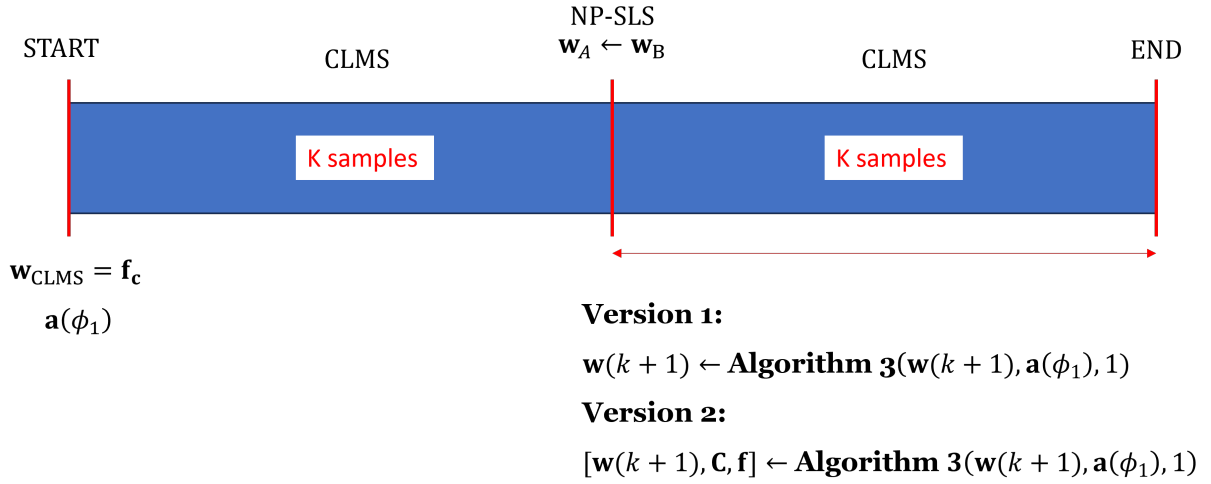


Figure 8 – Strategy of the CLMS Algorithm with NP-SLS.

Algorithm 2 The CLMS Algorithm with NP-SLS**Input data:** $\mathbf{x}(k)$

▷ Snapshots

Initialization:

$$\mathbf{C} = \mathbf{a}(\phi_1)$$

$$\mathbf{f} = 1$$

$$\mathbf{P} = \mathbf{I}_{M \times M} - \mathbf{C}(\mathbf{C}^H \mathbf{C})^{-1} \mathbf{C}^H$$

$$\mathbf{f}_c = \mathbf{C}(\mathbf{C}^H \mathbf{C})^{-1} \mathbf{f}$$

$$\mathbf{w}(k) = \mathbf{f}_c$$

▷ ϕ_1 is the DOA of the SOI

▷ Distortionless constraint

▷ M sensors

▷ Quiescent weight vector

Choose: μ (step-size) and K (sample block)**for each** k **do**

$$y(k) = \mathbf{w}^H(k) \mathbf{x}(k)$$

$$e(k) = 0 - y(k)$$

$$\mathbf{w}(k+1) = \mathbf{P} [\mathbf{w}(k) + \mu e^*(k) \mathbf{x}(k)] + \mathbf{f}_c$$

if $\text{mod}(k, K) = 0$ **do****Version 1:**

$$\mathbf{w}(k+1) \leftarrow \text{Algorithm 3}(\mathbf{w}(k+1), \mathbf{a}(\phi_1), 1)$$

Version 2:

$$[\mathbf{w}(k+1), \mathbf{C}, \mathbf{f}] \leftarrow \text{Algorithm 3}(\mathbf{w}(k+1), \mathbf{a}(\phi_1), 1)$$

$$\mathbf{P} = \mathbf{I}_{M \times M} - \mathbf{C}(\mathbf{C}^H \mathbf{C})^{-1} \mathbf{C}^H$$

$$\mathbf{f}_c = \mathbf{C}(\mathbf{C}^H \mathbf{C})^{-1} \mathbf{f}$$

end**end**

Algorithm 3 The NP-SLS Algorithm Applied to an ABF

Input data: \mathbf{w}_{ABF} , \mathbf{C} and \mathbf{f}
Initialization:

$$\text{BP}_{\text{ABF}}(\phi) = |\mathbf{w}_{\text{ABF}}^{\text{H}} \mathbf{a}(\phi)|$$

 $\triangleright \forall \phi \in \text{visible region}$

 From the peaks of $\text{BP}_{\text{ABF}}(\phi)$, find SLL and ϕ_{SL}

$$NrLoops \leftarrow 0$$

Choose: SLL_{\min}
while $\text{SLL} > \text{SLL}_{\min}$ **do**

$$NrLoops \leftarrow NrLoops + 1$$

$$\mathbf{C}_A \leftarrow [\mathbf{C} \quad \mathbf{a}(\phi_{\text{SL}})]$$

$$\mathbf{f}_A \leftarrow [\mathbf{f}^{\text{T}} \quad 0]^{\text{T}}$$

$$\mathbf{w}_{\text{NP-SLS}} \leftarrow \frac{1}{2} \mathbf{w}_{\text{ABF}} + \dots$$

$$\frac{1}{2} \mathbf{C}_A (\mathbf{C}_A^{\text{H}} \mathbf{C}_A)^{-1} [\mathbf{C} \quad -\mathbf{a}(\phi_{\text{SL}})]^{\text{H}} \mathbf{w}_{\text{ABF}}$$

$$\text{BP}_{\text{NP-SLS}}(\phi) = |\mathbf{w}_{\text{NP-SLS}}^{\text{H}} \mathbf{a}(\phi)|$$

 From the peaks of $\text{BP}_{\text{NP-SLS}}(\phi)$, find SLL and ϕ_{SL}

$$\mathbf{C} \leftarrow \mathbf{C}_A$$

$$\mathbf{f} \leftarrow \mathbf{f}_A$$

end
Returns: $\mathbf{w}_{\text{NP-SLS}}$, and, in the case of Version 2, also \mathbf{C} and \mathbf{f}

3.5 Sidelobe Suppression Results

In order to simulate the response of the proposed Algorithms 1 and 2 for sidelobe suppression, two stationary signals have been generated and processed following the signal model from Equation (2.5), and parameters and architecture from Figure 1, received by a ULA. The distance between the array elements is $d = \lambda/2$.

Figures 9 and 10 depict a confidence interval experiment of the NP-SLS MPDR algorithm. The SOI is fixed at 45° and the jammer ranges from 0 to 30° and from 60 to 180° , representing jammers not too close to the SOI in order to avoid causing beamforming distortion due to their proximity. The simulations have been performed for each angle within a step size of 5° and for each of the specific number of elements $M = 8, 10, 12, 15, 20, 25, 30, 35, 40, 45, 50$: to represent the behavior for different M . Figure 9 displays the final minimum SLL level versus the number of array elements M . Figure 10 displays the number of necessary loops for obtaining SLL_{\min} versus M . As seen in Figure 9, the final minimum SLL level decreases dramatically with the rise of M . However, even for low values of M , e.g. $M = 8$, it performs reasonable SL attenuation ranging from approximately -12 to -20 dB. The variation of attenuation can be considered quite large for lower M , even slightly outside the 95% confidence interval for $M \leq 30$. As seen in Figure 10, the variation of the amount of necessary loops decreases with the increase of M . However, as also seen in Figure 10, not even for higher values of M is the 95% confidence interval respected for the number of loops necessary to reach the minimum SLL. The confidence for the minimum SLL for lower values of M is low, but increases significantly with the number of array elements.

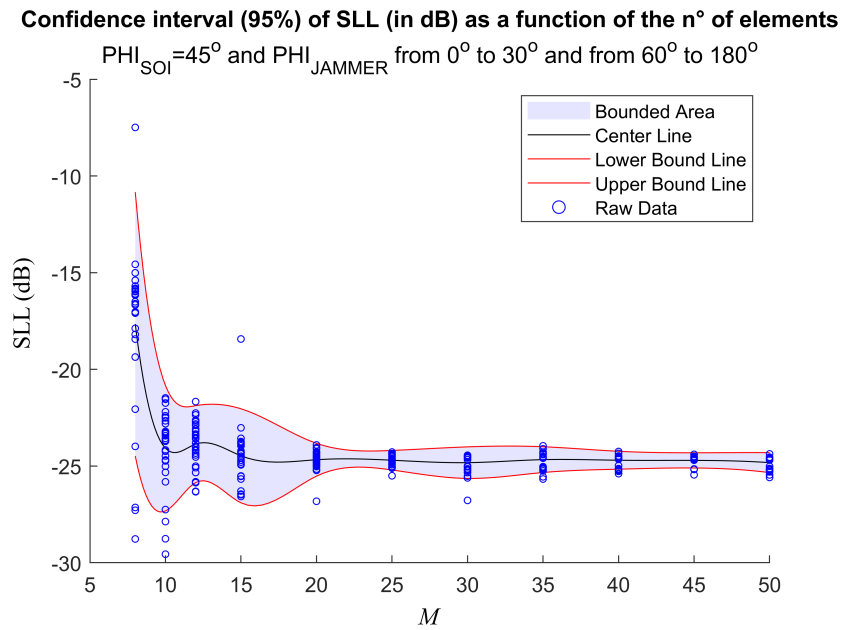


Figure 9 – Confidence interval analysis of the NP-SLS MPDR algorithm. The SOI is fixed at 45° and the jammer ranges from 0 to 30° and from 60 to 180° , representing the cases of jammer DOAs not too close to the SOI DOA. It displays the minimum final SLL level versus the number of array elements M .

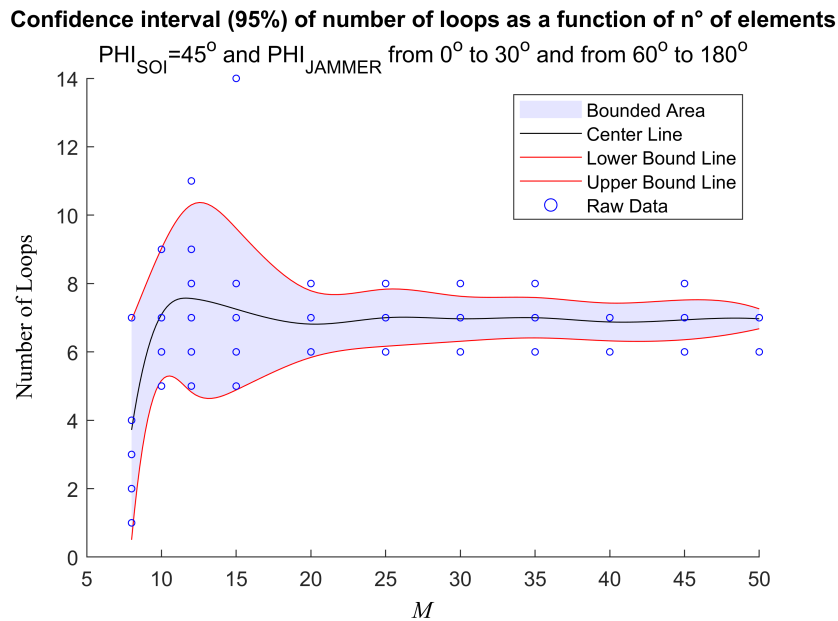


Figure 10 – Confidence interval analysis of the NP-SLS MPDR algorithm. The SOI is fixed at 45° and the jammer ranges from 0 to 30° and from 60 to 180° , representing the cases of jammer DOAs not too close to SOI DOA. It displays the number of required loops.

For the following experiments in this Section the array has $M = 8$ elements, the first signal is the SOI, generated as coming from the direction of 45° , and the second signal is the jammer, coming from 135° .

Figure 11 depicts the BP performance of the NP-SLS CLMS Algorithms, Versions 1 and 2, for a 23,000 snapshots block, initialized with the quiescent weight vector (\mathbf{f}_c). As seen in Figure 11 (a), the CLMS algorithm was initialized with the quiescent weight vector which, for this example, has a sidelobe in the direction of the jammer. In Figure 11

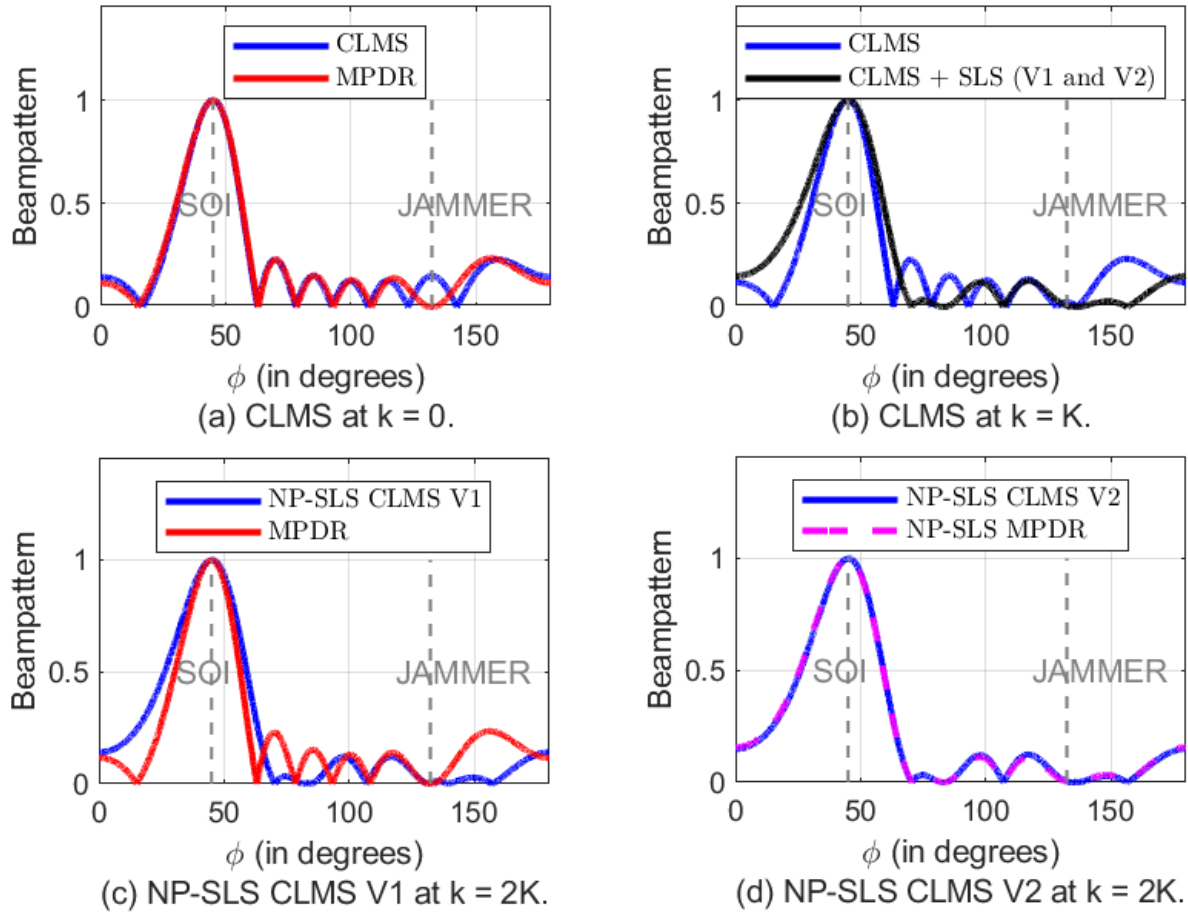


Figure 11 – Comparing the performance of the NP-SLS CLMS Algorithms, Versions 1 and 2, for a block with $K = 23,000$ snapshots. Note that the beampatterns at the end of the first block, after sidelobe suppression, are identical in both versions.

(b), the CLMS algorithm, after $K = 23,000$ snapshots, converges to a beampattern quite close to the MPDR solution, with a large attenuation towards the DOA of the jammer. Observe that, after sidelobe suppression, the SLL decreases at the expense of an increase in the main lobe beamwidth. Figures 11 (c) and (d) depict the behavior of the NP-SLS CLMS Algorithm Versions 1 and 2 at the end of the second block, after $k = 2K$ snapshots. Both versions do not change much its beampattern from the beginning of the block and clearly attenuate the jammer's DOA. Version 1, however, keeping only the distortionless response, would converge again to the MPDR solution, given more snapshots. Version

2, given more snapshots, would not converge to the MPDR solution but to the NP-SLS MPDR solution, which is the MPDR with SOI SV and 4 additional constraints from the 4 sidelobes attenuated, when $k = K$. In a general sense, both versions have attenuated the sidelobes in average over -16.5 dB, for over 100 repetitions, while maintaining the null on the jammer and zero attenuation on the SOI. Therefore, the average front-to-side lobe ratio, as known by the antennas community, is over -16.5 dB for the given experiment with $M = 8$.

Figure 12 (a) displays the SINR performance of the NP-SLS CLMS Algorithms,

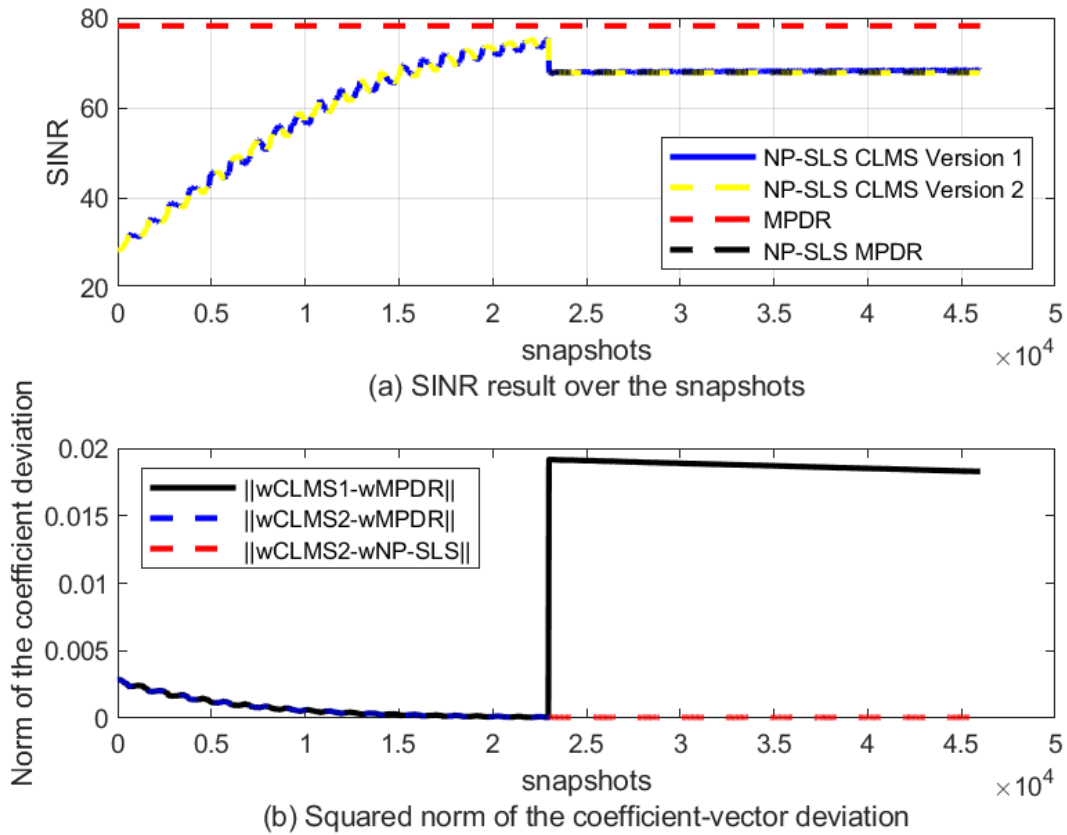


Figure 12 – Comparing SINR and the squared norm deviation of the coefficient vectors of the NP-SLS CLMS Algorithms, Versions 1 and 2, for a block with $K = 23,000$ snapshots.

Versions 1 and 2, for the 23,000 snapshots blocks 1 and 2, as described in Figure 11.

Figure 12 (b) displays the squared norm coefficient vector deviations, where the coefficient vectors are: $\mathbf{w}_{\text{CLMS1}}$ and $\mathbf{w}_{\text{CLMS2}}$ for NP-SLS CLMS Versions 1 and 2, \mathbf{w}_{MPDR} for MPDR, and $\mathbf{w}_{\text{NP-SLS}}$ for NP-SLS MPDR algorithms. As seen in Figure 12 (a), in block 1 the SINR increases for both NP-SLS CLMS Version 1 and 2 at the same pace, since they are identical in this first block. In block 2, after sidelobe suppression, both versions present a SINR decrease of around 0.6 dB. We can see in Figure 12 (a) that after the sidelobe suppression,

the SINR from both Version 1 and 2 increase, the first at a faster rate than the second. They show, however, a lower SINR increase rate than before SL suppression (on the first block). Given more snapshots, Version 1 would converge to the MPDR while Version 2 would converge to the already quite close NP-SLS MPDR SINR with the 4 nulls of the restrictions. Figure 13 displays an amplified view of the SINR performance over time, as in Figure 12 (a), but with $K = 2,000,000$ snapshots to show the convergence behavior.

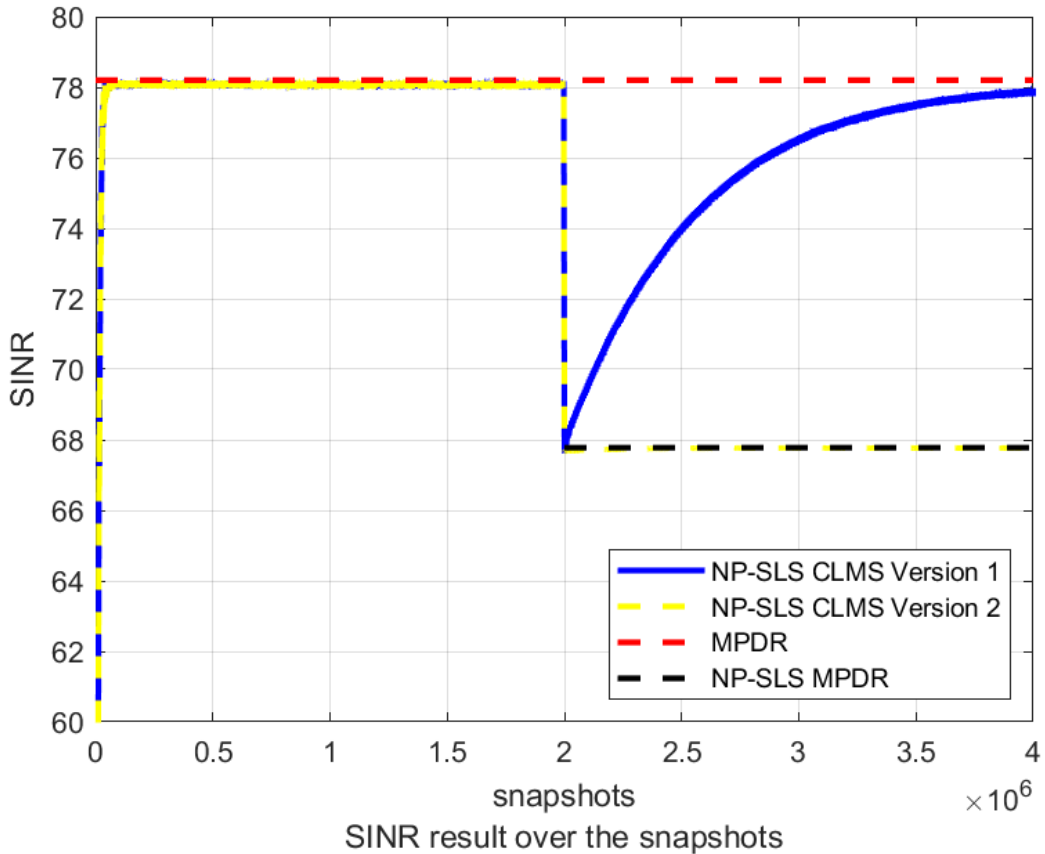


Figure 13 – SINR performance of the NP-SLS CLMS Algorithms, Versions 1 and 2, for 2,000,000 snapshots.

As seen in Figure 12 (b), in the first block the coefficient vector deviations from Versions 1 and 2 to MPDR decrease and converge to zero. In the second block, after sidelobe suppression, the deviation of Version 1 to MPDR increases by a positive degree and starts to reduce, reaching zero given sufficient time. This is coherent with Version 1's SINR increase and future convergence to MPDR given more snapshots. The Version 2 coefficient vector deviation, after SLL suppression, is compared now to NP-SLS MPDR due to its additional constraints and no longer to the distortionless constrained MPDR. It reaches zero right after the SLL suppression.

Figure 14 depicts the SINR performance and squared norm deviation of the

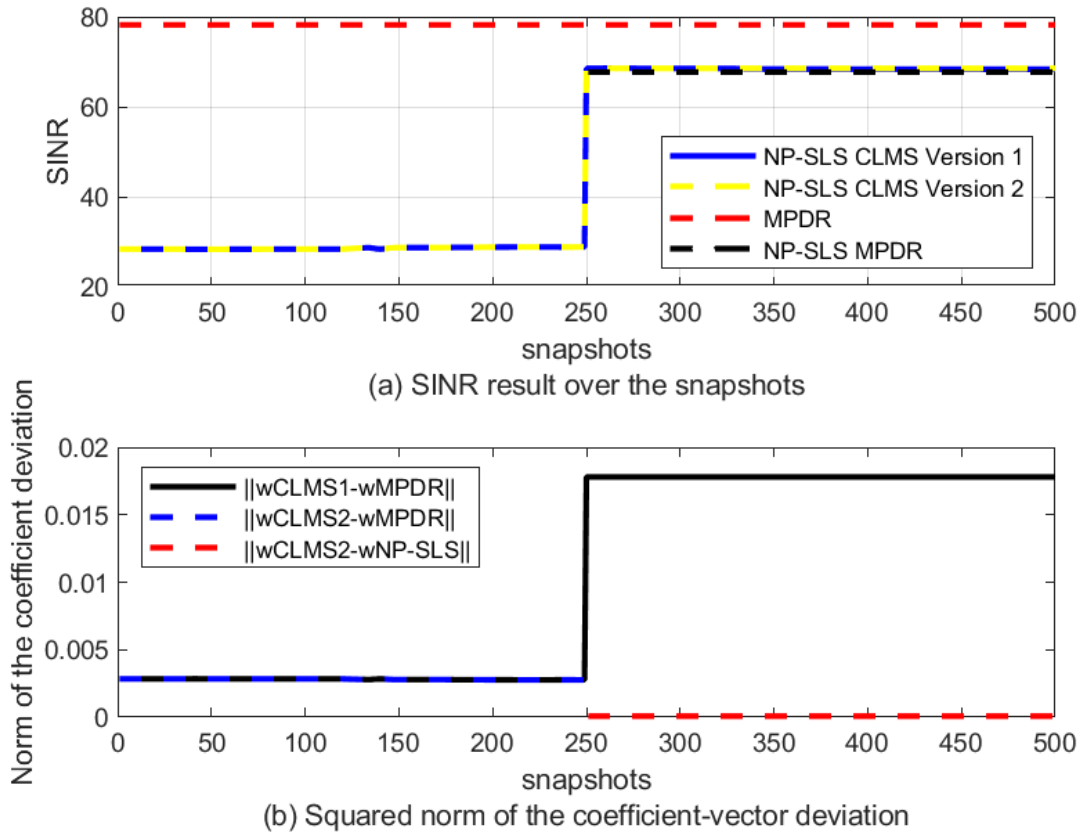


Figure 14 – Comparing SINR and the squared norm deviation of the coefficient vectors of the NP-SLS CLMS Algorithms, Versions 1 and 2, for a block with $K = 250$ snapshots.

NP-SLS CLMS Algorithms, for a shorter sample block of 250 snapshots. As seen in Figure 14 (a), the SINR does not significantly increase in block 1 due to short time. However, in block 2, after sidelobe suppression, both versions present a relevant positive degree of around 3.8 dB. The Beampattern for $K = 250$ is the same as in Figures 11 (a) and (b) for Versions 1 and 2. Therefore, the NP-SLS improves the SINR when the time is too short for CLMS to converge. As seen in Figure 14 (b), in the first block the coefficient vector deviations from Versions 1 and 2 to MPDR do not decrease due to short time. In the second block, after sidelobe suppression, the deviation of Version 1 to MPDR increases by a positive degree and would reduce given time. At the second block, the deviation from Version 2 to NP-SLS MPDR is already zero from the start of the block and the deviation from Version 2 to MPDR is not plotted since it is no longer relevant. Finally, the findings from Figures 12 and 14(a) and (b) above point out that in the case of a longer sample block (e.g. 23,000 snapshots), the sidelobe suppression comes with a cost of reducing the global SINR, in our example by at least 0.6 dB, and possibly slowing convergence. However, in the case of a shorter sample block (e.g. 250 snapshots), the sidelobe suppression would

improve SINR when the ABF still did not converge. In other words, it is a trade-off of global SINR and convergence speed versus reducing unexpected jammers at the higher sidelobes, which could also impact the SINR. With additional simulations, we confirmed that the NP-SLS Version 1 converges to the MPDR optimum solution while Version 2, incorporating the additional constraints, converges to the NP-SLS MPDR solution.

4 A MUTUAL COUPLING RESISTANT APPROACH

4.1 Literature Review concerning Mutual Coupling Compensation

Over the past decades, vast research has been performed on the topic of mutual coupling in antenna arrays, leading to several techniques for modeling, estimating, and mitigating its effects. Insights on the EM phenomena involved, along with circuit modeling, can be found in [19–27], while practical solutions to counter the mutual coupling effects have been investigated, such as decoupling networks [29, 53–55] and compensating algorithms [36, 56–60]. A few papers have elaborated on mutual coupling compensation techniques in adaptive beamforming to enhance array performance, [17, 28, 36, 57–64], while some have studied robust algorithms to compensate mutual coupling distortion [28, 36, 58]. Recent efforts have used machine learning and optimization as seen in [28, 57, 58]. Finally, we may highlight deep learning models for real-time mutual coupling prediction and mitigation, showing the potential of artificial intelligence (AI) driven approaches in antenna array design and operation [65–67]. These studies emphasize both past and current efforts to handle mutual coupling and highlight the need for continued research to enhance antenna array performance and signal quality.

However, most of the current mutual coupling compensation techniques present in the literature involve array calibration [16, 18, 28, 29]. This means ultimately an estimation of the in-situ or realistic array manifold vector, and, nowadays, usually requires either previous array measurements or 3D full-wave simulations, known both to be extensive and time-consuming works, or, at least, a task to be performed in advance [13, 30, 31]. Some references work with the premise of an unknown mutual coupling matrix (MCM), e.g. [56, 68], however, they usually assume that the mutual coupling matrix has a specific structure to be taken advantage of, which is usually not a real-life scenario, as thoroughly detailed in [13, 69]. Additionally, the calibration performed is usually particular to a specific array design and dimensions and therefore might be susceptible to structural changes.

Therefore, in a practical scenario of an uncalibrated array, the realistic array manifold vector is unknown and the ABF would converge to a distorted beamforming solution, with a significant loss in performance, signal quality, and signal-to-interference plus noise ratio.

4.2 Methodology for Mutual Coupling Evaluation and Mitigation

In this work we estimate the mutual coupling of three different antenna-type ULAs, with the help of full-wave 3D electromagnetic simulation; and propose a solution

to mitigate the signal-impairing effects without previous knowledge of the realistic array manifold. Also, this is done without relying on the assumption that the MCM has a specific structure, e.g., Toeplitz. The main idea is to combine a robust design with a technique that enforces sidelobe suppression while keeping the distortionless constraint, using additional linear constraints to the adaptive filter. Finally, the main contribution is a novel adaptive beamforming solution to mitigate the mutual coupling distortion when the realistic AMV is unknown. A schematic of the methodology used for achieving this objective is displayed in Figure 15. The methodology is explained following the related thesis objectives:

- (i) To estimate the non-isotropic radiation patterns and the mutual coupling on different antenna-type uniform linear arrays and incorporate them into a realistic array manifold vector model.
 - a) The work started with a literature review concerning the state of the art in mutual coupling effects, modeling, and compensation with a focus on adaptive beamforming.
 - b) Among different options, we chose the model from [13] to calculate the realistic array manifold vector.
 - c) Three different antenna-type arrays with the same number of elements have been designed with the help of a 3D full-wave electromagnetic simulation software. The ULA geometry was chosen due to its simplicity.
 - d) The arrays have been simulated to retrieve the scattering matrix and the isolated and embedded radiation patterns.
 - e) The mutual coupling matrix and realistic array manifold vectors have been calculated using the previously retrieved data from each array.
- (ii) To calculate optimum and adaptive beamforming with the realistic array manifold vector and evaluate the effects on the beampattern and SINR for the different arrays.
 - a) The signal model was adapted to include mutual coupling using now the realistic instead of the isotropic array manifold vector.
 - b) MPDR versions to consider mutual coupling were derived with and without knowledge of the realistic AMV.
 - c) The MPDR beampatterns were calculated and the mutual coupling distortion effects were evaluated for the different arrays.
 - d) An adaptive beamformer beampattern was calculated to observe the MC effects.
- (iii) To propose a solution to mitigate the signal-impairing effects for the scenario where the array is not previously calibrated, i.e., without previous knowledge of the realistic array manifold.

- a) Due to the known efficiency of robust solutions to mitigate mutual coupling effects, we have chosen, tested, and implemented the robust solution to adaptive beamformers from [70], mainly due to its simplicity and low computational cost.
- b) Based on the mutual coupling effects observed in the studied beampatterns, we employed the robust solution and our NP-SLS algorithm, separately and combined, to mitigate the observed effects.
- c) We have performed experiments to evaluate the effectiveness of the combined Robust NP-SLS technique in terms of mitigating the mutual coupling effects.

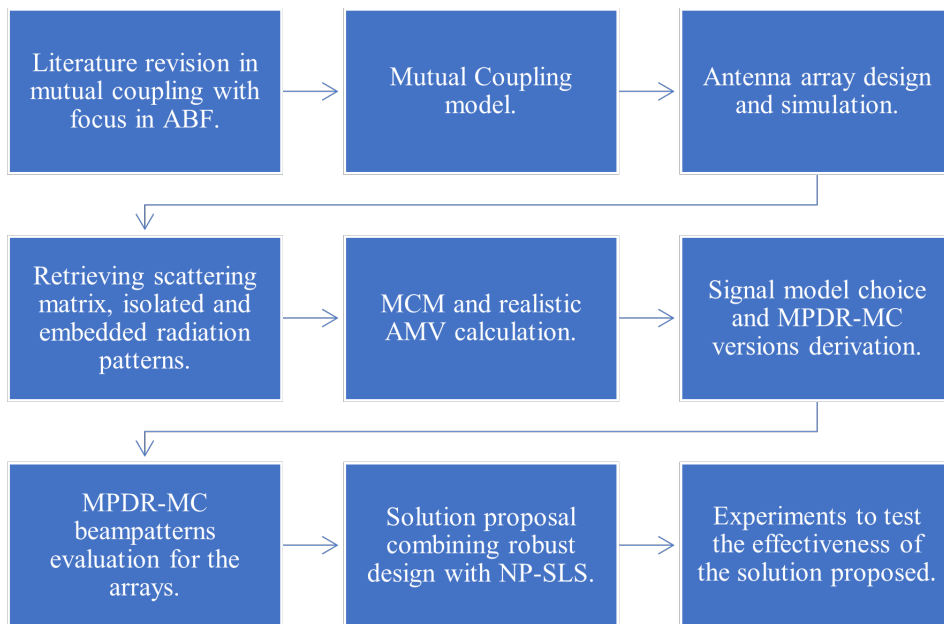


Figure 15 – Methodology used concerning Mutual Coupling evaluation and mitigation.

4.3 Modeling the Mutual Coupling

The mutual coupling effect in an array may be modeled according to different methodologies, as in e.g., [13, 30, 71, 72]. The methodology applied here is the one described in [13]. In this Section lies a description of how the mutual coupling was modeled and how the 3D full-wave EM simulation was employed to that end.

4.3.1 A Realistic Mutual Coupling Model for a ULA

One way to achieve a correct representation of the mutual coupling effect on an antenna array is to consider an appropriate mathematical model of the realistic AMV, also referred to as analytic AMV [13]. The realistic manifold incorporates the effects of mutual

coupling, the physical structure of the antennas, feed point locations, and terminating load.

The following experiment can achieve the realistic AMV [13]: a transmitter is placed at some far-field distance r from the center of the array, in a direction given by azimuth ϕ and elevation θ , transmitting a sinusoidal signal at frequency f . The vector of complex voltages at the outputs of the M antennas constitutes the array manifold vector at a given frequency. The vector is computed by collecting measurements at the antenna feed ports while the transmitter is moved to all possible directions for a given frequency f .

Since we are focused on a ULA, as the example in Figure 2, with its elements placed along the x axis and centered on the origin, the isotropic array manifold model is written as

$$\mathbf{a}(\phi) = \begin{bmatrix} e^{-j\frac{2\pi}{\lambda}x_1 \cos(\phi)} \\ e^{-j\frac{2\pi}{\lambda}x_2 \cos(\phi)} \\ \vdots \\ e^{-j\frac{2\pi}{\lambda}x_M \cos(\phi)} \end{bmatrix}, \quad (4.1)$$

where x_m is the coordinate of the m -th antenna and $\lambda = c/f$ is the wavelength. Therefore, all analyses made in this text are in the $x - y$ plane ($\theta = 90^\circ$) with one direction of interest: ϕ . The phases of the antenna elements are defined with respect to the phase at the origin, i.e., at $x = y = z = 0$.

The isotropic manifold from Equation (4.1) considers neither the mutual coupling between the antennas nor their radiation pattern. However, the isolated array manifold from Equation (4.2) resembles the situation when none of the remaining antennas are present and considers the isolated radiation patterns.

$$\mathbf{a}_{\text{iso}}(\phi) = \text{diag}(\mathbf{g}_{\text{iso}}(\phi))\mathbf{a}(\phi), \quad (4.2)$$

where $\mathbf{g}_{\text{iso}}(\phi) = [g_{\text{iso},1} \ g_{\text{iso},2} \ \cdots \ g_{\text{iso},M}]^T$ is the complex isolated radiation pattern vector of the M antennas in the receiving loaded configuration, while the transmitter is moved to all possible directions, ϕ , for a given frequency f . It is important to highlight that all radiation patterns in this text are far-field radiation patterns represented by the vector \mathbf{g} .

Two of the main frequency-dependent parameters of an antenna are their radiation pattern and input impedance [20, 73]. Mutual coupling results from a change in the near field configuration of the antenna due to the presence of a near object compared to the isolation condition. As a result, new or different equivalent currents are induced on the near objects, and the currents on the antenna change, causing radiation pattern and input impedance to change, resulting in an augmented antenna [20]. Therefore, another radiation pattern of interest is when all the other antennas in the array are present, passive, and their terminals are open-circuited [13], while the terminal of the antenna of interest is loaded. It is referred to as an open-circuit or embedded antenna pattern and is represented

by $\mathbf{g}_{\text{oc}}(\phi) = [g_{\text{oc},1} \ g_{\text{oc},2} \ \cdots \ g_{\text{oc},M}]^T$. The embedded pattern depends on the structure of the complete array and, therefore is significantly different from the isolated pattern. In this context, the open-circuit array manifold is:

$$\mathbf{a}_{\text{oc}}(\phi) = \text{diag}(\mathbf{g}_{\text{oc}}(\phi))\mathbf{a}(\phi). \quad (4.3)$$

4.3.2 The Mutual Coupling Matrix

An effective way to model the mutual coupling between the antennas of an array is the mutual coupling matrix, \mathbf{C} , which multiplies the uncoupled manifold [13]. This can be done either by applying the MCM to the isolated (also called uncoupled) manifold so that the realistic array manifold can be written as [13]:

$$\bar{\mathbf{a}}(\phi) = \mathbf{C} \mathbf{a}_{\text{iso}}(\phi). \quad (4.4)$$

Computing the MCM, however, requires two steps. The first is finding the relation between the complex voltages at the ports of the loaded and the open-circuited array on a far-field receiving situation, which is represented by [21]:

$$\mathbf{v}_{\text{oc}} = (\mathbf{I} + \mathbf{Z}\mathbf{Z}_{\text{L}}^{-1}) \mathbf{v}, \quad (4.5)$$

where \mathbf{v}_{oc} is the vector of the complex voltages in the ports of an array due to the incidence of a plane wave, \mathbf{Z} is the mutual impedance matrix of the array, and \mathbf{Z}_{L} is the diagonal matrix of the loads on the terminals. After proper algebraic manipulation, Equation (4.5) yields:

$$\mathbf{v} = \mathbf{Z}_{\text{L}}(\mathbf{Z} + \mathbf{Z}_{\text{L}})^{-1} \mathbf{v}_{\text{oc}}. \quad (4.6)$$

Since the array manifold vector is equivalent to the complex voltages on the array antenna terminals, one can write:

$$\bar{\mathbf{a}}(\phi) = \underbrace{\mathbf{Z}_{\text{L}}(\mathbf{Z} + \mathbf{Z}_{\text{L}})^{-1}}_{\mathbf{C}_{\text{oc}}} \mathbf{a}_{\text{oc}}(\phi), \quad (4.7)$$

where

$$\mathbf{C}_{\text{oc}} = \mathbf{Z}_{\text{L}}(\mathbf{Z} + \mathbf{Z}_{\text{L}})^{-1}. \quad (4.8)$$

The second step is retrieving the relation between the open circuit and isolated manifolds, which can be given by [13]:

$$\mathbf{a}_{\text{oc}}(\phi) = \mathbf{G}_{\text{iso}}(\phi)\mathbf{a}_{\text{iso}}(\phi), \quad (4.9)$$

where

$$\mathbf{G}_{\text{iso}}(\phi) = \text{diag} \left\{ \frac{a_{\text{oc},1}(\phi)}{a_{\text{iso},1}(\phi)}, \dots, \frac{a_{\text{oc},M}(\phi)}{a_{\text{iso},M}(\phi)} \right\}. \quad (4.10)$$

Finally, the realistic array manifold vector can be computed as:

$$\bar{\mathbf{a}}(\phi) = \underbrace{\mathbf{Z}_L (\mathbf{Z} + \mathbf{Z}_L)^{-1} \mathbf{G}_{\text{iso}}(\phi)}_{\mathbf{C}_{\text{iso}}(\phi)} \mathbf{a}_{\text{iso}}(\phi), \quad (4.11)$$

and the MCM can be computed by [13]:

$$\mathbf{C}(\phi) = \mathbf{C}_{\text{iso}}(\phi) = \mathbf{Z}_L (\mathbf{Z} + \mathbf{Z}_L)^{-1} \mathbf{G}_{\text{iso}}(\phi). \quad (4.12)$$

One can notice that the proper MCM model, $\mathbf{C}(\phi)$, is direction dependent, unlike the relation between the realistic and open-circuit manifolds, \mathbf{C}_{oc} , which is direction independent [13]. A final representation of the realistic array manifold vector, equivalent to Equation (4.11), can be given in terms of the isotropic array manifold as:

$$\bar{\mathbf{a}}(\phi) = \underbrace{\mathbf{Z}_L (\mathbf{Z} + \mathbf{Z}_L)^{-1} \mathbf{G}_{\text{iso}}(\phi)}_{\mathbf{C}(\phi)} \text{diag}(\mathbf{g}_{\text{iso,t}}(\phi)) \mathbf{a}(\phi), \quad (4.13)$$

where $\mathbf{g}_{\text{iso,t}}(\phi)$ is the complex isolated radiation pattern in a general term, not necessarily related to the far-field wave receiving experiment.

In summary, according to the methodology used herein, in order to determine the realistic or in-situ array manifold vector one must first gain knowledge of vectors $\mathbf{a}_{\text{iso}}(\phi)$, $\mathbf{a}_{\text{oc}}(\phi)$, $\mathbf{g}_{\text{iso,t}}(\phi)$, and matrix \mathbf{Z} . In other words, calculating $\bar{\mathbf{a}}(\phi)$ involves calculating the electric and magnetic fields generated by an antenna array [13], using electromagnetic theory based on the solution of Maxwell's equations, as in the methods described in, e.g., [73–78]. However, computing this AMV usually does not yield closed-form expressions [13], which can be often overcome by using numerical methods also known as numerical electromagnetic codes (NEC) [79–81]. In the next Section we describe how the realistic AMV was calculated using NEC.

As previously stated, the MCM usually has no fixed specific structure and therefore is not diagonal. In parallel with this master thesis, we have developed a method to derive an equivalent diagonal MCM to $\mathbf{C}(\phi)$, $\mathbf{C}_D(\phi)$ [82]. Its essential contribution is the potential of the proposed equivalent diagonal MCM to simplify matrix-vector multiplication and reduce memory requirements. Since it is not the focus of this master thesis it is not detailed herein.

4.3.3 Calculation of Array Response using 3D Electromagnetic Simulation

To calculate the in-situ AMV, this work has used numeric methods. The NEC used herein to perform the 3D design and full-wave simulations of the arrays was the ANSYS High-Frequency Structure Simulation Software (HFSS[®]) [83].

First, as part of the receiving wave experiment proposed, HFSS[®] was used to provide the results of the complex voltages on each array port $(1, 2, \dots, M)$ when excited

by a far-field incident plane wave excitation for three distinct arrays. This was done in the isolated and open-circuit conditions, computed as the array manifolds $\mathbf{a}_{\text{iso}}(\phi)$ and $\mathbf{a}_{\text{oc}}(\phi)$, for each of the evaluated N receiving angles ($0^\circ, 1^\circ, \dots, 180^\circ$). The resulting matrices \mathbf{A}_{iso} and \mathbf{A}_{oc} have dimension $M \times N$. Tables 1 and 2 provide the data format used for the computation of the complex voltage vectors $\mathbf{a}_{\text{iso}}(\phi)$ and $\mathbf{a}_{\text{oc}}(\phi)$ for each of the M ports. Figures 16 and 17 show an example of model configurations for calculation of $\mathbf{a}_{\text{iso}}(\phi)$ and $\mathbf{a}_{\text{oc}}(\phi)$ for a dipole array with $M = 4$ antenna elements. For \mathbf{A}_{iso} calculation the port of interest is active, $Z = Z_L$, while the remaining ports and antennas are not present as seen in Table 1 and in Figure 16. For \mathbf{A}_{oc} calculation the port of interest is active, $Z = Z_L$, while the remaining ports are configured with an impedance much higher than the matched load $Z \gg Z_L$, here used $Z = 10^6 \Omega$, and remaining antennas present in the model ("augmented antenna"), as seen in Table 2 and in Figure 17. For each array of the three different arrays, \mathbf{A}_{iso} and \mathbf{A}_{oc} calculations demanded performing M 3D electromagnetic simulations each, each simulation having N steps for each of the impinging signal angles.

Table 1 – Data format of the computed simulated complex voltages under isolated condition

\mathbf{A}_{iso}	ϕ_1	ϕ_2	\dots	ϕ_N
$\mathbf{a}_{\text{iso},1}(\phi)$ Port 1: active ($Z_1 = Z_L$) Remaining ports: not present	$a_{\text{iso},1}(\phi_1)$	$a_{\text{iso},1}(\phi_2)$	\dots	$a_{\text{iso},1}(\phi_N)$
$\mathbf{a}_{\text{iso},2}(\phi)$ Port 2: active ($Z_2 = Z_L$) Remaining ports: not present	$a_{\text{iso},2}(\phi_1)$	$a_{\text{iso},2}(\phi_2)$	\dots	$a_{\text{iso},2}(\phi_N)$
\vdots	\vdots	\vdots	\vdots	\vdots
$\mathbf{a}_{\text{iso},M}(\phi)$ Port M : active ($Z_M = Z_L$) Remaining ports: not present	$a_{\text{iso},M}(\phi_1)$	$a_{\text{iso},M}(\phi_2)$	\dots	$a_{\text{iso},M}(\phi_N)$

Second, independent from the receiving wave experiment, the designed arrays were simulated in HFSS[®] on a transmitting condition in order to compute the element's complex isolated radiation pattern, $\mathbf{g}_{\text{iso},t}(\phi)$, and the array's mutual impedance matrix \mathbf{Z} on a loaded matched configuration. One extra simulation was required where no exciting wave was configured. The resulting matrix $\mathbf{G}_{\text{iso},t}$ has dimension $M \times N$, while \mathbf{Z} is $M \times M$. Additionally, the load impedance matrix was defined as $\mathbf{Z}_L = Z_L \mathbf{I}$.

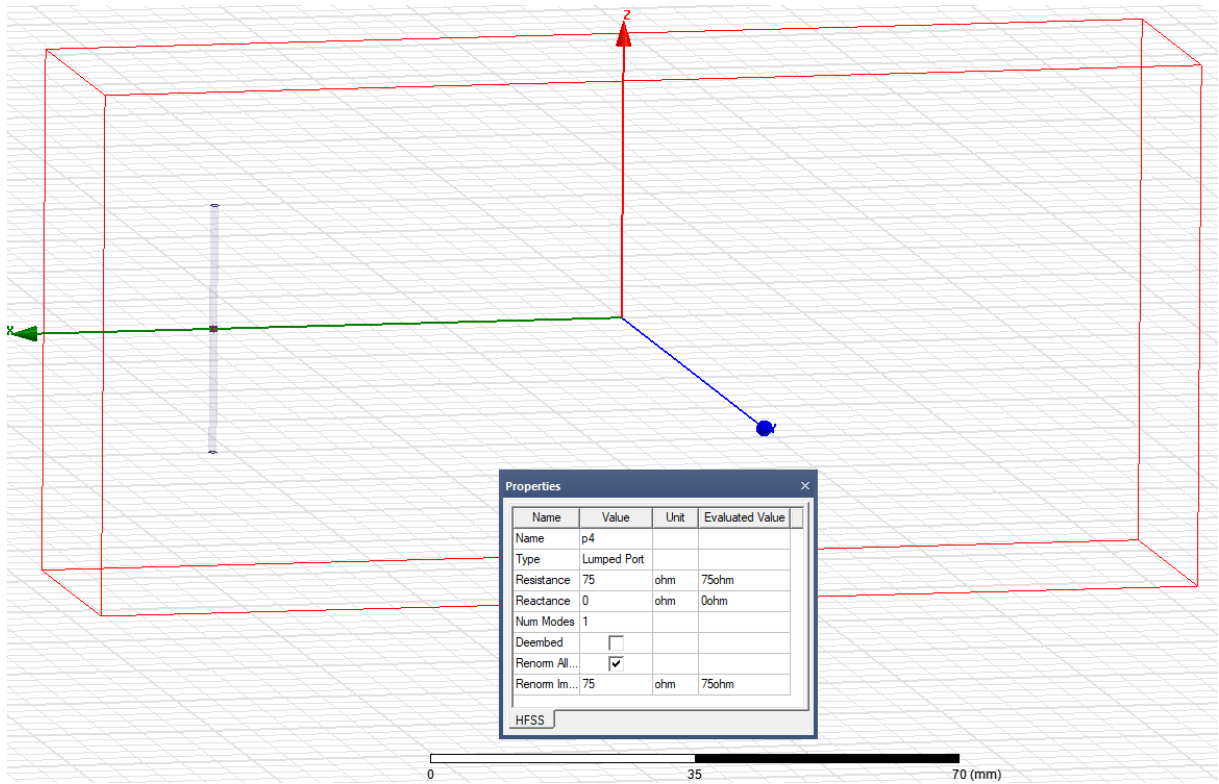


Figure 16 – Example of model configuration for calculation of $\mathbf{a}_{\text{iso},1}(\phi)$ in a dipole array with $M = 4$ antenna elements.

Table 2 – Data format of the computed simulated complex voltages under open-circuit condition

\mathbf{A}_{oc}	ϕ_1	ϕ_2	...	ϕ_N
$\mathbf{a}_{\text{oc},1}(\phi)$ Port 1: active ($Z_1 = Z_L$) Remaining ports: $Z = 10^6\Omega$	$a_{\text{oc},1}(\phi_1)$	$a_{\text{oc},1}(\phi_2)$...	$a_{\text{oc},1}(\phi_N)$
$\mathbf{a}_{\text{oc},2}(\phi)$ Port 2: active ($Z_2 = Z_L$) Remaining ports: $Z = 10^6\Omega$	$a_{\text{oc},2}(\phi_1)$	$a_{\text{oc},2}(\phi_2)$...	$a_{\text{oc},2}(\phi_N)$
\vdots	\vdots	\vdots	\vdots	\vdots
$\mathbf{a}_{\text{oc},M}(\phi)$ Port M : active ($Z_M = Z_L$) Remaining ports: $Z = 10^6\Omega$	$a_{\text{oc},M}(\phi_1)$	$a_{\text{oc},M}(\phi_2)$...	$a_{\text{oc},M}(\phi_N)$

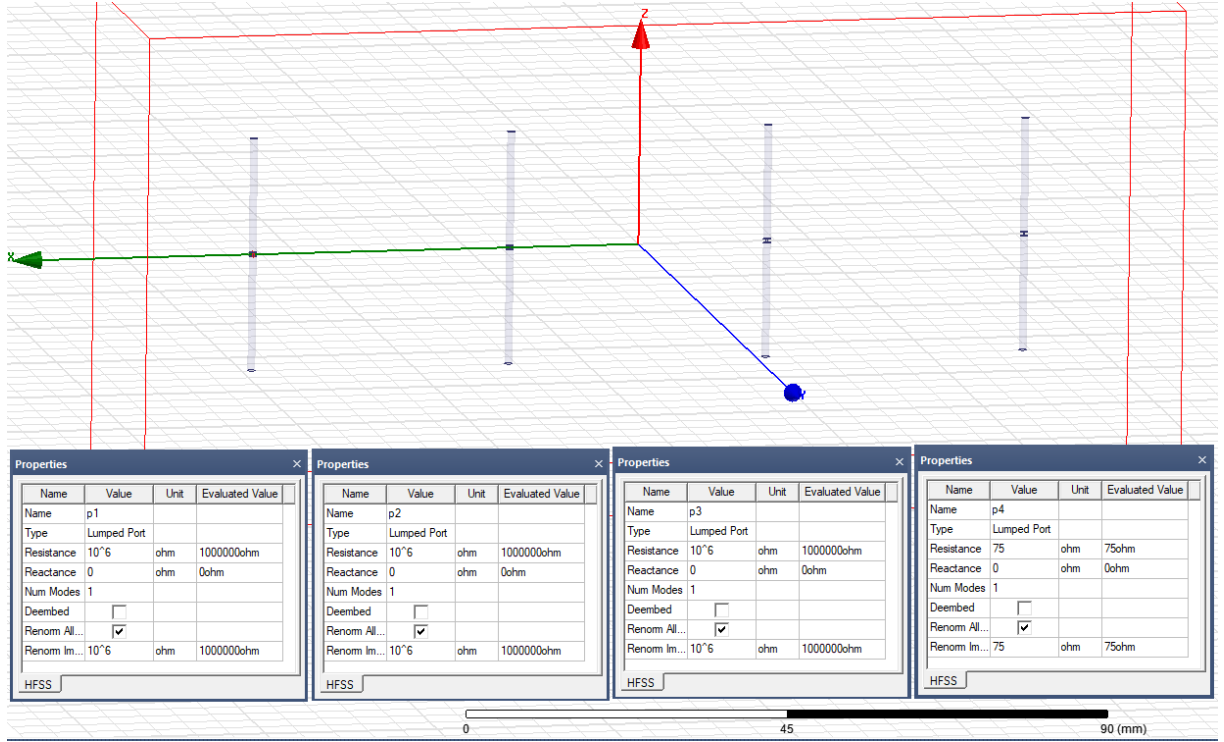


Figure 17 – Example of model configuration for calculation of $\mathbf{a}_{oc,4}(\phi)$ in a dipole array with $M = 4$ antenna elements.

4.3.4 Signal Model with Mutual Coupling

In the case of mutual coupling, the isotropic array manifold is replaced with the realistic array manifold vector and the signal model may be represented as:

$$\bar{\mathbf{x}}(k) = \begin{bmatrix} \bar{x}_1(k) \\ \vdots \\ \bar{x}_m(k) \\ \vdots \\ \bar{x}_M(k) \end{bmatrix} = s(k) \underbrace{\begin{bmatrix} \alpha_1(\phi) e^{-j(\Omega_o \Delta t_1 + \beta_1(\phi))} \\ \vdots \\ \alpha_m(\phi) e^{-j(\Omega_o \Delta t_m + \beta_m(\phi))} \\ \vdots \\ \alpha_M(\phi) e^{-j(\Omega_o \Delta t_M + \beta_M(\phi))} \end{bmatrix}}_{\bar{\mathbf{a}}(\phi)} + \underbrace{\begin{bmatrix} \bar{n}_1(k) \\ \vdots \\ \bar{n}_m(k) \\ \vdots \\ \bar{n}_M(k) \end{bmatrix}}_{\bar{\mathbf{n}}(k)}, \quad (4.14)$$

where $\alpha_m(\phi)$ and $\beta_m(\phi)$ are the gains and the phase delays due to the mutual coupling matrix $\mathbf{C}(\phi)$ and the isolated radiation pattern $\mathbf{g}_{iso,t}(\phi)$ multiplication on the isotropic array manifold $\mathbf{a}(\phi)$ as in Equation (4.13). Here, $\beta_m(\phi)$ is not the propagation constant β defined in the Section 2.3. Vector $\bar{\mathbf{n}}(k)$ is white Gaussian noise in the case of having mutual coupling. Therefore, the realistic AMV depends not only on the direction of arrival ϕ and on the array's geometry, but also on the additional gains and phase delays caused by the mutual coupling and by the isolated radiation pattern. Consider now the case of D different sources, $D \leq M$, 1 SOI (ϕ_1) and $D - 1$ jammers (ϕ_2 to ϕ_D), so that the signal

model adopted herein is:

$$\begin{aligned}
\bar{\mathbf{x}}(k) &= s_1(k)\bar{\mathbf{a}}(\phi_1) + \cdots + s_D(k)\bar{\mathbf{a}}(\phi_D) + \bar{\mathbf{n}}(k) \\
&= \underbrace{\begin{bmatrix} \bar{\mathbf{a}}(\phi_1) & \cdots & \bar{\mathbf{a}}(\phi_D) \end{bmatrix}}_{\bar{\mathbf{A}} \text{ (steering matrix)}} \underbrace{\begin{bmatrix} s_1(k) \\ \vdots \\ s_D(k) \end{bmatrix}}_{\mathbf{s}(k)} + \bar{\mathbf{n}}(k) \\
&= \bar{\mathbf{A}}\mathbf{s}(k) + \bar{\mathbf{n}}(k).
\end{aligned} \tag{4.15}$$

4.4 Antenna Array Scenarios

Figures 18, 19, and 20 display the HFSS[®] antenna array designs used herein: a $\lambda/2$ dipole, a bowtie, and a microstrip antenna array, all with 8 elements. All arrays have been designed in HFSS[®] to operate at center frequency $f_o = 4$ GHz and with physical separation between elements $d = \frac{\lambda}{2}$. The dipole antenna dimensions are: arm radius $r = 0.562$ mm, arm length along z axis $l = 16.594$ mm, and port gap $g = 0.562$ mm, having a total length of 33.75 mm. The bowtie antenna dimensions are: arm width along x axis $wd = 11.9$ mm, arm length along z axis $l = 11.335$ mm, arm thickness $t = 0.5$ mm, angle between the two arms in the z axis is 124° , and port gap $g = 1.23$ mm, having a total length of 23.9 mm. The rectangular microstrip antenna dimensions are: patch width along x axis $wd = 30$ mm, patch length along z axis $l = 24$ mm, feed width $fw = 1.1$ mm, substrate thickness $h = 1.575$ mm, and cladding $cl = 0.035$ mm. The substrate arbitrarily chosen was the Rogers RT/duroid[®] 5880 Laminate [84] with dissipation factor $\tan\delta = 0.0009$ and the previously referred thickness and cladding.

The gain radiation patterns of the three arrays in the $x - y$ plane at $\theta = 90^\circ$ can be seen in Figures 21, 22, 23. The dipole, bowtie, and microstrip radiation patterns are directive at the $x - y$ plane, with the microstrip array possessing low gain when $\phi = -90^\circ$, as expected due to the ground plane in that direction. The maximum gain on the $x - y$ plane at $\theta = 90^\circ$ of the dipole array is 12.38 dBi, of the bowtie array is 11.72 dBi, and of the microstrip array is 15.46 dBi. $\mathbf{Z}_L = 75\mathbf{I} \Omega$ for the dipole array and $\mathbf{Z}_L = 50\mathbf{I} \Omega$ for the bowtie and microstrip arrays.

Tables 3, 4, and 5 display the scattering matrix of the dipole, bowtie, and microstrip antenna arrays obtained through HFSS[®] simulation, calculated in dB as in Equations (2.25) and (2.27). As seen in Tables 3, 4, and 5, the S_{ii} results show efficient radiation with return loss over 10 dB at the center frequency for all arrays at 4 GHz. Also, in a general way, the S_{ij} results, which can also be seen as inter-element coupling, of the microstrip array are higher than those of the dipole array and both are much higher than the ones from the bowtie array. This insight will prove useful when calculating the mutual coupling matrices in Section 4.9.

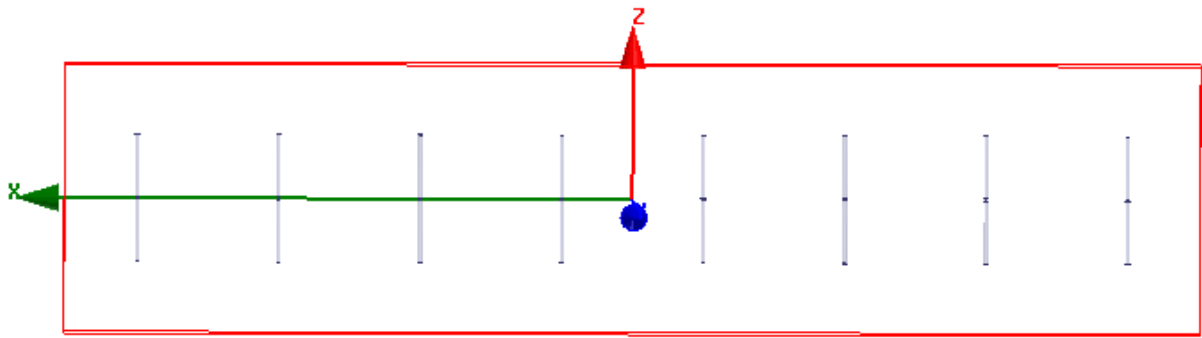


Figure 18 – Dipole array design model as used in the HFSS[®] software.

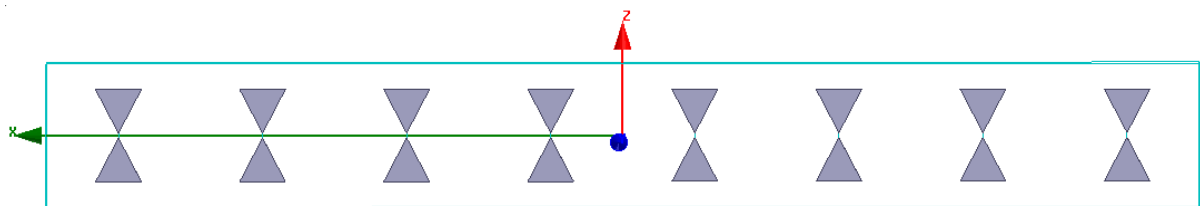


Figure 19 – Bowtie array design model as used in the HFSS[®] software.

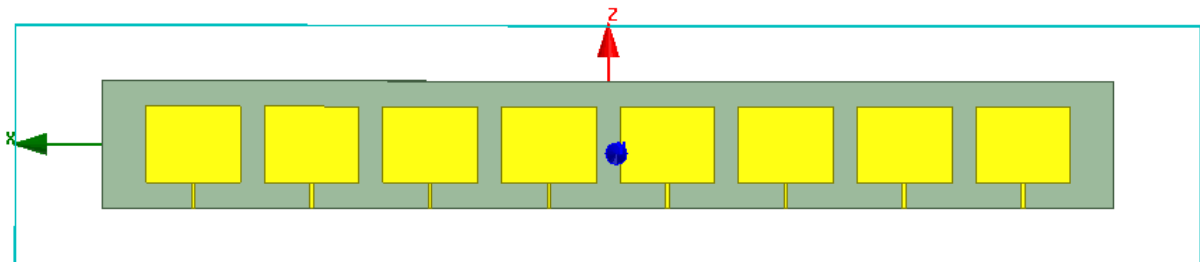


Figure 20 – Microstrip array design model as used in the HFSS[®] software.

Table 3 – Dipole Array Scattering Matrix (in dB)

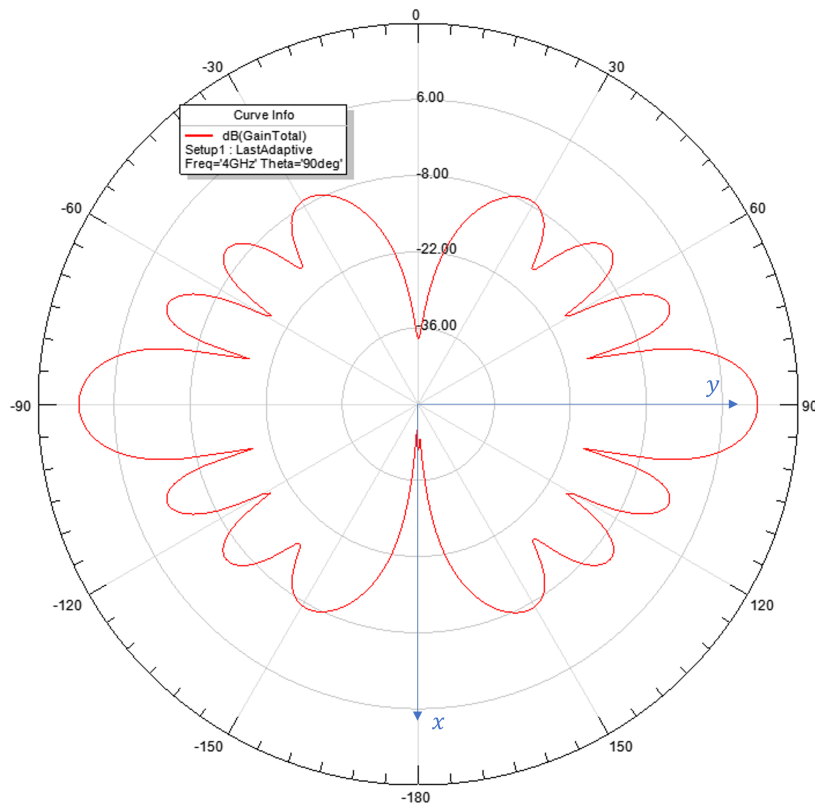
-16.99	-15.01	-15.03	-22.10	-21.74	-25.67	-26.11	-28.56
-15.01	-17.40	-21.84	-14.98	-26.02	-28.50	-21.77	-25.42
-15.03	-21.84	-17.74	-26.14	-14.91	-21.14	-28.89	-30.66
-22.10	-14.98	-26.14	-18.06	-28.74	-30.37	-14.75	-21.19
-21.74	-26.02	-14.91	-28.74	-17.91	-14.28	-31.03	-32.45
-25.67	-28.50	-21.14	-30.37	-14.28	-20.36	-32.38	-34.08
-26.11	-21.77	-28.89	-14.75	-31.03	-32.38	-18.29	-14.33
-28.56	-25.42	-30.66	-21.19	-32.45	-34.08	-14.33	-20.12

Table 4 – Bowtie Array Scattering Matrix (in dB)

-29.15	-16.86	-37.11	-56.84	-76.65	-96.58	-116.44	-136.25
-16.86	-26.04	-16.88	-37.11	-56.90	-76.83	-96.69	-116.51
-37.11	-16.88	-26.11	-16.88	-37.18	-57.10	-76.96	-96.78
-56.84	-37.11	-16.88	-26.58	-16.89	-37.33	-57.19	-77.00
-76.65	-56.90	-37.18	-16.89	-27.93	-16.83	-37.21	-57.02
-96.58	-76.83	-57.10	-37.33	-16.83	-27.25	-16.87	-37.20
-116.44	-96.69	-76.96	-57.19	-37.21	-16.87	-27.41	-16.86
-136.25	-116.51	-96.78	-77.00	-57.02	-37.20	-16.86	-28.89

Table 5 – Microstrip Array Scattering Matrix (in dB)

-18.06	-11.92	-21.61	-29.95	-37.18	-43.81	-50.24	-56.41
-11.92	-20.33	-11.80	-21.65	-30.10	-37.46	-44.31	-50.50
-21.61	-11.80	-19.37	-11.73	-21.45	-29.85	-37.39	-44.04
-29.95	-21.65	-11.73	-19.81	-11.75	-21.46	-30.02	-37.44
-37.18	-30.10	-21.45	-11.75	-19.75	-11.69	-21.49	-30.09
-43.81	-37.46	-29.85	-21.46	-11.69	-19.36	-11.72	-21.76
-50.24	-44.31	-37.39	-30.02	-21.49	-11.72	-20.10	-12.02
-56.41	-50.50	-44.04	-37.44	-30.09	-21.76	-12.02	-18.97

Figure 21 – Dipole array gain radiation pattern result (in dB) in HFSS[®] software.

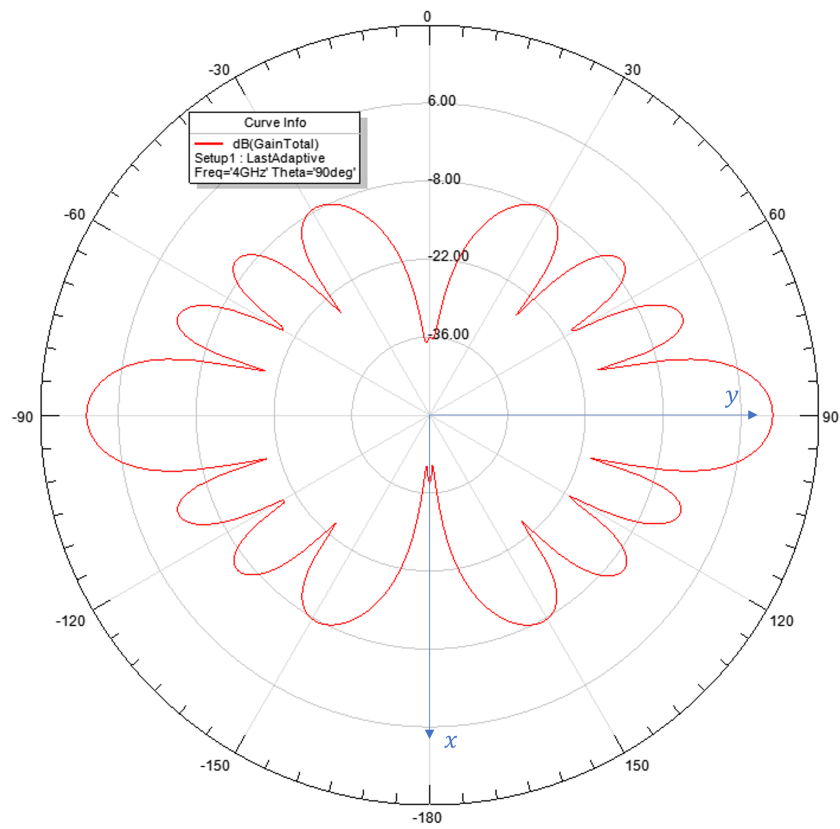


Figure 22 – Bowtie array gain radiation pattern result (in dB) in HFSS[®] software.

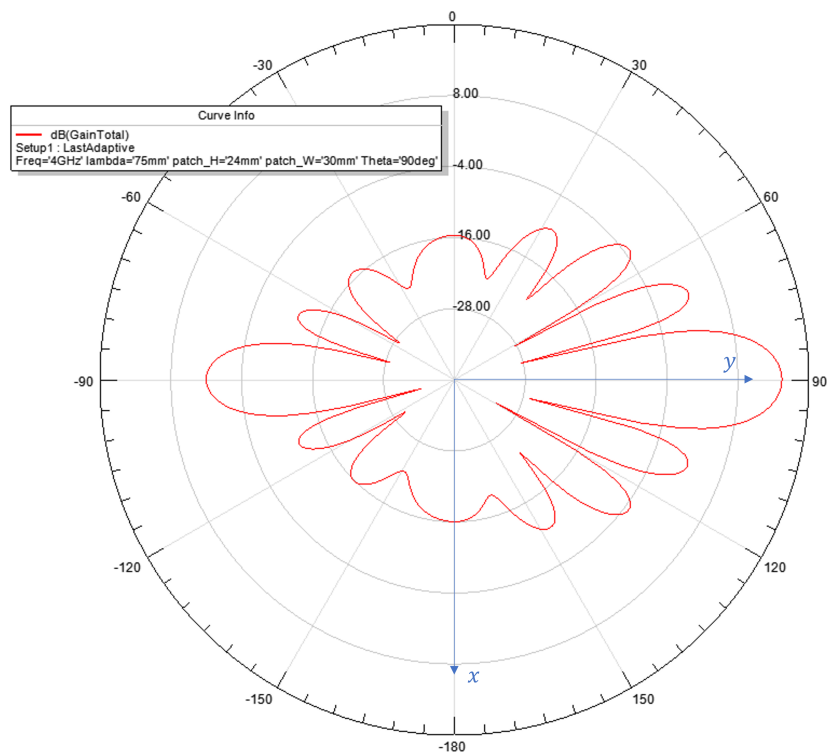


Figure 23 – Microstrip array gain radiation pattern result (in dB) in HFSS[®] software.

4.5 Optimum Beamforming with Mutual Coupling

4.5.1 MPDR Beamforming with Mutual Coupling

For the MPDR beamforming considering mutual coupling between the antenna elements, the minimization at hand may be written as minimizing the energy at the output $\mathbb{E}[|y(k)|^2] = \mathbf{w}^H \bar{\mathbf{R}}_x \mathbf{w}$, where $\bar{\mathbf{R}}_x = \mathbb{E}[\bar{\mathbf{x}}(k)\bar{\mathbf{x}}^H(k)]$, and $\bar{\mathbf{x}}(k) = s_1(k)\bar{\mathbf{a}}(\phi_1) + \dots + s_D(k)\bar{\mathbf{a}}(\phi_D) + \bar{\mathbf{n}}(k)$. $\bar{\mathbf{R}}_x$ is the covariance matrix of the input signal with mutual coupling, subject to $\mathbf{w}^H \bar{\mathbf{a}}(\phi_1) = 1$ which is the distortionless criteria in the mutual coupling scenario. It yields:

$$\bar{\mathbf{w}}_{\text{MPDR}} = \frac{\bar{\mathbf{R}}_x^{-1} \bar{\mathbf{a}}(\phi_1)}{\bar{\mathbf{a}}^H(\phi_1) \bar{\mathbf{R}}_x^{-1} \bar{\mathbf{a}}(\phi_1)}. \quad (4.16)$$

4.5.2 MPDR Beamforming with Mutual Coupling and without knowledge of the realistic array manifold

The optimum beamforming solution from Equation (4.16) implies in a previous knowledge of the realistic array manifold $\bar{\mathbf{a}}(\phi_1)$. This, in practical terms, requires a previous calibration of the array or, ultimately, its measurement or a 3D EM full wave simulation by a NEC.

Alternatively, we can define an optimum beamforming solution where the realistic array manifold $\bar{\mathbf{a}}(\phi_1)$ is unknown, closer to a practical scenario of an uncalibrated array when receiving a signal previously distorted by mutual coupling effects. Following the mutual coupling MPDR derivation, however subject to the distortionless criteria with $\mathbf{a}(\phi_1)$ instead of $\bar{\mathbf{a}}(\phi_1)$, we obtain:

$$\mathbf{w}_{\text{MPDR-MC}} = \frac{\bar{\mathbf{R}}_x^{-1} \mathbf{a}(\phi_1)}{\mathbf{a}^H(\phi_1) \bar{\mathbf{R}}_x^{-1} \mathbf{a}(\phi_1)}. \quad (4.17)$$

4.5.3 Mutual Coupling Effects and the Convergence of an ABF in Case of Mutual Coupling

Figure 24 shows the normalized BP result of four MPDR versions concerning mutual coupling for different arrays. The following simulation results, along with the ones in Section 4.9, concern three stationary signals (one SOI at 110° and two jammers, J1 and J2, at 55° and 135° , respectively) generated and processed following the signal model from Equations (2.3) and (4.14) (without and with mutual coupling), the receiving architecture from Figure 1, and the realistic array manifold vector calculated based on the simulated data from the arrays.

We observe in the first quadrant of Figure 24 the BP without MC is the same for all arrays: the coefficient vector \mathbf{w}_{MPDR} is computed with $\mathbf{a}(\phi_{\text{SOI}})$ and \mathbf{R}_x as in

Equation (2.6), and not plotted in the mutual coupling environment (MCE) such that $BP(\phi) = \mathbf{w}_{\text{MPDR}}^H(\phi)\mathbf{a}(\phi)$.

In the second, third, and fourth quadrants of Figure 24 are the MPDR BPs for the dipole, bowtie, and microstrip arrays respectively. The first curve (in black) is the \mathbf{w}_{MPDR} computed with $\mathbf{a}(\phi_{\text{SOI}})$ and $\mathbf{R}_x = E[\mathbf{x}(k)\mathbf{x}^H(k)]$, i.e., is the version without MC from Equation (2.6) plot in the MCE ($BP(\phi) = \mathbf{w}_{\text{MPDR}}^H(\phi)\bar{\mathbf{a}}(\phi)$). The second curve (in blue) is the $\bar{\mathbf{w}}_{\text{MPDR}}$ computed with $\bar{\mathbf{a}}(\phi_{\text{SOI}})$ and $\bar{\mathbf{R}}_x = E[\bar{\mathbf{x}}(k)\bar{\mathbf{x}}^H(k)]$, i.e., the version with mutual coupling where the realistic AMV is known, as in Equation (4.16), also plotted in the MCE. The third curve (in red) is the $\bar{\mathbf{w}}_{\text{MPDR-MC}}$ computed with $\mathbf{a}(\phi_{\text{SOI}})$ and $\bar{\mathbf{R}}_x = E[\bar{\mathbf{x}}(k)\bar{\mathbf{x}}^H(k)]$, MPDR version without knowledge of the realistic AMV as in Equation (4.17), also plot in the MCE. We assumed $\bar{\mathbf{R}}_x$ known in practical situations since we have the realistic snapshots $\bar{\mathbf{x}}(k)$ and, from them, we estimate $\bar{\mathbf{R}}_x$.

As seen in Figure 24, for the three arrays, the BP of the $\bar{\mathbf{w}}_{\text{MPDR}}$ is quite close to

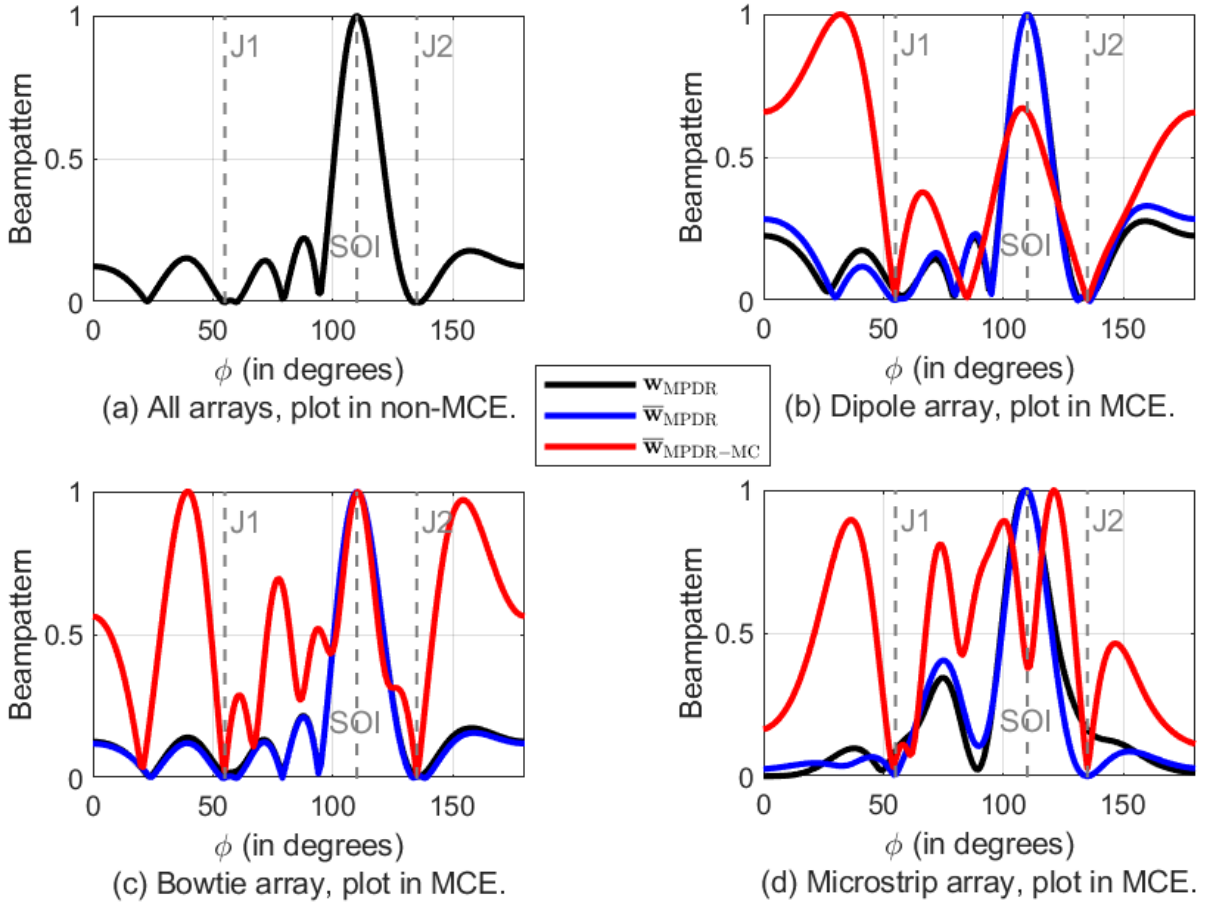


Figure 24 – MPDR beampattern for a generic isotropic array in a non-mutual coupling environment (top left). Beampatterns for the studied dipole, bowtie, and microstrip arrays with mutual coupling.

the one from \mathbf{w}_{MPDR} . This means that when the realistic AMV is known, MC BP tends to the BP without MC, which may be seen as equivalent to the MC compensation or the array calibration. In other words, the closer these coefficients are, the more efficient the

mutual coupling compensation process, e.g., the method used in Section 4.3, based on [13].

The BP from the $\bar{\mathbf{w}}_{\text{MPDR-MC}}$, however, presents significant distortions when compared with the BP from \mathbf{w}_{MPDR} for all the arrays simulated. The distortions seem more important first on the microstrip, second on the dipole, and least on the bowtie array BPs, which is coherent with the inter-element coupling degree insight indicated by the scattering matrices S_{ij} results from Section 4.4 in Tables 3, 4, and 5. This means that the array with the highest MC distortion is the microstrip, followed by the dipole, and least the bowtie. The effects are mainly highly enhanced sidelobes, significant misalignment of the main lobe, and small nulling capability loss, similar to the effects reported in [16], [34], [85]. Therefore, when comparing the BP results from $\bar{\mathbf{w}}_{\text{MPDR-MC}}$ with the ones from $\bar{\mathbf{w}}_{\text{MPDR}}$, we can infer that the array processor that does not hold knowledge of the realistic AMV is directly impacted by distortions due to the mutual coupling phenomena, as seen in the three evaluated arrays.

Most importantly, as we shall see in Section 4.9, the adaptive beamformer solution with mutual coupling in the input signal, $\bar{\mathbf{x}}(k)$, converges to the $\bar{\mathbf{w}}_{\text{MPDR-MC}}$, while the ABF without mutual coupling would converge to the \mathbf{w}_{MPDR} solution. This is considered an important result since it establishes that the MPDR-MC from Equation (4.17) is the optimum beamforming coefficient vector for computing the mutual coupling when no compensation or calibration has been done, i.e., when the realistic AMV is unknown to the beamformer.

4.6 Simplified Version of Mutual Coupling Model

As an abstraction, we could verify the results of a simplified mutual coupling model, sometimes also referred to in the literature as the MCM, where the MCM is direction-independent $\mathbf{C} = \mathbf{C}_{\text{oc}}$. This would change the Equation (4.13) into:

$$\bar{\mathbf{a}}(\phi) = \underbrace{\mathbf{Z}_L (\mathbf{Z} + \mathbf{Z}_L)^{-1}}_{\mathbf{C}} \text{diag}(\mathbf{g}_{\text{iso,t}}(\phi)) \mathbf{a}(\phi). \quad (4.18)$$

In Figure 25 we can see the mutual coupling effects for this simplified mutual coupling model. The mutual coupling effects when we consider the simplified direction independent model diverge considerably from the original results with the complete model. A general analysis of the 3 arrays shows that the simplified model effect may be less severe to the main lobe distortion while having a not-so-different impact on the side lobes. This abstraction provides insight into the importance of considering the MCM variation with the incoming direction of the impinging signals in the array. The results from Figure 25 are not considered further in this text, since they are meant only as an abstraction, as Equation (4.13) is the model used in this thesis.

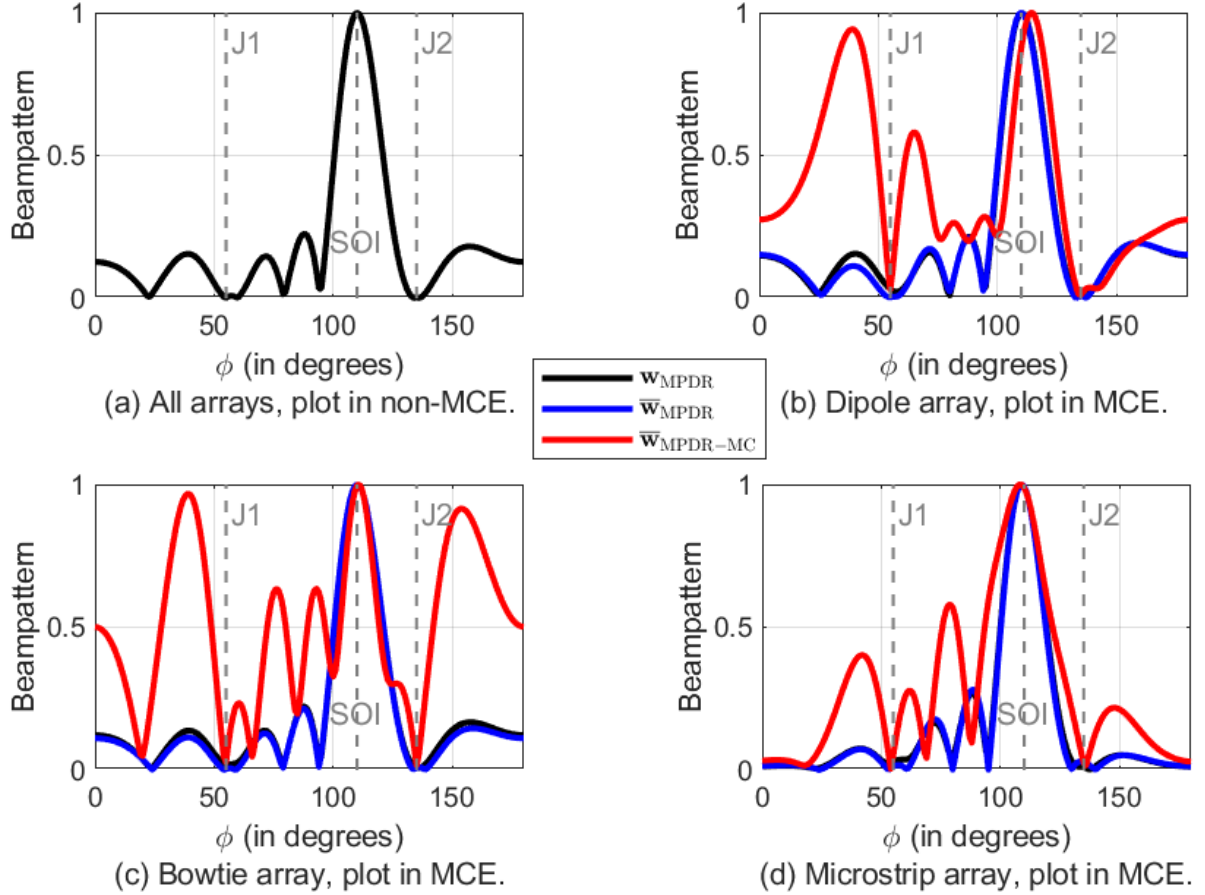


Figure 25 – MPDR beampattern for a generic isotropic array in a non-mutual coupling environment (top left). Beampatterns for the studied dipole, bowtie, and microstrip arrays with mutual coupling. A simplified MC model was used instead of the complete one.

4.7 The Proposed Scheme

This work proposes a solution to mitigate the main signal distortion effects encountered in this study due to the mutual coupling on antenna arrays [86]. Since one of the most present effects is the presence of significant sidelobes, our sidelobe suppression technique, NP-SLS, was directly useful. Besides that, the robust beamforming designs are known for their efficiency against mismatch or errors in the array manifold vector, [70, 87–89].

Therefore, with the purpose of achieving a combined effort, our proposed scheme essentially combines a robust adaptive beamforming design with our sidelobe suppression technique. It uses only the snapshot information available and does not rely on the MCM having a specific structure, e.g., Toeplitz, which is usually not the case [13, 69].

4.7.1 Robust Adaptive Beamformer

For the robust version of the adaptive beamformer, among vast possibilities, the robust technique employed herein was the classic one from [70], due to its simplicity and

effectiveness. Further work may replace it with other robust strategies.

Fundamentally, the employed robust approach aims to ensure that the beamformer is robust and, thus: not highly sensitive to small amplitude, phase, or position errors. To do so, it tries to improve array gain against spatially white noise, G_w , as in [70]:

$$\text{Max}_{\mathbf{w}} \frac{|\mathbf{w}^H \mathbf{a}|^2}{\mathbf{w}^H \mathbf{w}} = G_w = \delta^2 \leq M, \quad (4.19)$$

where δ is the constraining value that must be chosen less than or equal to the maximum possible white noise gain M for self-consistency [70]. This is to be done while also minimizing the total output power, $\text{Min}_{\mathbf{w}} \mathbf{w}^H \mathbf{R}_x \mathbf{w}$, subject to $\mathbf{C}^H \mathbf{w} = \mathbf{f}$, which yields $\mathbf{w} = \mathbf{R}_x^{-1} \mathbf{C} (\mathbf{C}^H \mathbf{R}_x^{-1} \mathbf{C})^{-1} \mathbf{f}$. The weight vector may be decomposed into its orthogonal components $\mathbf{w} = \mathbf{f}_c + \mathbf{v}$, where $\mathbf{f}_c = \mathbf{P}_c \mathbf{w} = \mathbf{C} (\mathbf{C}^H \mathbf{C})^{-1} \mathbf{C}^H \mathbf{w} = \mathbf{C} (\mathbf{C}^H \mathbf{C})^{-1} \mathbf{f}$ is the projection of \mathbf{w} into the range of \mathbf{C} ; and $\mathbf{v} = (\mathbf{I} - \mathbf{P}_c) \mathbf{w} = \mathbf{P} \mathbf{w} = (\mathbf{I} - \mathbf{C} (\mathbf{C}^H \mathbf{C})^{-1} \mathbf{C}^H) \mathbf{w}$ is the projection of \mathbf{w} into the null space of \mathbf{C} . Writing G_w in terms of the orthogonal components yields [70]:

$$G_w = \frac{1}{\mathbf{f}_c^H \mathbf{f}_c + \mathbf{v}^H \mathbf{v}} \geq \delta^2, \quad (4.20)$$

resulting in:

$$\mathbf{v}^H \mathbf{v} \leq \delta^{-2} - \mathbf{f}^H [\mathbf{C}^H \mathbf{C}]^{-1} \mathbf{f} = b^2, \quad (4.21)$$

or finally:

$$b = \sqrt{\frac{1}{\delta^2} - \mathbf{f}^H [\mathbf{C}^H \mathbf{C}]^{-1} \mathbf{f}} = \sqrt{\frac{1}{\delta^2} - \frac{1}{M}}. \quad (4.22)$$

The Scalar b is the limit border for the decision of the robust algorithm [70]:

$$\mathbf{w}_R = \mathbf{f}_c + \begin{cases} \mathbf{v} & \text{for } |\mathbf{v}|^2 \leq b^2 \\ \frac{b\mathbf{v}}{|\mathbf{v}|} & \text{for } |\mathbf{v}|^2 > b^2 \end{cases} \quad (4.23)$$

Figure 26 provides a graphical interpretation of the ABF Algorithm and its robust version.

In the case of an adaptive beamformer, at each snapshot the BF robust algorithm checks if the module of the null space projection $\mathbf{v}(k+1)$, in $\mathbf{w}(k+1) = \mathbf{f}_c + \mathbf{v}(k+1)$, is greater than the constraining boundary limit b . If positive the robust update $\mathbf{w}_R(k+1)$ is restrained to the boundary.

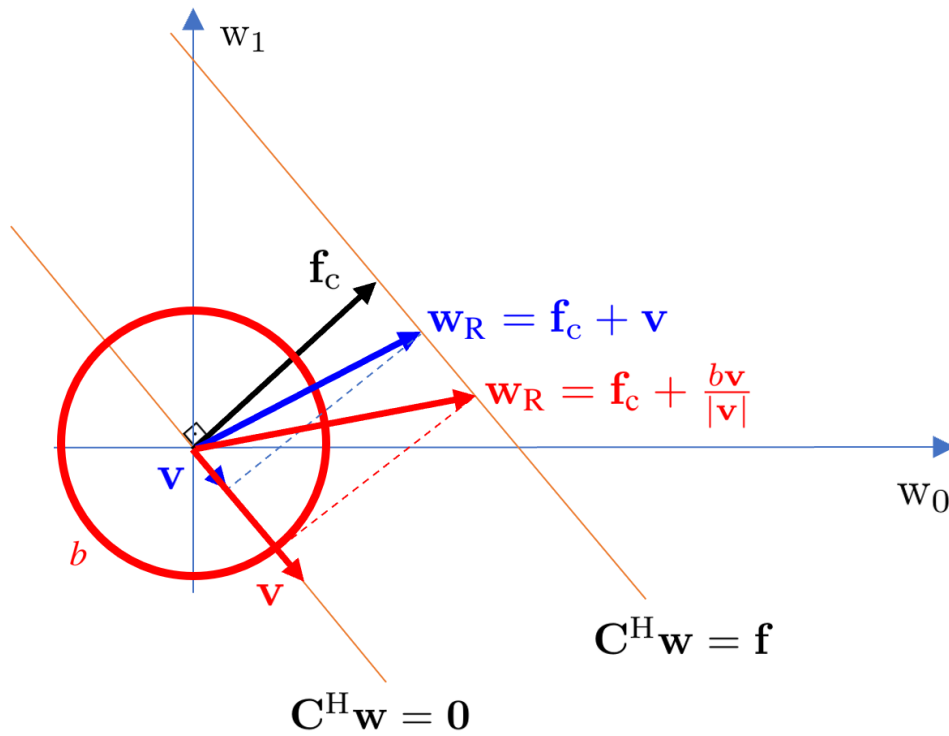


Figure 26 – Graphical interpretation of the BF Algorithm and its robust version. The blue vector is the regular robust BF case and the red vector stands for the restrained robust BF result.

4.7.2 The Robust NP-SLS MPDR Algorithm

Along with the robust design, in order to control the sidelobe levels we employ the NP-SLS Algorithm, resulting in the Robust NP-SLS ABF (RNP-SLS ABF). Before delving into the adaptive version, we first go over the Robust NP-SLS MPDR Algorithm (RNP-SLS MPDR), depicted in Algorithm 4. It has as input data the covariance matrix with MC and the SOI isotropic SV. The algorithm initializes with the coefficient vector MPDR-MC and performs the robust algorithm from Equation (4.23), resulting in the robust MPDR-MC (RMPDR-MC). It then calculates the RMPDR-MC beampattern and detects the greatest sidelobe level, incorporating an additional restriction to the adaptive filter in the form of an SV with the sidelobe direction. This additional restriction reduces the detected SLL by placing a null on its direction. It stops when the length of $\mathbf{C} < M$, so that the filter uses the most constraints possible.

Algorithm 4 The Robust NP-SLS MPDR-MC Beamformer

Input data: $\bar{\mathbf{R}}_x$ ▷ MC Snapshot Covariance matrix
 $\mathbf{a}(\phi_1)$ ▷ SOI Isotropic Steering Vector

Initialization:
 $\mathbf{w}_{\text{RMDPR-MC}} = \frac{\bar{\mathbf{R}}_x^{-1} \mathbf{a}(\phi_1)}{\mathbf{a}^H(\phi_1) \bar{\mathbf{R}}_x^{-1} \mathbf{a}(\phi_1)}$ after robustness test in Equation 4.23
BP RMPDR-MC(ϕ) = $|\mathbf{w}_{\text{RMDPR-MC}}^H \mathbf{a}(\phi)|$ ▷ $\forall \phi \in$ visible region
From the peaks of BP RMPDR-MC(ϕ), find SLL and ϕ_{SL}
 $\mathbf{C} \leftarrow [\mathbf{a}(\phi_1) \ \mathbf{a}(\phi_{\text{SL}})]$
 $\mathbf{f} \leftarrow [1 \ 0]^T$
 $\mathbf{w}_{\text{RNP-SLS}} \leftarrow \mathbf{w}_{\text{RMDPR-MC}}$
while length (C) < M do
 $\mathbf{w}_{\text{RNP-SLS}} \leftarrow \bar{\mathbf{R}}_x^{-1} \mathbf{C} (\mathbf{C}^H \bar{\mathbf{R}}_x^{-1} \mathbf{C})^{-1} \mathbf{f}$
BP RNP-SLS(ϕ) = $|\mathbf{w}_{\text{RNP-SLS}}^H \mathbf{a}(\phi)|$
From the peaks of BP RNP-SLS(ϕ), find SLL and ϕ_{SL}
 $\mathbf{C} \leftarrow [\mathbf{C} \ \mathbf{a}(\phi_{\text{SL}})]$
 $\mathbf{f} \leftarrow [\mathbf{f}^T \ 0]^T$
end

4.7.3 The Robust NP-SLS Algorithm for ABF

Similar to its optimum version, the RNP-SLS ABF Algorithm aims to receive an updated weight vector \mathbf{w}_B from the robust ABF (RABF), along with the restriction vectors \mathbf{C} and \mathbf{f} . Hereafter, it detects the sidelobe with the greatest level and incorporates an SV for the direction of the SL as an additional linear restriction to the linear constrained adaptive filter. This originates an updated weight vector \mathbf{w}_A .

The RNP-SLS ABF proposed is Algorithm 5. Figure 27 presents a schematic of the strategy of Algorithm 5.

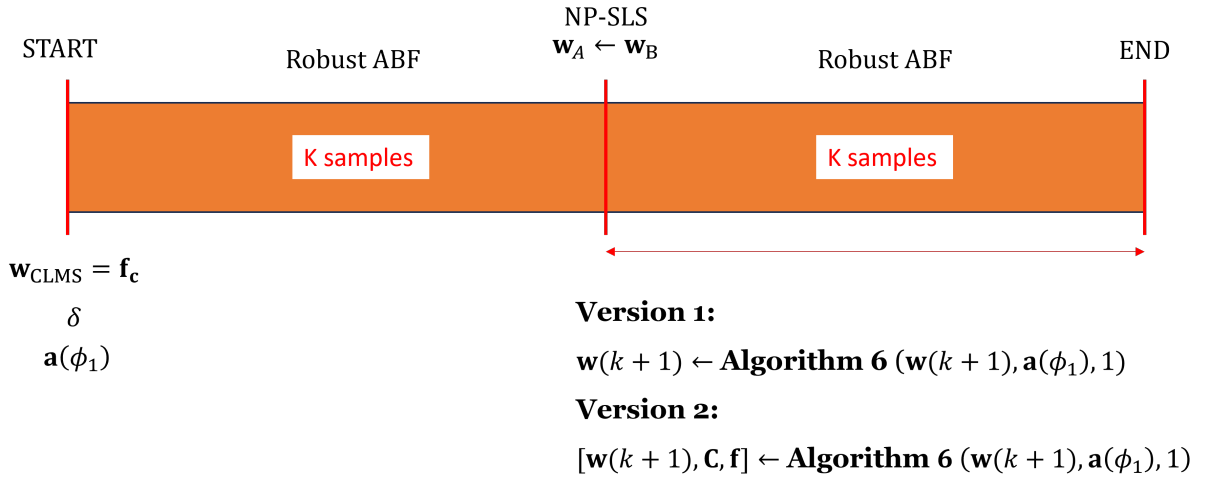


Figure 27 – Strategy of the RNP-SLS ABF Algorithm.

It uses the NP-SLS Algorithm 6 as a function. The required input data are the snapshots and the isotropic SOI SV, being the realistic AMV unknown to the algorithm. Also, it requires setting the constraining value δ . Based on the linear constraints, it calculates the projection matrix \mathbf{P} and the quiescent weight vector, \mathbf{f}_c , as initialization. Following that, it updates the ABF weight vector based on each snapshot in each iteration, and on the robust design process. The strategy behind it is to perform the Robust ABF up to the end of a sample block with K snapshots, and, by the end of the block, to decide among two optional versions. Both versions call Algorithm 6, which performs the SLL control returning the updated weight vector. While Version 1 keeps the single restriction of the distortionless constraint, given as the SOI SV, Version 2, on the other hand, returns all additional restrictions generated by Algorithm 6 and not only the SOI SV restriction. Algorithm 5 shows both versions. We have also evaluated other strategies concerning the time to call Algorithm 6 besides the one described, such as at the beginning of the sample block or at different times during the block. The results showed to be the same except for when calling Algorithm 6 at the beginning before the robust ABF, which degrades the final SINR.

Algorithm 5 The RNP-SLS ABF Algorithm

Input data: $\bar{\mathbf{x}}(k)$

▷ Snapshots with Mutual Coupling

Initialization:

$$\mathbf{C} = \mathbf{a}(\phi_1)$$

▷ ϕ_1 is the DOA of the SOI

$$\mathbf{f} = \mathbf{1}$$

▷ Distortionless constraint

$$\mathbf{P} = \mathbf{I}_{M \times M} - \mathbf{C}(\mathbf{C}^H \mathbf{C})^{-1} \mathbf{C}^H$$

▷ M sensors

$$\mathbf{f}_c = \mathbf{C}(\mathbf{C}^H \mathbf{C})^{-1} \mathbf{f}$$

▷ Quiescent weight vector

$$b = \sqrt{\frac{1}{\delta^2} - \frac{1}{M}}$$

▷ Robust constraint border

$$\mathbf{w}(k) = \mathbf{f}_c$$

Choose: K (sample block), and δ (robust design constraining limit)for each k do

$$\mathbf{w}(k+1)$$

▷ ABF update

$$\mathbf{v}(k+1) = \mathbf{P}\mathbf{w}(k+1)$$

$$\text{if } |\mathbf{v}(k+1)|^2 > b^2$$

▷ Robust design decision

$$\mathbf{w}(k+1) = \frac{b\mathbf{v}(k+1)}{|\mathbf{v}(k+1)|} + \mathbf{f}_c$$

else

$$\mathbf{w}(k+1) = \mathbf{v}(k+1) + \mathbf{f}_c$$

if $\text{mod}(k, K) = 0$ do

Version 1:

$$\mathbf{w}(k+1) \leftarrow \text{Algorithm 6}(\mathbf{w}(k+1), \mathbf{a}(\phi_1), 1)$$

Version 2:

$$[\mathbf{w}(k+1), \mathbf{C}, \mathbf{f}] \leftarrow \text{Algorithm 6}(\mathbf{w}(k+1), \mathbf{a}(\phi_1), 1)$$

$$\mathbf{P} = \mathbf{I}_{M \times M} - \mathbf{C}(\mathbf{C}^H \mathbf{C})^{-1} \mathbf{C}^H$$

$$\mathbf{f}_c = \mathbf{C}(\mathbf{C}^H \mathbf{C})^{-1} \mathbf{f}$$

end

end

Algorithm 6 The NP-SLS AlgorithmInput data: \mathbf{w}_{RABF} , \mathbf{C} and \mathbf{f}

Initialization:

$\text{BP RABF}(\phi) = |\mathbf{w}_{\text{RABF}}^{\text{H}} \mathbf{a}(\phi)|$ $\triangleright \forall \phi \in \text{visible region}$
 From the peaks of BP RABF(ϕ), find SLL and ϕ_{SL}
 $NrLoops \leftarrow 0$
 while length (\mathbf{C}) $> M$ do
 $NrLoops \leftarrow NrLoops + 1$
 $\mathbf{C}_A \leftarrow [\mathbf{C} \ \mathbf{a}(\phi_{\text{SL}})]$
 $\mathbf{f}_A \leftarrow [\mathbf{f}^{\text{T}} \ 0]^{\text{T}}$
 $\mathbf{w}_{\text{NP-SLS}} \leftarrow \frac{1}{2} \mathbf{w}_{\text{RABF}} + \dots$
 $\frac{1}{2} \mathbf{C}_A (\mathbf{C}_A^{\text{H}} \mathbf{C}_A)^{-1} [\mathbf{C} - \mathbf{a}(\phi_{\text{SL}})]^{\text{H}} \mathbf{w}_{\text{RABF}}$
 BP NP-SLS(ϕ) = $|\mathbf{w}_{\text{NP-SLS}}^{\text{H}} \mathbf{a}(\phi)|$
 From the peaks of BP NP-SLS(ϕ), find SLL and ϕ_{SL}
 $\mathbf{C} \leftarrow \mathbf{C}_A$
 $\mathbf{f} \leftarrow \mathbf{f}_A$
 end
 Returns: $\mathbf{w}_{\text{NP-SLS}}$, and, in the case of Version 2, \mathbf{C} and \mathbf{f}

4.8 Analysis of Computational Complexity

The computational burden of the proposed RNP-SLS approach applied to an ABF primarily arises from updating the constrained beamforming algorithm, performing the robustness test, and executing the eventual scaling. The robust scaling complexity described in [70] consists of M multiplications to compute $|\mathbf{v}|^2$ and perform the robustness test, one square root operation to determine $|\mathbf{v}|$, followed by M multiplications and one division to compute the update term \mathbf{v}_b . This computational cost is significantly lower compared to other robust beamformer designs, such as those in [88, 90–92], where the complexities are typically on the order of $\mathcal{O}(M^3)$ or higher. In contrast, the proposed approach leverages the NP-SLS technique, applied once per a large block of snapshots, with a computational complexity of $\mathcal{O}(NM)$ under the condition $N \gg M$, which is always satisfied in our scenarios.

4.9 Simulation Results

This Section presents the simulation results concerning three stationary signals (one SOI at 110° and two jammers, J1 and J2, at 55° and 135°) received and processed by the beamformer architecture from Figure 1 using the constrained least mean squares (CLMS) algorithm. The update equation of the CLMS algorithm considering mutual coupling may be represented as $\bar{\mathbf{w}}_{\text{CLMS}}(k+1) = \mathbf{P} [\mathbf{w}(k) + \mu e^*(k) \bar{\mathbf{x}}(k)] + \mathbf{f}_c$, where $e(k) = -\mathbf{w}^H(k) \bar{\mathbf{x}}(k)$, $\mathbf{P} = \mathbf{I}_{M \times M} - \mathbf{C} (\mathbf{C}^H \mathbf{C})^{-1} \mathbf{C}^H$, and $\mathbf{f}_c = \mathbf{C} (\mathbf{C}^H \mathbf{C})^{-1} \mathbf{f}$. It is noteworthy to highlight that, since the realistic AMV is unknown, \mathbf{C} uses $\mathbf{a}(\phi_1)$ instead of $\bar{\mathbf{a}}(\phi_1)$, thus $\mathbf{C} = [\mathbf{a}(\phi_1) \cdots \mathbf{a}(\phi_D)]$.

Figures 28, 29, and 30 depict the BP of the Robust NP-SLS CLMS (RNP-SLS CLMS) Algorithms, Versions 1 and 2 (V1 and V2), for two blocks of $K = 50,000$ snapshots each, initialized with the quiescent weight vector (\mathbf{f}_c) for the dipole, bowtie, and microstrip arrays.

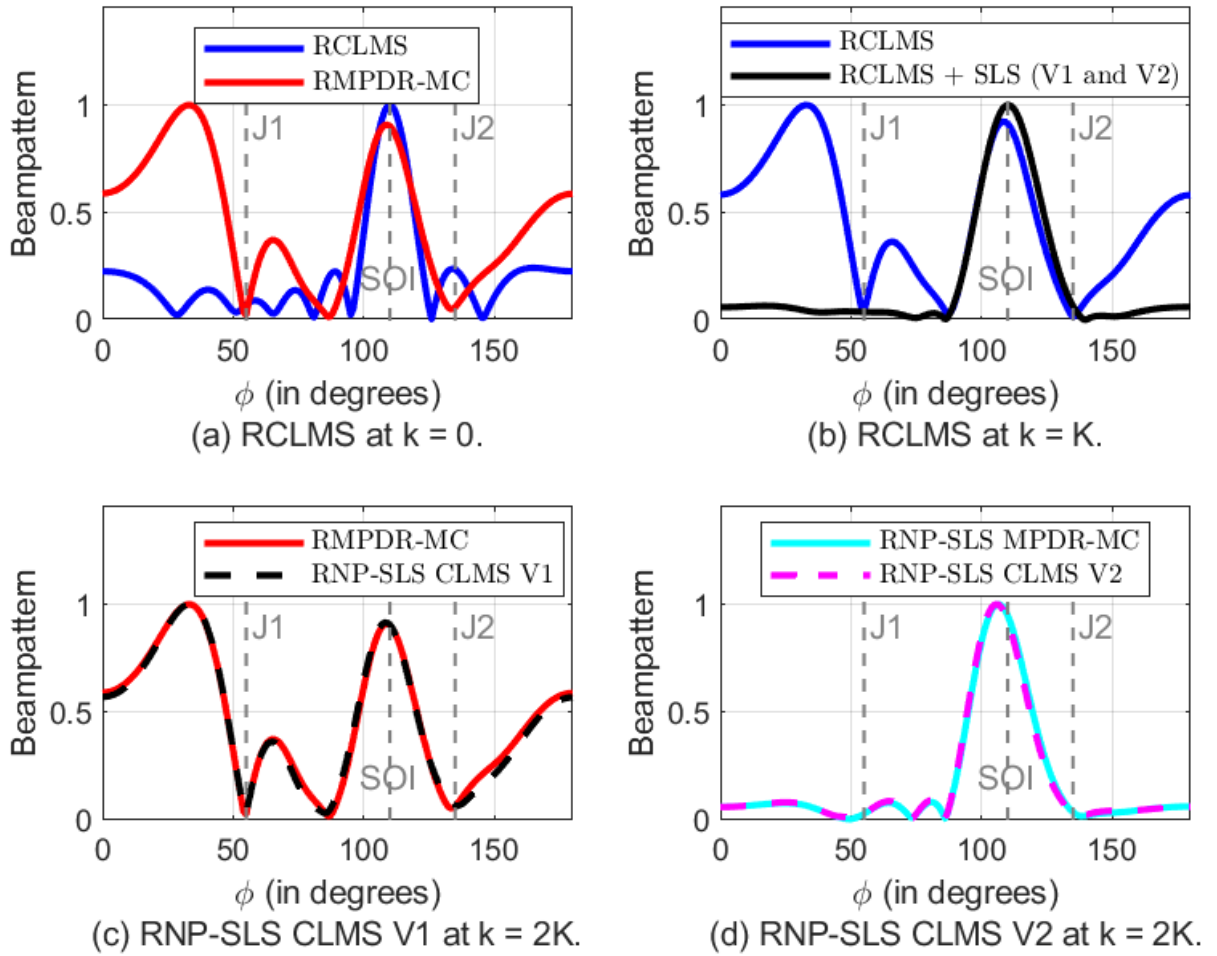


Figure 28 – BP of the dipole array using the RNP-SLS CLMS algorithms, versions 1 and 2, for two blocks of $K = 50,000$ snapshots each.

The constraining value used for the robust technique, as in [70], is the one that

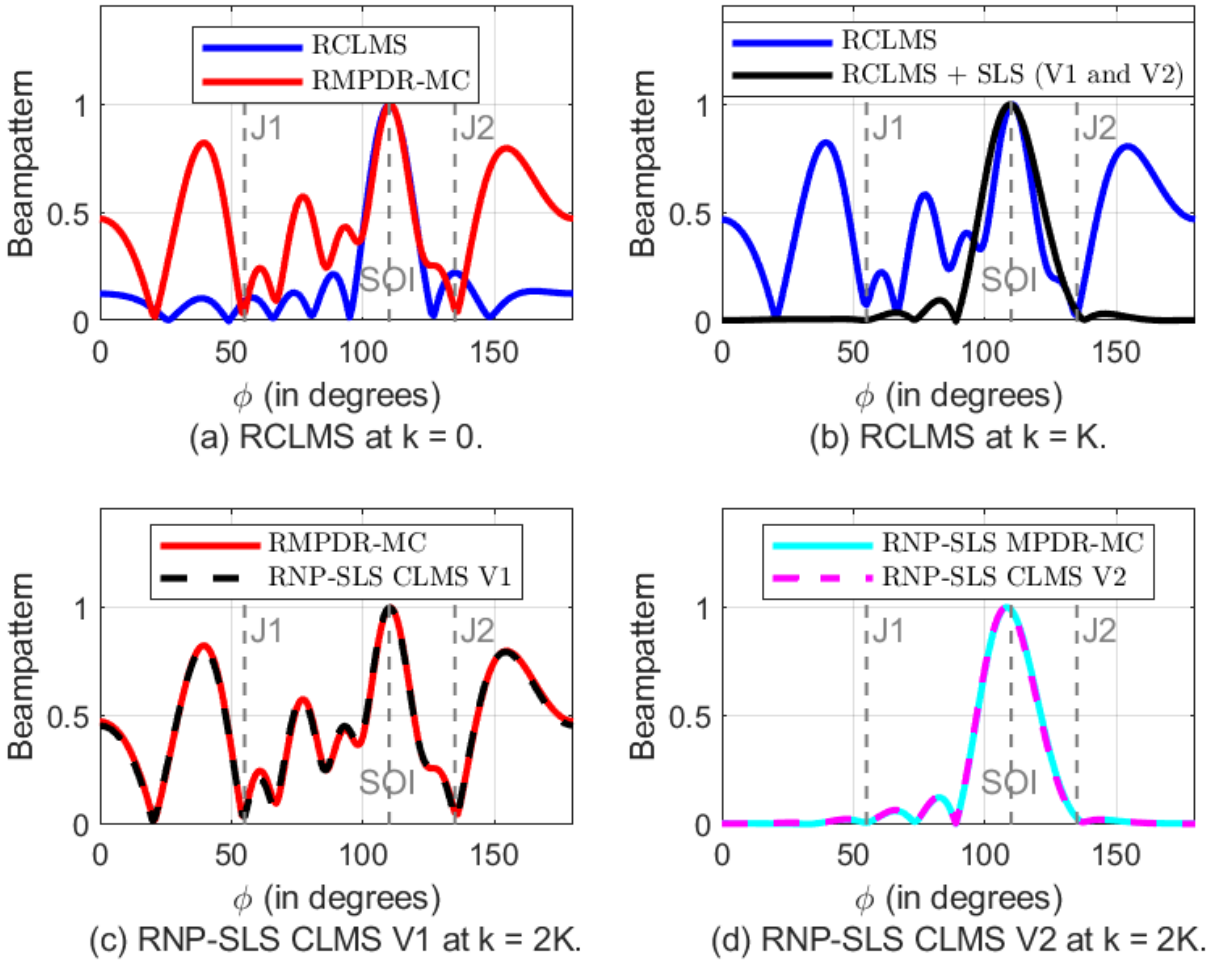


Figure 29 – BP of the bowtie array using the RNP-SLS CLMS algorithms, versions 1 and 2, for two blocks of $K = 50,000$ snapshots each.

produces the best result for each array after extensive evaluation. We have employed $\delta = 2$ since it provides the best results ensuring adequate convergence of the ABF. As seen in Figures 28 (a), 29 (a), and 30 (a), the robust CLMS (RCLMS) algorithm was initialized with the quiescent weight vector which, for this example, has at least one sidelobe in the direction of one of the jammers.

In Figures 28 (b), 29 (b), and 30 (b) the RCLMS algorithm V1 and V2 before NP-SLS, after $K = 50,000$ snapshots, converge to a beampattern quite close to the RMPDR-MC solution. This, nonetheless, restates the MPDR-MC as an appropriate model for the optimum mutual coupling solution. After the NP-SLS, the BP presents a high SL attenuation, including towards the DOA of the jammers, however at the expense of an increase in the main lobe beamwidth.

Figures 28, 29, and 30 (c) and (d) display the behavior of the RNP-SLS CLMS Algorithm Versions 1 and 2 at the end of the second block, after $k = 2K$ snapshots. Version 1, keeping only the distortionless response, converges back to the RMPDR-MC, as in the end of the block before NP-SLS. On the other hand, Version 2, carrying the SOI

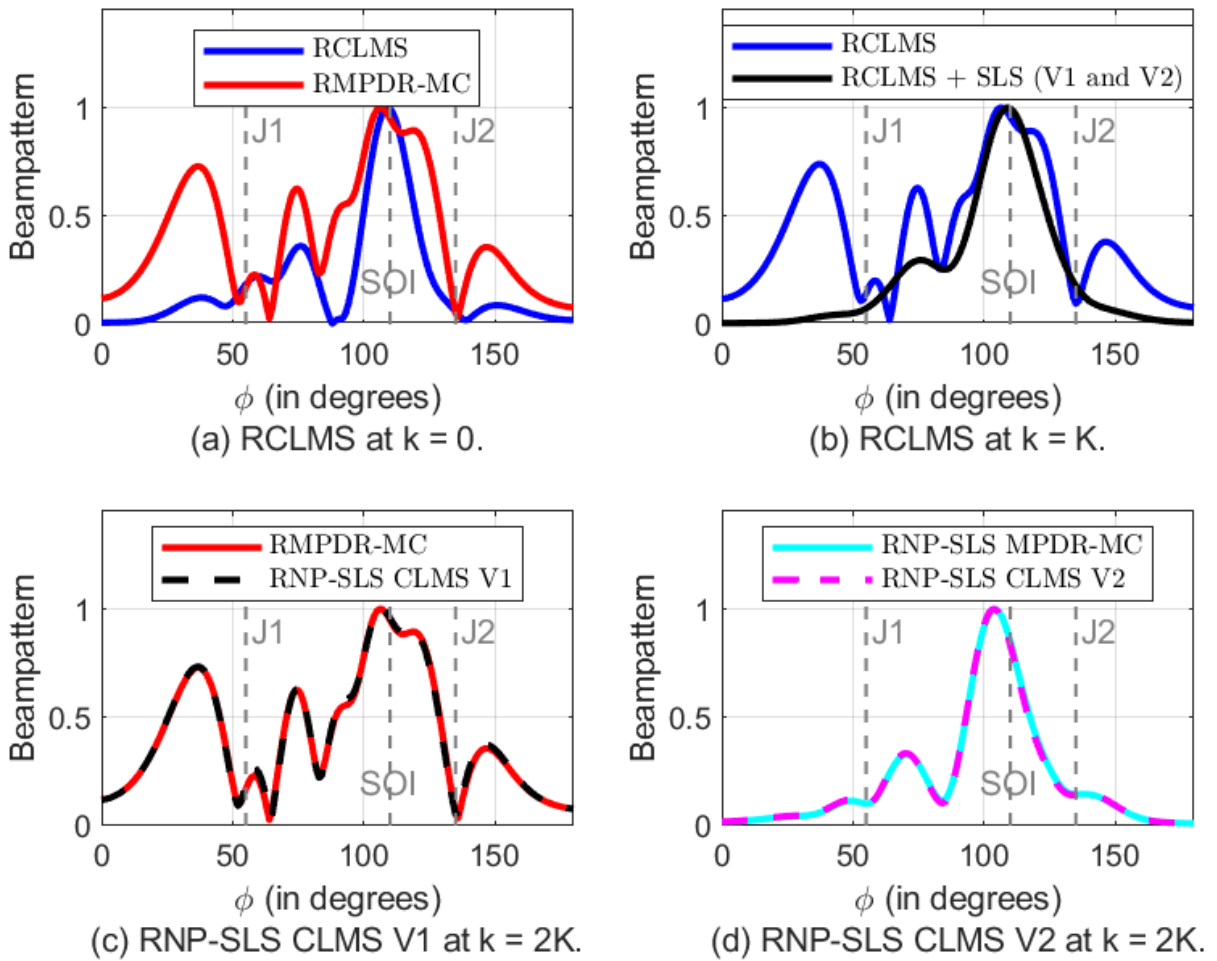


Figure 30 – BP of the microstrip array using the RNP-SLS CLMS algorithms, versions 1 and 2, for two blocks of $K = 50,000$ snapshots each.

SV plus 6 additional constraints, does not converge to the RMPDR-MC, but rather to the RNP-SLS MPDR, which is the robust version of the MPDR-MC with all the additional constraints. Version 2 BP presents a high SL attenuation with some, not perfect, nulling on the jammers and some main lobe displacement. Still, V2 BP is a much less distorted BP than the one from RMPDR-MC, for all three arrays.

Figure 31 compares the SINR performance of the RNP-SLS CLMS Algorithms, Versions 1 and 2 (V1 and V2), for two blocks of $K = 50,000$ snapshots each.

As seen in Figure 31, for all arrays, in the first block the SINR of the RNP-SLS CLMS V1 and V2 decrease tending to the RMPDR-MC solution, at the same pace since they are identical in this first block. In the second block, the NP-SLS on both V1 and V2 present a significant increase in the SINR for the three arrays. The difference between SINR levels among the different arrays is due to their different mutual coupling levels, as previously discussed.

After sidelobe suppression the SINR from the RNP-SLS CLMS V1 drops to the previous level before the NP-SLS procedure, converging back to the level of the RMPDR-

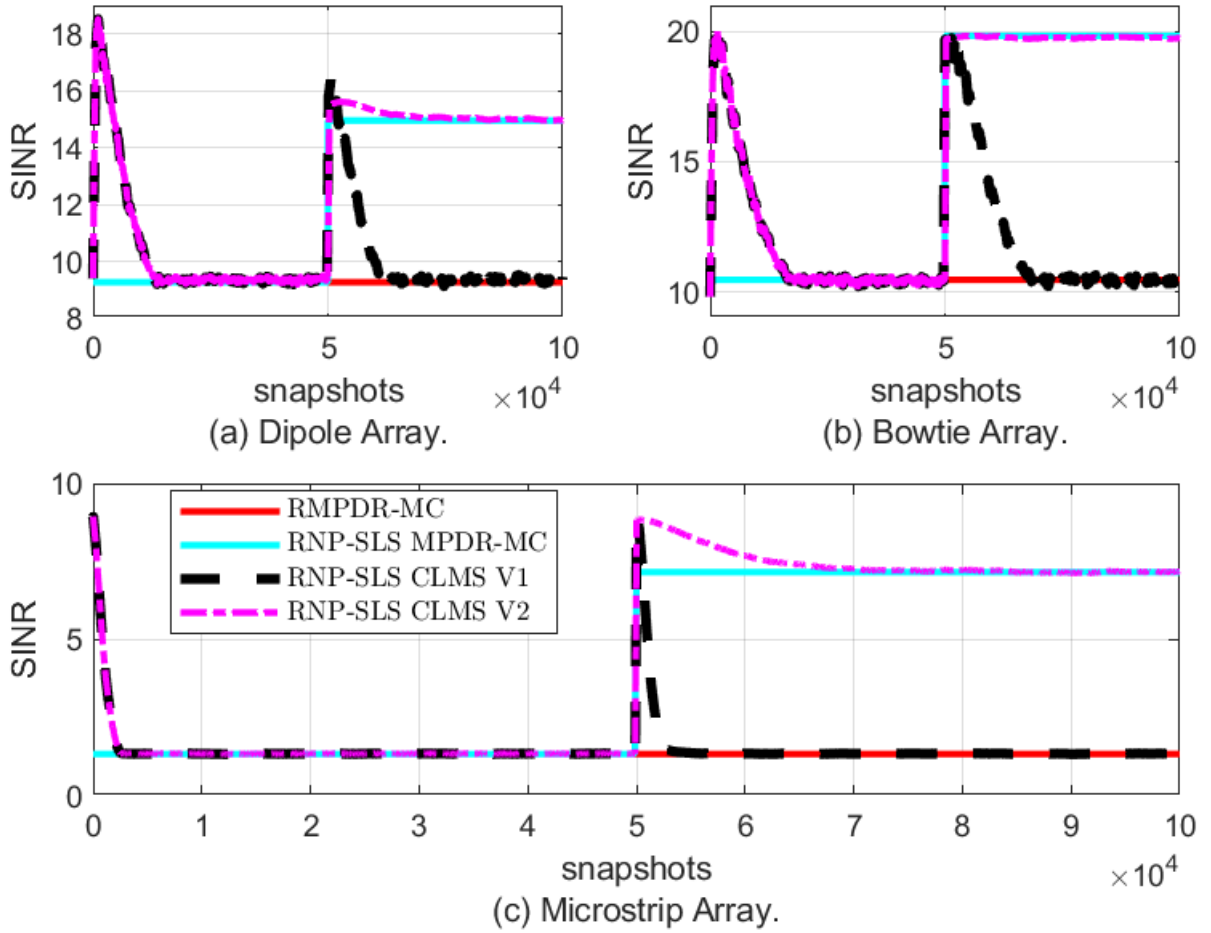


Figure 31 – Comparing the SINR (linear) performance of the RNP-SLS CLMS algorithms, V1 and V2, for two blocks of $K = 50,000$ snapshots each.

MC for all arrays. Version 2, on the other hand, has a slight decrease and converges to RNP-SLS MPDR, keeping most of the gained SINR. Finally, the findings from Figures 28 to 31, point out that, for all arrays, the RNP-SLS CLMS Algorithm Version 2 improves the beam patterns by reducing the sidelobes and performing some main lobe displacement towards the SOI, maintaining reasonable nulling capability when compared to the optimum Robust MPDR-MC solution.

Table 6 presents the final SINR achieved by the NP-SLS and Robust Techniques isolated and by their combination, for the dipole, bowtie, and microstrip arrays.

As seen in the first line of Table 6, the MPDR with knowledge of the $\bar{\mathbf{a}}(\phi)$ presents the highest results, which are higher for the arrays with lower mutual coupling. On the other hand, the MPDR-MC beamformer presents the lowest final SINR values. In the third line, we can see that the SINR values increase significantly when employing only the robust technique. The NP-SLS technique also provides meaningful SINR increase when applied alone, except for the dipole array; as seen on the fourth line we observe a difficulty in suppressing the side lobes and enforcing the distortionless constraint. However, when

Table 6 – Final SINR (linear) achieved by the NP-SLS and robust techniques and their combination

Techniques	Dipole Array	Bowtie Array	Microstrip Array
MPDR	21.2	23.17	17.56
MPDR-MC	6.5	8.51	0.16
RMPDR-MC	9.27	10.48	1.35
NP-SLS MPDR-MC	0.059	19.85	6.5
RNP-SLS MPDR-MC	14.9	19.89	7.3

combined, the NP-SLS and Robust techniques present better SINR results for all the studied arrays. The difficulty found by the NP-SLS technique alone on the dipole array mutual coupling is apparently resolved when applying the robust technique combined. Different SOI angles have also been tested yielding similar results as in Table 6 except when too close to the jammer so that the beamformer lacks resolution with the current array elements.

As an additional evaluation of the proposed solution's performance, Table 7 presents the final front-to-sidelobe ratio (SLL), measured in decibels (dB), achieved when combining the NP-SLS and robust techniques for the dipole, bowtie, and microstrip antenna arrays. The results indicate that the bowtie array has the smallest final SLL, followed by the dipole array, with the microstrip array having the largest SLL. This trend is consistent with the mutual coupling levels observed in the three arrays and with the results of the Signal-to-Interference-plus-Noise Ratio (SINR) analysis.

Table 7 – Final front-to-sidelobe ratio (dB), or SLL, achieved by the NP-SLS and robust techniques and their combination

	Dipole Array	Bowtie Array	Microstrip Array
Front-to-sidelobe ratio (dB)	-18.66	-22.3	-10.42

As we approach the end of this text, it is important to highlight that the proposed solution offers, besides the mitigation of the mutual coupling effects measured in terms SINR or evaluated as front-to-side ratio, also the ability to reject new interferers in the directions of the sidelobes when the adaptive beamformer still did not converge to reject them, which could be referred to as an enhanced adaptive interference suppression.

5 CONCLUSION

To conclude this work, this chapter presents a summary of the key findings, followed by a discussion on potential directions for future research, and ended by the published and submitted papers.

5.1 Final Considerations

In the current days, the electromagnetic environment is considered to be dense and the signals of interest are frequently mixed with interference and noise, reducing the signal-to-interference plus noise ratio. As a part of this context, our endeavor with this research was to contribute to the field of adaptive beamforming and the rise of SINR in electronic warfare receivers. Our research was divided into two main fronts or themes that initially were not related and, as the work advanced, the first contributed significantly to the second.

The first theme was the sidelobe suppression in adaptive beamforming techniques. The work studied a scheme to perform sidelobe suppression to adaptive beamformers using null placement and, based on that, developed and proposed our approach employing constrained adaptive algorithms. The NP-SLS approach incorporates linear constraints to the ABF algorithm placing nulls on the detected sidelobes above a specified minimum level. The simulated results demonstrate the effectiveness of the proposed approach in controlling SLL and its effect on adaptive interference suppression for different numbers of antennas, however at the expense of slower convergence. For longer blocks, a small global SINR reduction was detected, while for shorter blocks the sidelobe suppression improves the SINR.

The second theme concerned mutual coupling in antenna arrays. We studied the signal-impairing effects caused by the mutual coupling between antenna array elements and proposed a technique to mitigate the signal distortion for the practical situation when the realistic array manifold vector is unknown and the array is not compensated or calibrated. This is done without relying on the assumption that the mutual coupling matrix has a specific structure, e.g., Toeplitz. The first important result was the computation of an optimum beamformer version, MPDR-MC, which is the solution to which an adaptive beamforming would converge in case of mutual coupling when the realistic array manifold vector is unknown. Second, we propose an approach that, given only the SOI isotropic steering vector and incoming snapshots, combines a robust design with a sidelobe suppression technique to mitigate the main mutual coupling distortion effects to the beampattern and, therefore, significantly enhance the SINR. It may be used as a mutual coupling resistant technique for unknown and uncalibrated arbitrary arrays. These findings

provide a foundation for future research in mutual coupling signal distortion mitigation and adaptive beamforming with robust techniques and enhanced sidelobe control.

5.2 Future Work

For future research, some topics can be investigated. Different methods for modeling the mutual coupling can be used, as for example the ones from [71] and [31]. Particularly the one from [71] requires fewer electromagnetic simulations since instead of requiring the embedded and the isolated radiation patterns, it requires only the loaded radiation pattern when all terminals are loaded and matched. It would be helpful to have fewer electromagnetic simulations required when working with array geometries more complex than the ULA, i.e., that allow resolution capability in more than one direction.

Concerning the robust design, there are several different design principles that can be evaluated in the pursuit of better performances, as related in e.g. [88, 89, 93]: diagonal loading-based, generalized sidelobe canceler, eigenspace projection, worst-case optimization, steering vector estimation, and support vector machines, among others. It is important, however, to bear in mind that each of these approaches has different required input data that may be unavailable depending on the application. For our case, the beamformer and its robust design have no additional information rather than the isotropic AMV, the snapshots, and the SOI steering vector.

5.3 Published and Submitted Papers

1. "Exploring Adaptive Beamformers with the Null Placing Sidelobe Suppression Algorithm," 2024 19th International Symposium on Wireless Communication Systems (ISWCS), Rio de Janeiro, Brazil, 2024, pp. 1-6.
Available at <<https://ieeexplore.ieee.org/document/10639135>> DOI: 10.1109/ISWCS61526.2024.10639135
2. "A Mutual Coupling Resistant Approach for Uncalibrated Narrowband Beamformers".
Submitted to The IEEE Transactions on Vehicular Technology, 2025.
3. "Equivalent diagonal mutual coupling matrices for narrowband ULA beamformers.
Submitted to 23rd IEEE NEWCAS Conference, Paris-France, 2025.

BIBLIOGRAPHY

- 1 GORDON, D. E. *Electronic Warfare*. first. [S.l.]: Pergamon, 1981. ISBN 978-1-4831-9722-7.
- 2 GROUP., T. *Website: Communications Electronic Warfare*. 2023. <https://www.thalesgroup.com/en/markets/defence-and-security/radio-communications/naval-communications/communications-electronic>. Accessed on November 28th, 2023.
- 3 EMSOPEDIA. *Website: Communication Electronic Support Measures (CESM)*. 2023. <https://www.emsopedia.org/entries/communication-electronic-support-measures-cesm/>. Accessed on December 03rd, 2023.
- 4 TREES, H. V. *Optimum Array Processing: Part IV of Detection, Estimation, and Modulation Theory*. [S.l.]: Wiley, 2004. (Detection, Estimation, and Modulation Theory). ISBN 9780471463832.
- 5 HARTAL, O. *Electromagnetic Compatibility by Design: Circuit Design, Mechanical Packaging, Shielding, Filtering, Cable Type and Layout, Software*. [S.l.]: R & B Enterprises, 1995.
- 6 DINIZ, P. S. R.; CAMPOS, M. L. R. de; MARTINS, W. A.; LIMA, M. V. S.; APOLINÁRIO JR, J. A. *Online Learning and Adaptive Filters*. [S.l.]: Cambridge University Press, 2022.
- 7 KLINGELFUS, V. T.; SERRANO, A. L. C.; REHDER, G. P. Co-site interference study and mitigation onboard a submarine between communication and positioning systems at L band. *IEEE Letters on Electromagnetic Compatibility Practice and Applications*, v. 3, n. 1, p. 38–42, 2021.
- 8 GRAVAS, I. P.; ZAHARIS, Z. D.; YIOULTSIS, T. V.; LAZARIDIS, P. I.; XENOS, T. D. Adaptive beamforming with sidelobe suppression by placing extra radiation pattern nulls. *IEEE Transactions on Antennas and Propagation*, v. 67, n. 6, p. 3853–3862, 2019.
- 9 GOUDOS, S. K.; REKANOS, I. T.; SAHALOS, J. N. EMI reduction and ICS optimal arrangement inside high-speed networking equipment using particle swarm optimization. *IEEE Transactions on Electromagnetic Compatibility*, v. 50, n. 3, p. 586–596, 2008.
- 10 REKANOS, I. T. Shape reconstruction of a perfectly conducting scatterer using differential evolution and particle swarm optimization. *IEEE Transactions on Geoscience and Remote Sensing*, v. 46, n. 7, p. 1967–1974, 2008.
- 11 AL-AZZA, A. A.; AL-JODAH, A. A.; HARACKIEWICZ, F. J. Spider monkey optimization: A novel technique for antenna optimization. *IEEE Antennas and Wireless Propagation Letters*, v. 15, p. 1016–1019, 2016.
- 12 EBRAHIMZADE, A.; ABEDI, H.; HESARI, M. Gravitational search algorithm used to synthesis a planar array antenna for nulling control and side lobe level reduction. In: *2016 8th International Symposium on Telecommunications (IST)*. [S.l.: s.n.], 2016. p. 391–395.

- 13 FRIEDLANDER, B. Antenna array manifolds for high-resolution direction finding. *IEEE Transactions on Signal Processing*, v. 66, n. 4, p. 923–932, 2018.
- 14 GRAVAS, I. P. Doctoral Dissertation, *Development of Beamforming Techniques for Antenna Arrays*. 2021.
- 15 FRIEDLANDER, B. Antenna array manifolds for high-resolution direction finding. *IEEE Transactions on Signal Processing*, v. 66, n. 4, p. 923–932, 2018.
- 16 SVENDSEN, A. S. C.; GUPTA, I. J. The effect of mutual coupling on the nulling performance of adaptive antennas. *IEEE Antennas and Propagation Magazine*, v. 54, n. 3, p. 17–38, 2012.
- 17 LIAO, B.; CHAN, S.-C. Adaptive beamforming for uniform linear arrays with unknown mutual coupling. *IEEE Antennas and Wireless Propagation Letters*, v. 11, p. 464–467, 2012.
- 18 LUI, H.-S.; HUI, H. T.; LEONG, M. S. A note on the mutual-coupling problems in transmitting and receiving antenna arrays. *IEEE Antennas and Propagation Magazine*, v. 51, n. 5, p. 171–176, 2009.
- 19 HOOP, A. T. D. The n-port receiving antenna and its equivalent electrical network. *IEEE Transactions on Antennas and Propagation*, Philips Res. Repts, n. 30, p. 302–315, 1975.
- 20 CRAEYE, C.; GONZÁLEZ-OVEJERO, D. A review on array mutual coupling analysis. *Radio Science*, v. 46, n. 02, p. 1–25, 2011.
- 21 WALLACE, J. W.; MEHMOOD, R. On the accuracy of equivalent circuit models for multi-antenna systems. *IEEE Transactions on Antennas and Propagation*, v. 60, n. 2, p. 540–547, 2012.
- 22 KATAGI, T.; OHMINE, H.; MIYASHITA, H.; NISHIMOTO, K. Analysis of mutual coupling between dipole antennas using simultaneous integral equations with exact kernels and finite gap feeds. *IEEE Transactions on Antennas and Propagation*, v. 64, n. 5, p. 1979–1984, 2016.
- 23 HENAULT, S.; ANTAR, Y.; RAJAN, S.; INKOL, R.; WANG, S. The multiple antenna induced EMF method for the precise calculation of the coupling matrix in a receiving antenna array. *Progress In Electromagnetics Research M*, v. 8, p. 103–118, 01 2009.
- 24 COLLIN, R. Limitations of the Thevenin and Norton equivalent circuits for a receiving antenna. *IEEE Antennas and Propagation Magazine*, v. 45, n. 2, p. 119–124, 2003.
- 25 HENAULT, S.; ANTAR, Y. M. M. Accurate evaluation of mutual coupling for array calibration. In: *2009 Computational Electromagnetics International Workshop*. [S.l.: s.n.]. p. 34–37.
- 26 HANSEN, R. Relationships between antennas as scatterers and as radiators. *Proceedings of the IEEE*, v. 77, n. 5, p. 659–662, 1989.
- 27 HENAULT, S.; ANTAR, Y. Unifying the theory of mutual coupling compensation in antenna arrays. *IEEE Antennas and Propagation Magazine*, v. 57, n. 2, p. 104–122, 2015.

- 28 ZHANG, T.; HUI, H. Compensation for the mutual coupling effect in ESPRIT DOA estimations. In: *IEEE Antennas and Propagation Society Symposium, 2004*. [S.l.: s.n.], 2004. v. 3, p. 2816–2818 Vol.3.
- 29 CHUA, P. T.; COETZEE, J. C. Microstrip decoupling networks for low-order multiport arrays with reduced element spacing. *Microwave and Optical Technology Letters*, v. 46, n. 6, p. 592–597, 2005.
- 30 FRIEDLANDER, B. The extended manifold for antenna array calibration. In: *55th Asilomar Conference on Signals, Systems, and Computers*. [S.l.: s.n.], 2021. p. 216–220.
- 31 FRIEDLANDER, B. The extended manifold for antenna arrays. *IEEE Transactions on Signal Processing*, v. 68, p. 493–502, 2020.
- 32 RAZAVI, B. *RF Microelectronics*. [S.l.]: Pearson Education, 2011. (Prentice Hall Communications Engineering and Emerging Technologies Series from Ted Rappaport). ISBN 9780132901055.
- 33 DINIZ, P. *Adaptive Filtering: Algorithms and Practical Implementation*. [S.l.]: Springer US, 2012. (SpringerLink : Bücher). ISBN 9781461441069.
- 34 GUPTA, I.; KSIENSKI, A. Effect of mutual coupling on the performance of adaptive arrays. *IEEE Transactions on Antennas and Propagation*, v. 31, n. 5, p. 785–791, 1983.
- 35 VOROBYOV, S. A. Principles of minimum variance robust adaptive beamforming design. *Signal Processing*, v. 93, n. 12, p. 3264–3277, 2013. ISSN 0165-1684. Special Issue on Advances in Sensor Array Processing in Memory of Alex B. Gershman. Disponível em: <<https://www.sciencedirect.com/science/article/pii/S0165168412003830>>.
- 36 ZHENG, Z.; LIU, K.; WANG, W.-Q.; YANG, Y.; YANG, J. Robust adaptive beamforming against mutual coupling based on mutual coupling coefficients estimation. *IEEE Transactions on Vehicular Technology*, v. 66, n. 10, p. 9124–9133, 2017.
- 37 POZAR, D. *Microwave Engineering*. [S.l.]: Wiley, 2012. ISBN 9781118213636.
- 38 WU, Z.-J.; WANG, C.-X.; JIANG, P.-H.; ZHOU, Z.-Q. Range-doppler sidelobe suppression for pulsed radar based on golay complementary codes. *IEEE Signal Processing Letters*, v. 27, p. 1205–1209, 2020.
- 39 KIM, J. H.; CHOI, B. H.; KIM, H. R.; RIM, C. T.; KIM, Y.-S. Single-variable-input active sidelobe suppression method for synthesized magnetic field focusing technology and its optimization. *IEEE Transactions on Industrial Electronics*, v. 67, n. 11, p. 9813–9823, 2020.
- 40 LIU, S.; CAO, Y.; YEO, T.-S.; WANG, F.; HAN, J. Range sidelobe suppression for randomized stepped-frequency chirp radar. *IEEE Transactions on Aerospace and Electronic Systems*, v. 57, n. 6, p. 3874–3885, 2021.
- 41 MAO, K.; LI, Y.; LIANG, Z.; ZHENG, S. Y.; LONG, Y. Backward-to-forward scanning periodic nonuniform leaky-wave antenna for reflected sidelobe suppression. *IEEE Antennas and Wireless Propagation Letters*, v. 21, n. 8, p. 1522–1526, 2022.

- 42 WANG, Y.; ZHANG, Q.; LIN, Y.; ZHAO, Z.; LI, Y. Multi-phase-center sidelobe suppression method for circular gbsar based on sparse spectrum. *IEEE Access*, v. 8, p. 133802–133816, 2020.
- 43 YUAN, S.; YU, Z.; LI, C.; WANG, S. A novel SAR sidelobe suppression method based on CNN. *IEEE Geoscience and Remote Sensing Letters*, v. 18, n. 1, p. 132–136, 2021.
- 44 HUSSAIN, K.; LÓPEZ-VALCARCE, R. Joint precoder and window design for OFDM sidelobe suppression. *IEEE Communications Letters*, v. 26, n. 12, p. 3044–3048, 2022.
- 45 ZABELIN, A. N.; LITVINOV, O. S. Recurrent neural network application features to suppress non-stationary interference in an adaptive antenna array. In: *2023 Wave Electronics and its Application in Information and Telecommunication Systems (WECONF)*. [S.l.: s.n.], 2023. p. 1–5.
- 46 HAN, J.; NG, B. P.; ER, M. H. An adaptive orientational beamforming technique for narrowband interference rejection. In: *IEEE International Conference on Acoustics, Speech and Signal Processing (ICASSP)*. [S.l.: s.n.], 2022. p. 4908–4912.
- 47 ORNELAS-GUTIERREZ, A.; VARGAS-ROSALES, C.; VILLALPANDO-HERNANDEZ, R. Vehicular ad hoc network interference mitigation using digital beamforming approach in roundabout scenarios. *IEEE Access*, v. 11, p. 108232–108244, 2023.
- 48 WU, Z.; ZHU, S.; XU, J.; LAN, L.; ZHANG, M.; LI, X. A robust interference suppression method based on fda-mimo radar. In: *2022 5th International Conference on Information Communication and Signal Processing (ICICSP)*. [S.l.: s.n.], 2022. p. 419–423.
- 49 GE, Q.; ZHANG, Y.; WANG, Y.; ZHANG, D. Multi-constraint adaptive beamforming in the presence of the desired signal. *IEEE Communications Letters*, v. 24, n. 11, p. 2594–2598, 2020.
- 50 MILLER, S. R.; SPANIAS, A. Adaptive antenna beamforming using quiescent pattern control. *IEEE Antennas and Wireless Propagation Letters*, v. 6, p. 651–654, 2007.
- 51 KLINGELFUS, V. T.; APOLINÁRIO JR., J. A.; SAUNDERS FILHO, C. A. B.; DE LAMARE, R. C. Exploring adaptive beamformers with the null placing sidelobe suppression algorithm. In: *19th International Symposium on Wireless Communication Systems (ISWCS)*. [S.l.: s.n.], 2024. p. 1–6.
- 52 APOLINÁRIO JR., J.A.; CAMPOS, M. D.; BERNAL-OÑATE, C. P. The constrained conjugate gradient algorithm. *IEEE Signal Processing Letters*, v. 7, n. 12, p. 351–354, 2000.
- 53 YU, Y.; HUI, H. T. Design of a mutual coupling compensation network for a small receiving monopole array. *IEEE Transactions on Microwave Theory and Techniques*, v. 59, n. 9, p. 2241–2245, 2011.
- 54 ANDERSEN, J.; RASMUSSEN, H. Decoupling and descattering networks for antennas. *IEEE Transactions on Antennas and Propagation*, v. 24, n. 6, p. 841–846, 1976.
- 55 COETZEE, J. C.; YU, Y. New modal feed network for a compact monopole array with isolated ports. *IEEE Transactions on Antennas and Propagation*, v. 56, n. 12, p. 3872–3875, 2008.

- 56 SELONE, F.; SERRA, A. A novel online mutual coupling compensation algorithm for uniform and linear arrays. *IEEE Transactions on Signal Processing*, v. 55, n. 2, p. 560–573, 2007.
- 57 AFSARI, A.; ABBOSH, A. M.; RAHMAT-SAMII, Y. Adaptive beamforming by compact arrays using evolutionary optimization of Schelkunoff polynomials. *IEEE Transactions on Antennas and Propagation*, v. 70, n. 6, p. 4485–4497, 2022.
- 58 YAĞAN, M. Y.; COŞKUN, A. F.; PUSANE, A. E. A novel blind adaptive beamformer with robustness against mutual coupling and miscalibration effects. In: *17th European Conference on Antennas and Propagation (EuCAP)*. [S.l.: s.n.], 2023. p. 1–5.
- 59 PFEIFFER, C.; DAGEFU, F.; TOMASIC, B.; TWIGG, J. N.; WU, B.-I. Virtual impedance method for mutual coupling compensation. *IEEE Transactions on Antennas and Propagation*, v. 69, n. 8, p. 4569–4579, 2021.
- 60 HENAULT, S.; PODILCHAK, S. K.; MIKKI, S. M.; ANTAR, Y. M. M. A methodology for mutual coupling estimation and compensation in antennas. *IEEE Transactions on Antennas and Propagation*, v. 61, n. 3, p. 1119–1131, 2013.
- 61 ADVE, R.; SARKAR, T. Compensation for the effects of mutual coupling on direct data domain adaptive algorithms. *IEEE Transactions on Antennas and Propagation*, v. 48, n. 1, p. 86–94, 2000.
- 62 HUI, H. T. A practical approach to compensate for the mutual coupling effect in an adaptive dipole array. *IEEE Transactions on Antennas and Propagation*, v. 52, n. 5, p. 1262–1269, 2004.
- 63 YANG, S.; NIE, Z. Mutual coupling compensation in time modulated linear antenna arrays. *IEEE Transactions on Antennas and Propagation*, v. 53, n. 12, p. 4182–4185, 2005.
- 64 FREDRICK, J.; WANG, Y.; ITOH, T. Smart antennas based on spatial multiplexing of local elements (SMILE) for mutual coupling reduction. *IEEE Transactions on Antennas and Propagation*, v. 52, n. 1, p. 106–114, 2004.
- 65 FANG, W.; YU, D.; WANG, X.; XI, Y.; CAO, Z.; SONG, C.; XU, Z. A deep learning based mutual coupling correction and DOA estimation algorithm. In: *13th International Conference on Wireless Communications and Signal Processing (WCSP)*. [S.l.: s.n.], 2021. p. 1–5.
- 66 XIAO, Y.; WANG, Y. Deep learning-based mutual coupling modeling and baseband decoupling algorithm for MIMO systems. *IEEE Communications Letters*, v. 24, n. 9, p. 1986–1990, 2020.
- 67 ALZAHED, A. M.; MIKKI, S. M.; ANTAR, Y. M. M. Nonlinear mutual coupling compensation operator design using a novel electromagnetic machine learning paradigm. *IEEE Antennas and Wireless Propagation Letters*, v. 18, n. 5, p. 861–865, 2019.
- 68 AUBRY, A.; MAIO, A. D.; LAN, L.; ROSAMILIA, M. Adaptive radar detection and bearing estimation in the presence of unknown mutual coupling. *IEEE Transactions on Signal Processing*, v. 71, p. 1248–1262, 2023.

- 69 WU, Y. I.; ARADA, G. P.; TAM, W.-Y.; WONG, K. T. Mis-modeling and mis-correction of mutual coupling in an antenna array — a case study in the context of direction finding using a linear array of identical dipoles. In: *IEEE International Conference on Signal and Image Processing (ICSIP)*. [S.l.: s.n.], 2016. p. 447–451.
- 70 COX, H.; ZESKIND, R.; OWEN, M. Robust adaptive beamforming. *IEEE Transactions on Acoustics, Speech, and Signal Processing*, v. 35, n. 10, p. 1365–1376, 1987.
- 71 FRIEDLANDER, B. On the mutual coupling matrix in array signal processing. In: *54th Asilomar Conference on Signals, Systems, and Computers*. [S.l.: s.n.], 2020. p. 1245–1249.
- 72 FRIEDLANDER, B. The extended manifold for diversely polarized antenna arrays. In: *53rd Asilomar Conference on Signals, Systems, and Computers*. [S.l.: s.n.], 2019. p. 1262–1266.
- 73 BALANIS, C. *Antenna Theory: Analysis and Design*. [S.l.]: Wiley, 2015. ISBN 9781119178989.
- 74 KING, R. The linear antenna—eighty years of progress. *Proceedings of the IEEE*, v. 55, n. 1, p. 2–16, 1967.
- 75 JOHNSON, R.; JASIK, H. *Antenna Engineering Handbook*. [S.l.]: McGraw-Hill, 1993. (Electronics Electrical Engineering). ISBN 9780070323810.
- 76 BALANIS, C. *Advanced Engineering Electromagnetics*. [S.l.]: Wiley, 2012. (CourseSmart Series). ISBN 9780470589489.
- 77 HANSEN, R. *Phased Array Antennas*. [S.l.]: Wiley, 1998. (Wiley Series in Microwave and Optical Engineering). ISBN 9780471530763.
- 78 STUTZMAN, W.; THIELE, G. *Antenna Theory and Design*. [S.l.]: Wiley, 2012. (Antenna Theory and Design). ISBN 9780470576649.
- 79 BURKE, G. J.; POGGIO, A. J.; LOGAN, J. C.; ROCKWAY, J. W. Numerical electromagnetic code (NEC). In: *IEEE International Symposium on Electromagnetic Compatibility*. [S.l.: s.n.], 1979. p. 1–3.
- 80 BURKE, G.; MILLER, E.; POGGIO, A. The numerical electromagnetics code (NEC) - a brief history. In: *IEEE Antennas and Propagation Society Symposium*. [S.l.: s.n.], 2004. v. 3, p. 2871–2874 Vol.3.
- 81 HARRINGTON, R. Origin and development of the method of moments for field computation. *IEEE Antennas and Propagation Magazine*, v. 32, n. 3, p. 31–35, 1990.
- 82 KLINGELFUS, V. T.; APOLINÁRIO JR., J. A.; SAUNDERS FILHO, C. A. B.; RAMOS, A. L. L. Equivalent diagonal mutual coupling matrices for narrowband ULA beamformers. *Submitted to 23rd IEEE NEWCAS Conference, Paris-France, 2025*.
- 83 ANSYS. *Website: Ansys HFSS*. 2024. <https://www.ansys.com/products/electronics/ansys-hfsstab1-1>. Accessed on August 29th, 2024.
- 84 CORPORATION, R. *Website: RT/duroid® 5880 Laminates*. <https://www.rogerscorp.com/advanced-electronics-solutions/rt-duroid-laminates/rt-duroid-5880-laminates>. Accessed on September 12th, 2024.

- 85 DURRANI, S.; BIALKOWSKI, M. Effect of mutual coupling on the interference rejection capabilities of linear and circular arrays in CDMA systems. *IEEE Transactions on Antennas and Propagation*, v. 52, n. 4, p. 1130–1134, 2004.
- 86 KLINGELFUS, V. T.; APOLINÁRIO JR., J. A.; SAUNDERS FILHO, C. A. B.; RAMOS, A. L. L. A mutual coupling resistant approach for uncalibrated narrowband beamformers. *Submitted to The IEEE Transactions on Vehicular Technology*, 2025.
- 87 ZOUBIR, A.; THEODORIDIS, S.; CHELLAPPA, R. *Array and Statistical Signal Processing*. [S.l.]: Academic Press, 2013. (Academic Press Library in Signal Processing: Array and Statistical Signal Processing). ISBN 9780124115972.
- 88 RUAN, H.; DE LAMARE, R. C. Robust adaptive beamforming using a low-complexity shrinkage-based mismatch estimation algorithm. *IEEE Signal Processing Letters*, v. 21, n. 1, p. 60–64, 2014.
- 89 LI, J.; STOICA, P. *Robust Adaptive Beamforming*. [S.l.]: Wiley, 2005. (Wiley Series in Telecommunications and Signal Processing). ISBN 9780471733461.
- 90 HASSANIEN, A.; VOROBYOV, S. A.; WONG, K. M. Robust adaptive beamforming using sequential quadratic programming. In: *IEEE International Conference on Acoustics, Speech, and Signal Processing (ICASSP)*. [S.l.: s.n.], 2008. p. 2345–2348.
- 91 KHABBAZIBASMENJ, A.; VOROBYOV, S. A.; HASSANIEN, A. Robust adaptive beamforming based on steering vector estimation with as little as possible prior information. *IEEE Transactions on Signal Processing*, v. 60, n. 6, p. 2974–2987, 2012.
- 92 GU, Y.; LESHEM, A. Robust adaptive beamforming based on jointly estimating covariance matrix and steering vector. In: *IEEE International Conference on Acoustics, Speech and Signal Processing (ICASSP)*. [S.l.: s.n.], 2011. p. 2640–2643.
- 93 LIN, G.; LI, Y.; JIN, B. Research on the algorithms of robust adaptive beamforming. In: *2010 IEEE International Conference on Mechatronics and Automation*. [S.l.: s.n.], 2010. p. 751–755.